Coupling phenomena and scalability of CoFeB/Ru/CoFeB sandwiches

Dissertation zur Erlangung des Grades
eines Doktors in Naturwissenschaften
der Fakultät für Physik der
Universität Bielefeld

vorgelgt von
Nils Wiese
aus Steinhagen

Februar 2006

Erklärung:

Hiermit versichere ich an Eides statt, dass ich die vorliegende Arbeit selbständig verfasst und keine anderen als die angegebenen Hilfsmittel verwendet habe.

Glasgow, 27. Februar 2006

(Nils Wiese)

Gutachter:
Prof. Dr. Günter Reiss
Prof. Dr. Markus Sauer
Datum des Einreichens der Arbeit: 27. Februar 2006

Contents

Publications

- <u>N. Wiese</u>, T. Dimopoulos, M. Rührig, J. Wecker, H. Brückl, and G. Reiss, *Antiferromagnetically coupled CoFeB/Ru/CoFeB trilayers*, Appl. Phys. Lett. 85, 2020 (2004)

- T. Dimopoulos, G. Gieres, J. Wecker, <u>N. Wiese</u>, and M.D. Sacher, *Thermal annealing of junctions with amorphous and polycrystalline ferromagnetic electrodes*, J. Appl. Phys. 96, 6382 (2004)

- <u>N. Wiese</u>, T. Dimopoulos, M. Rührig, J. Wecker, H. Brückl, and G. Reiss, *Antiferromagnetically coupled CoFeB/Ru/CoFeB trilayers*, J. Magn. Magn. Mater. 290-291, 1427 (2005)

- <u>N. Wiese</u>, *Untersuchung von sub-μm Strukturen mit dem NanoMOKE2^{TM} - ein Anwenderbericht*, LOT-Spectrum 99, p. 7, (2005)

- T. Dimopoulos, G. Gieres, <u>N. Wiese</u>, J. Wecker, Y. Luo, and K. Samwer, *Large tunnel magnetoresistance with plasma oxidized MgO barriers*, J. Appl. Phys. 98, 073705 (2005)

- <u>N. Wiese</u>, T. Dimopoulos, M. Rührig, J. Wecker, and G. Reiss, *Switching behavior of sub-μm sized, antiferromagnetically coupled CoFeB/Ru/CoFeB trilayers*, J. Appl. Phys. 98, 103904 (2005)

- T. Uhrmann, L. Bär, T. Dimopoulos, <u>N. Wiese</u>, M. Rührig, and A. Lechner, *Magnetostrictive GMR sensor on flexible polyimide substrates*, submitted for publication in J. Magn. Magn. Mater.

- <u>N. Wiese</u>, T. Dimopoulos, M. Rührig, J. Wecker, G. Reiss, J. Nogues, and J. Sort, *Strong temperature dependence of antiferromagnetic coupling in CoFeB/Ru/CoFeB*, in preparation.

- <u>N. Wiese</u>, M. Rührig, J. Wecker, A. Drechsler, G. Tarrach, and H.J. Hug, *MFM imaging of uncompensated spins in sub-micrometer sized IrMn/CoFeB samples*, in preparation.

Conferences

- <u>N. Wiese</u>, T. Dimopoulos, G. Gieres, M.D. Sacher, and J. Wecker, *Comparative study of magnetic tunnel junctions with CoFe and CoFeB ferromagnetic electrodes*, DPG Frühjahrstagung 2004, Regensburg, Germany

- <u>N. Wiese</u>, T. Dimopoulos, M. Rührig, J. Wecker, H. Brückl, and G. Reiss, *Untersuchung der antiferromagnetischen Kopplung in CoFeB-Systemen*, DPG Frühjahrstagung 2004, Regensburg, Germany

- <u>N. Wiese</u>, T. Dimopoulos, M. Rührig, J. Wecker, H. Brückl, and G. Reiss, *Magnetic properties of antiferromagnetically coupled CoFeB/Ru/CoFeB*, Joint European Magnetic Symposia (JEMS), 2004, Dresden, Germany

- <u>N. Wiese</u>, T. Dimopoulos, M. Rührig, J. Wecker, and G. Reiss, *Schaltverhalten amorpher, nanostrukturierter CoFeB Elemente*, DPG Frühjahrstagung 2005, Berlin, Germany

- <u>N. Wiese</u>, T. Dimopoulos, M. Rührig, J. Wecker, and G. Reiss, *Switching of sub-micrometer CoFeB/Ru/CoFeB artificial ferrimagnets*, Euromat Congress 2005, Prague, Czech Republic

- <u>N. Wiese</u>, T. Dimopoulos, M. Rührig, and G. Reiss, *Strong temperature dependence of antiferromagnetic coupling in CoFeB/Ru/CoFeB*, submitted contribution for the DPG Frühjahrstagung 2006, Dresden, Germany

Introduction

In the past decades, the increasing demands of information and communication technology have been the driving force for the rapid improvements of semiconductor devices. The future demands for all fields of semiconductor production are regularly predefined by the *International Technology Roadmap for Semiconductors (ITRS)* that identifies the technological challenges and needs over the next 15 years [1]. It requires high efforts to continue with this fast progress, making smaller and faster devices that consume less power and operate with higher reliability.

Furthermore, additional functionalities like non-volatility or fast reconfigurable logic devices are desirable. By using not only the charge of an electron, but also the spin degree of freedom, the so-called magnetoelectronic (or spinelectronic) devices promise to fulfill these requirements.

Using thin magnetic multilayer systems, a variety of magnetoelectronic devices and potential applications have been developed, e.g., sensor elements in read heads of hard disks [1], angle [2] or strain sensors [3], magnetic random access memories (MRAM) [4], or even magnetic logic devices (M-Logic) [5, 6].

Although, possible applications are one of the challenging aspects for studies of spinelectronics, they just have been enabled by a variety of fundamental scientific results, that have been published in this field within the past decades. Milestones in science related to spin-dependent devices have been, e.g., the discovery of spin-dependent tunneling phenomena by JULLIERE in 1975, the giant magnetoresistive (GMR) effect by GRÜNBERG ET AL. in 1986, the effect of oscillating coupling in thin multilayer systems of two ferromagnets separated by a thin non-magnetic spacer layer by PARKIN ET AL. in 1990, the studies of exchange bias effects between thin layers of antiferromagnetic and ferromagnetic layers by MEIKLEJOHN and BEAN in 1956, the spin-injection experiments by JOHNSON and SILSBEE in 1985 [7], the proposed spin-transistor by DATTA and DAS in 1990 [8], and the spin-transfer switching predicted by SLONCZEWSKI and BERGER in 1996 [9, 10]. Reviews about the emerging field of spinelectronic for both fundamental research and industrial applications are given, e.g., in Refs. [11, 12, 13, 14, 15].

The work of this thesis has to be seen in the context of magnetoresistive phenomena and their applications. It was the aim of this thesis, to implement a new material system, an amorphous CoFeB alloy, and to study its properties in magnetic tunnel junctions (MTJ). Main focus was the investigation of the coupling phenomena in these materials and the effect for their technical application. The work is relevant for application in magnetoresistive devices and partly has been carried out within the project "Magnetoresistive logic devices". The financial support of the German Ministry for Education and Research is gratefully acknowledged (grant no.13N8208).

In order to compete with the rapid downscaling in feature size of silicon semiconductors, the spin-dependent devices will also have to be scaled down to the sub-micrometer range. In the second part of this thesis, therefore, the aforementioned concepts have been transferred to elements of sub-micrometer size. In order to get access to this small scale at experiments, patterning has been performed by electron-beam lithography, leading to sizes comparable to

---

[1]the latest version and additional information about the ITRS can be found at http://public.itrs.net/

recent MRAM devices. In order to characterize the resulting patterns, a magneto-optical Kerr effect setup has been purchased, installed, and modified. A systematic study of the switching behavior as well as the related coupling phenomena at sub-micrometer size is presented. Emphasis is given at the interlayer exchange coupling and the exchange bias effect.

Most of the phenomena for spin-dependent devices listed above are relevant for the discussion of the measurements presented in this thesis. Therefore, the first chapter covers a short introduction to most of them. The second chapter highlights the measurement methods used within this thesis. In the third chapter, the experimental results are presented and discussed. This chapter is separated into three main sections, covering the experiments at unpatterned magnetic multilayers, at patterned samples, and the studies of exchange bias effect. In the last chapter, the thesis is summarized and an outlook for further interesting investigations is given. In the appendix, the software and hardware modifications done at the magneto-optical Kerr effect setup are presented.

Comment on the units in magnetism

In the field of magnetism, the cgs system is still often used for magnetic properties. Wherever possible and useful, the SI system is used in this thesis. Nevertheless, since all micromagnetic simulation software use cgs units, the cgs system is sometimes used in the discussion of simulation results. The cgs system is also used in some of the figures which have been reproduced from other publications.

An overview of the most important magnetic quantities and their cgs and SI units is given in table 0.1, along with conversion factors.

Parameter		cgs unit	conv. factor	SI unit
Magnetic flux density	B	gauss (G)	10^{-4}	tesla (T), Wb/m^2
Magnetic flux	Φ	maxwell (Mx), G·cm^2	10^{-8}	weber (Wb), Vs
Magnetic field strength	H	oersted (Oe)	$10^3/4\pi$	A/m
(Volume) magnetization	M	emu/cm^3	10^3	A/m
(Volume) magnetization	$4\pi M$	gauss (G)	$10^3/4\pi$	A/m
Magnetic moment	m	emu, erg/G	10^{-3}	A·m^2, J/T
Permeability	μ	dimensionless	$4\pi \times 10^{-7}$	H/m, Wb/(A·m)
Demagnetization factor	N	dimensionless	$1/4\pi$	dimensionless
Anisotropy constant	K_u	erg/cm^3	10^{-1}	J/m^3
Interlayer coupling	J	erg/cm^2	1	mJ/m^2

Tab. 0.1: *Magnetic quantities and their units in the cgs and SI systems, respectively. In order to convert from cgs units into SI units, one has to multiply the cgs units with the given conversion factor.*

1 Theory

The main motivation for investigating coupling phenomena in CoFeB based thin film systems is their use in magnetoresistive devices. In this chapter, the basics needed for understanding the discussed phenomena are introduced.

Therefore, the first section will include a short overview of tunneling phenomena in thin film systems, with a special emphasis on the spin-dependent tunneling effect used in magnetoresistive devices. In the second section, there is a treatment of the coupling phenomena in magnetic multilayer systems, that are important for the samples under investigation. In the third section the switching properties of sub-micrometer magnetic elements by means of the Stoner-Wohlfarth model are discussed. This model is then applied in the following section to sub-micrometer scaled artificial ferrimagnets.

1.1 Tunneling Magnetoresistance (TMR)

1.1.1 Tunneling phenomena in thin film systems

From the classical point of view, a particle can overcome an energy barrier only if its energy is higher than the barrier height. If tunneling processes are taken into account, they have to be described using the quantum mechanical framework. Here the tunneling process is described as a transmission probability of particles (e.g. electrons passing from one to the other electrode) through a potential barrier (e.g. a thin film of insulating material like AlO_x or MgO).

In figure 1.1, the tunneling in a metal-insulator-metal (M/I/M) system is visualized. Considering an incident electron wave $\Psi(0)$ crossing a potential barrier, a part of it will be reflected, and the other part will enter the barrier. Its intensity decays exponentially across the barrier thickness. If the barrier is thin enough (of the order of one nm), the wave function Ψ_T at the right side of the barrier differs from zero. Therefore, the electron will not have a vanishing probability of passing the barrier, given by $T(E) = \frac{|\Psi_T|^2}{|\Psi(0)|^2}$.

In a tunneling system with an applied bias voltage, V, the number of electrons tunneling from the left to the right electrode is given by the product of the density of states at a given energy in the left electrode, $D_1(E)$, and the density of states at the other electrode, $D_2(E)$, multiplied by the square of the matrix element $|M|^2$, describing the probability of tunneling. Furthermore, one has to take into account the probability that the states at the left electrode are occupied, described by the Fermi-Dirac function $f(E)$, and the probability that the states at the right are empty, $[1 - f(E + eV)]$. This results in a tunneling current, given by [17]

$$I_{1,2}(V) = \int_{-\infty}^{\infty} D_1(E) \cdot D_2(E + eV)|M|^2 f(E) \left[1 - f(E + eV)\right] dE \qquad (1.1)$$

A similar equation can be given for the electrons traversing from the right to the left, and the total tunnel current is given by $I_{1,2} - I_{2,1}$. If no bias voltage is applied across the barrier (i.e. $eV = 0$), the quantity of electrons traversing from left to right and from right to left will
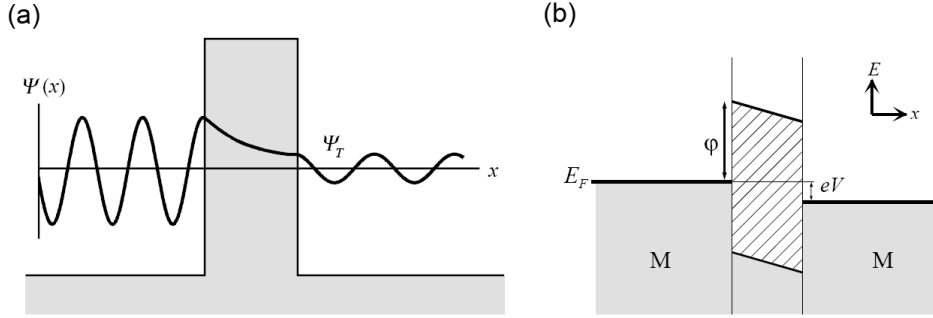
(a)

(b)

Fig. 1.1: *Tunneling in metal-insulator-metal structures. (a) Electron wave function decays exponentially in the barrier region, and for thin barriers, some intensity remains in the right side. (b) Potential diagram of a M/I/M structure with applied bias eV [16].*

balance each other. The system will stay in equilibrium, with the Fermi levels at the same energies.

One simple way to solve equation 1.1 has been shown by SIMMONS [18]. As approximation of an arbitrary barrier, he assumed a rectangular energy barrier of mean height $\bar{\varphi}$. He then used a step-function, i.e. the Fermi-Dirac function at $T = 0$, and the WKB approximation (named after Wenzel-Kramers-Brillouin) to obtain the matrix elements of $|M|^2$. Simmons' approach only takes into account a symmetric M/I/M system with the same material and density of states on both sides. This simple model was extended by BRINKMAN ET AL. describing an asymmetric M/I/M junction by using an additional asymmetry parameter $\Delta\varphi$ [19].

Neither of the models considers the dependence of the transport characteristics on the electronic density of states (DOS) in the electrodes. However, the simplified models of Simmons and Brinkman can qualitatively describe the experimentally observed $I - V$ characteristics in spin-dependent tunneling elements at least for small bias voltage.

1.1.2 Spin-dependent tunneling phenomena

Spin-dependent tunneling was discovered by TEDROW and MESERVEY in the early 1970s. They measured the conduction electron spin polarization (P) of electrons tunneling from a ferromagnet into a superconducting Al film [20, 21]. Their experiments showed that the conduction electrons in ferromagnetic materials are spin polarized and that the spin is conserved during the tunneling process [12].

The first evidence of spin-dependent tunneling was demonstrated by JULLIERE in Co/Ge/Fe junctions in 1975 [22]. He observed, at low temperatures ($T = 4.2\text{K}$), a change in resistance depending on the relative orientation of the magnetizations of the electrodes. He described the tunneling magnetoresistance (TMR) depending on the spin polarization, $P_{1,2}$, of the two ferromagnetic electrodes as

$$TMR = \frac{\Delta R}{R} = \frac{R_{AP} - R_P}{R_P} = \frac{2P_1 P_2}{1 - P_1 P_2} \tag{1.2}$$

where $R_{\mathbf{P}}$ and $R_{\mathbf{AP}}$ are the resistances in the parallel and antiparallel orientation of the ferromagnetic electrodes, respectively.

Finally, in 1995, two groups (Miyazaki et al. and Moodera et al.) independently reported room temperature measurements of the TMR effect in FM/I/FM systems [23, 24]. These results led to intensive experimental efforts, since the room temperature TMR effect is the basis for various magnetoelectronic applications, as pointed out in the introduction. A detailed overview on spin-dependent tunneling can be found, e.g., in Ref. [12].

Influence of barrier material on TMR

After the demonstration of the TMR effect at room temperature, AlO_x has become by far the most commonly studied tunnel barrier. Combined with polycrystalline CoFe or/and NiFe (permalloy) electrodes, TMR values as high as 50% at room temperature have been obtained. Recently, amorphous FM electrodes have been employed [25] and, in particular the use of CoFeB, has further increased the effect to nearly 70% [26].

Due to the technological requirements, a further decrease in the resistance area product (RA) of the barrier has to be achieved, especially for sensor elements in hard disk drives and for MRAM applications. This constraint requires a further shrinking of the barrier thickness, with proven detrimental effects for the TMR (e.g. pinholes) [27]. An alternative to reducing the barrier thickness, is the use of different barrier materials in order to lower the RA value, e.g. TaO, ZnS, AlN, and YO_x [28, 29, 30, 31]. Unfortunately, to date, almost all alternative barriers have also led to a smaller TMR.

Experimental efforts have particularly concentrated the last few years on MgO barrier. The motivation arose from the theoretical predictions that a huge TMR effect of several hundred percent is to be expected in perfectly ordered (001) Fe/MgO/Fe [32, 33] and CoFe/MgO/CoFe [34] junctions. The first successful experimental reports were for epitaxial Fe/MgO/Fe junctions grown by molecular beam epitaxy (MBE), where a TMR effect of 80% was obtained at room temperature [35]. Recently, for MBE-grown Fe/MgO/Fe MTJs, a room temperature TMR of 230% has been reported, with a dependence on the barrier thickness in accordance with the theoretical predictions [36]. Most interestingly, similar results have been simultaneously reported for sputtered multilayers [37]. There, the MgO barrier has been deposited reactively in an Ar/O_2 mixture. To our knowledge, in the only work concerning plasma oxidized MgO barriers, a low TMR of $\approx 5\%$ has been reported [38]. The low effect has been attributed to the lack of texture in the barrier, which comprised a mixture of polycrystalline and amorphous regions. In a recent publication, we have shown that sputter deposited junctions with plasma oxidized MgO barriers can lead to high TMR values of nearly 60% and additionally offer low resistance-area product and unsurpassed thermal stability [39]. The current record for published results on TMR effect has been announced by Ikeda et al. from Hitachi with a TMR of 355% at room temperature and 578% at 5K, forming the barrier by sputtering from a MgO target [40].

1.1.3 Typical stack systems for TMR experiments

The simplest TMR multilayer system consists of two ferromagnetic electrodes separated by a thin insulating barrier as shown in figure 1.2(a). One of the ferromagnetic layers acts as a *reference* or *hard magnetic electrode (HE)*, the other one as a *sense* or *soft magnetic electrode (SE)*. The HE should keep its magnetization in the operational field window, while the orientation of the SE can be changed by an external magnetic field.

This simplest layout of a magnetic tunnel junction device has been improved by several
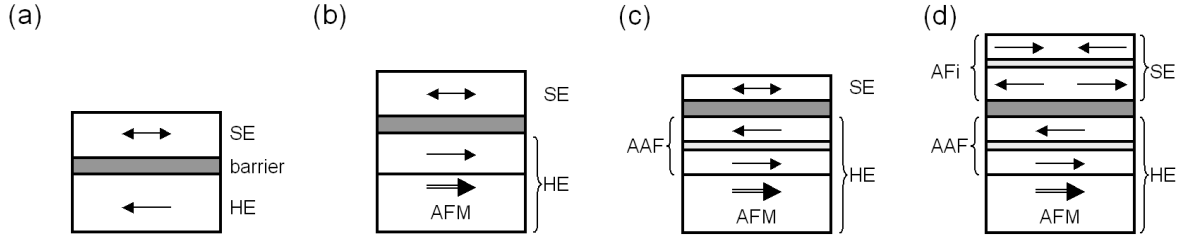
Fig. 1.2: *Schematics of the "evolution" of MTJ stacks: (a) Single ferromagnetic layer hard and soft electrode (HE and SE, respectively), (b) exchange biased hard electrode, (c) exchange biased AAF as hard electrode and (d) exchange biased AAF as hard electrode and AFi as soft electrode. The arrows indicate the direction of magnetization in the two remanent states, in case of the antiferromagnet (AFM) they indicate the exchange bias direction.*

steps of "evolution" as shown in figure 1.2. To achieve a more rigid reference electrode, the so-called *exchange bias effect*, a direct coupling between a ferromagnetic layer and a natural antiferromagnet (AFM) has been implemented to the multilayer system (see figure 1.2 (b)). To reduce the magnetic stray field from the reference layer and to further stabilize the reference electrode, the ferromagnetic layer within the hard electrode has been substituted by a system of two antiferromagnetic coupled ferromagnetic layers as shown in figure 1.2(c). These systems are called an *Artificial Antiferromagnet (AAF)* or *Artificial Ferrimagnet (AFi)*, depending on their net magnetic moment. Recently, such a coupled system was also discussed for use as a soft magnetic electrode as shown in figure 1.2(d).

The underlaying concepts of the above mentioned coupling phenomena (interlayer exchange coupling, exchange biasing, etc.) will be addressed in the following paragraphs.

1.2 Interlayer exchange coupling

In magnetic multilayers, an indirect interlayer exchange coupling between two ferromagnets (FM) separated by a non-magnetic spacer (NM) layer is often used. As we will see, these systems can exhibit a stable ground state, where the two ferromagnetic layers are oriented antiparallel to each other in zero field.

This antiferromagnetic coupling can be used to compensate the moment of an electrode in elements used for magnetoresistive devices or sensors, therefore reducing the stray field of this electrode. Furthermore, the indirect antiferromagnetic (AF) exchange coupling increases the rigidity of these systems in comparison to a single ferromagnetic layer [41, 42].

In the following, the AF coupled systems will be called *Artificial Ferrimagnets (AFi)* or *Artificial Antiferromagnets (AAF)*, depending on the net moment $m_{net} = m_1 - m_2$ of the two layers at the ground state ($m_{net}^{AFi} \neq 0$ in case of the AFi, and $m_{net}^{AAF} = 0$ in case of the AAF). In the literature, the name *Synthetic Antiferromagnet (SAF or SyAF)* is also found for these systems. Furthermore, we define such AF coupled systems as a *positive (negative) AFi* if $t_1 > t_2$ ($t_1 < t_2$).

One has to consider different coupling contributions in magnetic multilayer systems, separated by a non-magnetic spacer. The total interlayer exchange coupling can be regarded as a superposition of different mechanisms, that can be ferromagnetic (F), antiferromagnetic (AF),

or both:

- Ruderman-Kittel-Kasuya-Yosida (RKKY) like coupling (F or AF type, depending on spacer layer thickness)

- Néel coupling (F type, roughness induced magnetostatic coupling)

- stray field coupling (AF type, magnetostatic coupling, only in patterned magnetic multilayers of importance)

- direct ferromagnetic coupling by pinholes (F type)

In the following sections, we will discuss these coupling terms, as they are important for the samples investigated in this thesis.

1.2.1 Coupling through non-magnetic spacer layers

The first evidence of antiferromagnetic coupling between two ferromagnetic layers, separated by a thin non-magnetic layer, was reported by GRÜNBERG ET AL. in 1986 in a multilayer system of Fe/Cr/Fe [43].

Two years later, GRÜNBERG'S and FERT'S group discovered the *giant magnetoresistance (GMR)* effect [44, 45]. This effect refers to the dependence of a sample's resistivity on an applied external magnetic field and depends on the relative orientation of the magnetizations of the ferromagnetic layers. If the layers are antiferromagnetically coupled for zero applied field, then the magnetizations of the two layers are antiparallel in orientation. GRÜNBERG and FERT found that this antiparallel state has a significantly higher resistance than the parallel state, which can be obtained in an external magnetic field larger than the saturation field. This effect is therefore called *giant magnetoresistance.*

In 1990, PARKIN discovered oscillatory behavior of the dependence of the giant magnetoresistance on the thickness of the non-magnetic spacer layer [46]. He showed, that these oscillations were not due to variations in the transport properties but rather, variations in the coupling between the ferromagnetic layers. For some thicknesses, the coupling was ferromagnetic, favoring parallel alignment of the magnetization directions at zero field. For these thicknesses, there was no change in the relative alignment of the magnetizations when a magnetic field was applied; hence, the magnetoresistance was almost zero.[1]

To explain the physical origin of the oscillating coupling between magnetic layers mediated by a non-magnetic spacer, PARKIN also suggested the Ruderman-Kittel-Kasuya-Yosida (RKKY) coupling as one possible origin of the observed exchange coupling [46].

The RKKY coupling originally describes the coupling between two magnetic impurities in a non-magnetic host. Hybridization between the s-p conduction electrons of the host metal and the d- (or f-) electrons of the magnetic impurity produces an effective on-site exchange coupling at the impurity site. This coupling between the two impurities oscillates in sign and decreases in amplitude with the distance (see figure 1.3) [47, 48]. Several groups transferred the RKKY model to the multilayer case, assuming the interaction between two two-dimensional sheets of impurities (the ferromagnetic layers) embedded in a non-magnetic host (the non-magnetic spacer) [49, 47, 50]. These models give a coupling that oscillated as

$$\frac{sin(2k_\mathrm{F}t)}{t^2} \qquad \text{for} \qquad t \gg \lambda$$

---

[1]Only a small change in resistance exists due to the anisotropic magnetoresistance (AMR).

where t is the interlayer thickness, k_{F} the Fermi wave vector of the interlayer material, and $\lambda = \frac{\pi}{k_{\mathrm{F}}}$ the period of the oscillation. The period is the same as in the case of the coupling between two magnetic impurities in a free electron host metal, but, in the planar case, the coupling decays more slowly than in the impurity case ($1/t^2$ instead of $1/t^3$) [49, 51, 47].

While the RKKY model describes many of the observed properties in FM/NM/FM sandwiches, there are several disagreements in comparison to real multilayer systems. One of the most important is that the oscillation period, approximately 1 nm, was much longer than was expected from estimates based on the analogy with the RKKY interaction [52].

In more recent publications about interlayer exchange coupling, a *Quantum Well Model* is assumed to describe the electronic states in the non-magnetic spacer layer. In this model, a spin-dependent electron confinement is the origin of the interlayer exchange coupling.

The origin of ferromagnetism is an imbalance of the spin-up and spin-down electrons in the 3d sub-band. The density of states of the *majority band* is shifted downwards with respect to the Fermi energy, E_F, and the *minority band* is only partially occupied. Hence, there are free states in the minority band and a lack of free states in the majority band. If the electrons are traversing from one

Fig. 1.3: *Coupling as a function of the spacer layer thickness as calculated within the continuum version of the RKKY model [47]. The dashed line indicates the so-called "aliasing effect" due to the discrete thickness variation of the spacer. Therefore, the rapidly varying oscillation is sampled and appears to be a slower varying function.*

ferromagnetic electrode to the other, the probability of scattering is proportional to the density of states. For parallel alignment of the magnetizations of the electrodes, this probability is much higher for the minority electrons. The majority electrons can propagate through the stack system with a low scattering probability. The minority carriers are reflected at both interfaces and, therefore, confined in the spacer material. The reflection of minority spin electrons at both interfaces leads to an interference of electron waves and standing electron waves will occur. In the case of an antiparallel orientation of the magnetizations, both minority and majority carriers are reflected by one of the interfaces. Therefore, the condition for quantum confinement is not fulfilled [53].

In the frame of the quantum well theory, the oscillation periods are related to the oscillation of the reflection coefficients at the magnetic/non-magnetic interface. The results, however, are the same as within the RKKY theory [54].

There are several review papers on the interlayer exchange coupling and its theory, see, e.g., Ref. [55] in the book *"Ultrathin Magnetic Structures III"*.

Phenomenological description of interlayer exchange coupling

In a simple phenomenological model, such an AF coupled system can be considered as a rigid magnetic body with a reduced net moment, showing a rotation like magnetization reversal
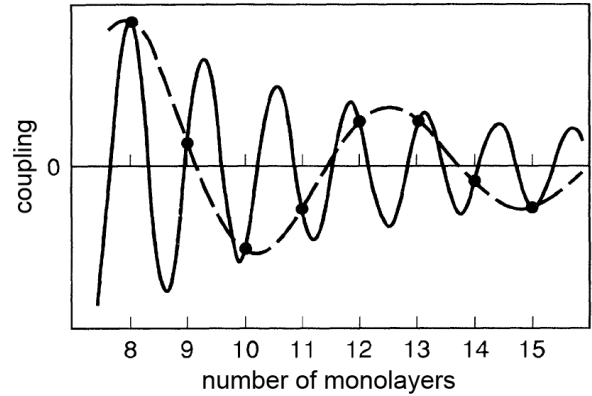
(Stoner-Wohlfarth behavior). This assumption is valid, since in strongly coupled systems it has been found that the rotational reversal process is favored in comparison to the domain nucleation processes [56].

The total energy of an uncompensated AFi system can be written as the sum of the anisotropy energy (E_A), the coupling energy (E_C) and the Zeeman energy (E_Z) [57, 58]:

$$
\begin{aligned}
E &= E_C + E_A + E_Z \\
&= -J_{\text{lin}} \cos(\varphi_1 - \varphi_2) - J_{\text{bq}} \cos^2(\varphi_1 - \varphi_2) \\
&\quad + K_1 t_1 \sin^2 \varphi_1 + K_2 t_2 \sin^2 \varphi_2 \\
&\quad - \mu_0 H (M_1 t_1 \cos \varphi_1 + M_2 t_2 \cos \varphi_2)
\end{aligned}
\tag{1.3}
$$

where $M_{1,2}$ and $t_{1,2}$ are the magnetic moments and the thicknesses of the ferromagnetic layers, $\varphi_{1,2}$ are defined as the angle between the magnetization vector of the layers with respect to the direction of the applied field H (see figure 1.4(a)).

The first two terms in 1.3 describe the interlayer exchange coupling energy, where J_{lin} is the linear and J_{bq} the second order (biquadratic) contribution. The following terms describe the anisotropy contributions of the two individual layers. Only uniaxial anisotropies are taken into account, and K_1 and K_2 are the anisotropy constants per unit volume for the two layers. Finally, the fifth term is the Zeeman energy of the two ferromagnetic layers with respect to the applied field H.

In figure 1.4, the result of the energy minimization problem for a simulation of the $M(H)$ dependence of a typical AF coupled system is given. Within the calculation, the parameters for a CoFeB-AFi are assumed: $M_1 = M_2 = M_{\text{s}} = 860 \frac{\text{emu}}{\text{cm}^3}$, $J_{\text{lin}} = -0.1 \frac{\text{erg}}{\text{cm}^2}$, $J_{\text{bq}} = 0$ and $K_1 = K_2 = K = 5 \times 10^3 \frac{\text{erg}}{\text{cm}^3}$. The thicknesses of the FM layers have been chosen so that $t_1 = 4$nm and $t_2 = 3$nm. The basic characteristics of the simulation result will now be discussed step-by-step:

- $H \geq H_{\text{sat}}$
  For large applied magnetic fields the Zeeman contribution is dominating and therefore the magnetic moments of the AFi are aligned in parallel.

- $H_{\text{p}} \leq H \leq H_{\text{sat}}$
  At this field region, the magnetic moment of the thinner layer of the AFi begins to rotate in order to be aligned antiparallel to the magnetic moment of the thicker AFi layer (see figure 1.4(b)). While φ_2 opens up from 0 to 180° in the flank region, the magnetic moment of the thicker AFi experiences angle rotation to the opposite direction and flips back to its initial position parallel to the field direction. Finally, the antiferromagnetic alignment is established at the plateau field, H_{p}.

- $-H_{\text{p}} \leq H \leq H_{\text{p}}$
  Due to the dominating AF coupling term, the AFi is in its antiparallel ground state at this field region. At the coercivity of the AFi, $H_{\text{c}}^{\text{AFi}}$, the reversal of the two layers takes place. Due to the strong AF coupling, the AFi could be considered as a rigid body with a reduced net moment of $m_{\text{net}} = m_1 - m_2$, and the switching can be considered as a coherent rotation of both layers. Here, the magnetization of the thicker layer tries to turn parallel to the applied external field.

- $-H_{\text{sat}} \leq H \leq -H_{\text{p}}$
  For increasing opposite fields, the Zeeman energy increases and gradually dominates over
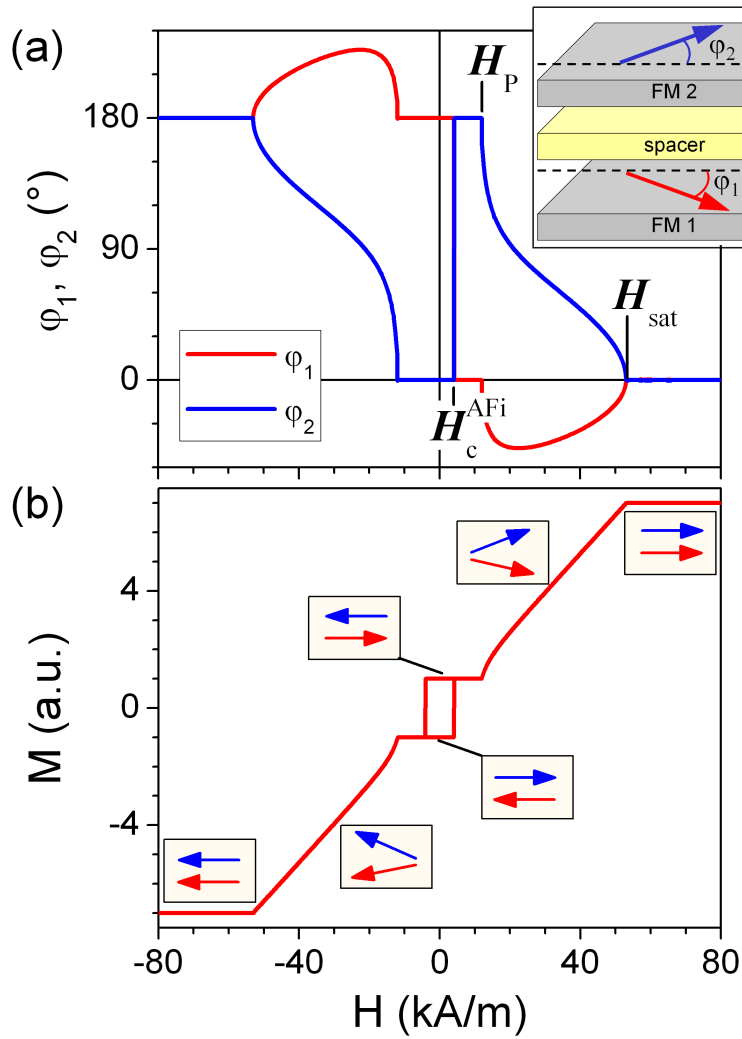
Fig. 1.4: *Numerical calculation of (a) the variation of the angles φ_1 and φ_2 between the two layers within the AFi and (b) the hysteresis curve of the AFi. Parameters of CoFeB-AFi have been assumed for the calculation.*

the AF coupling energy. Again, the thinner layer has to rotate by 180°. The thicker layer just exhibits small angle variations and flips back to the direction parallel to the field at the saturation field.

- $H \leq -H_{\text{sat}}$
  In this field region, the Zeeman energy is the dominating factor again, and the two ferromagnetic layers are oriented parallel to the applied field.

The interlayer coupling strength, J_{lin}, can be expressed in terms of the saturation field, H_{sat}, by the relationship [41]

$$J_{\text{lin}} = -\mu_0 H_{\text{sat}} \frac{M_1 t_1 M_2 t_2}{M_1 t_1 + M_2 t_2} \tag{1.4}$$

Rigidity enhancements due to AF coupling

VAN DEN BERG ET AL. has shown in Refs. [41, 42], that indirect antiferromagnetic exchange coupling increases the rigidity of AFi systems in comparison to a single ferromagnetic layer. The AFi can be regarded as a rigid magnetic body with a reduced magnetic moment but with full presence of the intrinsic switching friction of both layers:

$$H_{\text{c}}^{\text{AFi}} = \frac{t_1 \tau_1 + t_2 \tau_2}{t_1 M_1 - t_2 M_2} = \frac{m_1 + m_2}{m_1 - m_2} \cdot \frac{t_1 \tau_1 + t_2 \tau_2}{t_1 M_1 + t_2 M_2} \tag{1.5}$$

where M_1, M_2, t_1, t_2 and τ_1, τ_2 are the saturation magnetization, the thickness and the volume density of the frictional torque of the two composite ferromagnetic layers. $H_{\text{c}}^{\text{AFi}}$ is the resulting coercivity of the AF coupled system. With $Q = \frac{m_1 + m_2}{m_1 - m_2}$ quantifying the gain in coercivity with respect to a single layer, one achieves

$$H_{\text{c}}^{\text{AFi}} = Q \cdot H_{\text{c}}^{\text{SL}} \tag{1.6}$$

Therefore, the Q value and the coercivity $H_{\text{c}}^{\text{AFi}}$ can be tailored easily by modifying the thickness of the ferromagnetic layers. One should, however, note that equation 1.5 is valid only as long H_{sat} given by the coupling strength in equation 1.4 is larger than H_{c}.

Such AFi systems have been first integrated into magnetoresistive devices, due to their increase in rigidity, as a hard magnetic (or reference) layer. The stability of these systems can be increased further by combining them with an exchange biasing to a natural antiferromagnet (see section 1.2.2), and they are widely used in today's magnetoresistive devices [59, 60].

Also, in recent years, several groups investigated the properties of these systems for use as a soft magnetic (or sensing) layer. By the compensation of the two ferromagnetic layers in the soft magnetic layer, the stray field can be decreased additionally. This enables one to further increase the integration of magnetoresistive devices in applications like MRAM or M-Logic. Furthermore, it has been shown that such AFi free layers show a smaller switching field distribution [61], and patterned elements with a small aspect ratio more easily retain a single domain structure [62]. Both is originated by the increased effective anisotropy and the reduced demagnetizing fields at the edges of sub-micrometer size AFi elements.

While, so far, only AFi systems with polycrystalline materials have been treated in the literature, it was the purpose of this thesis to extend the knowledge about AFi soft electrodes towards amorphous alloys. We have used an amorphous alloy of the composition $Co_{60}Fe_{20}B_{20}$, separated by a thin Ru spacer layer. The results are presented in section 3.1 and have been recently published in Refs. [63, 64].

Temperature dependence

Shortly after the first experiments of oscillating coupling phenomena in FM/NM/FM systems, a strong temperature dependence of the coupling strength was observed [65]. Several theoretical studies have focused on the temperature dependence of interlayer exchange coupling [50, 66, 67], concluding that the velocity of electrons at the extremal points of the Fermi surface, v_{F}, governs the temperature dependence:

$$J(T) = J_0 \frac{T/T_0}{\sinh(T(T_0))} \tag{1.7}$$

The characteristic temperature, T_0 is given by

$$T_0 = \frac{\hbar v_{\mathrm{F}}}{2\pi k_B t_{\mathrm{NM}}} \tag{1.8}$$

This relationship first was experimentally confirmed by ZHANG ET AL. in Co/Ru/Co trilayer films using ferromagnetic resonance [68]. In these studies the characteristic temperature for Ru is of the order of 100K, resulting in a Fermi velocity of $v_{\mathrm{F}} \approx 10^7 \mathrm{cm/s}$. The Fermi velocity in Ru is, therefore, about one order of magnitude smaller than for a typical free electron gas in most non-magnetic metals, where $v_{\mathrm{F}} \approx 10^8$ [54, 69]. In these materials, the characteristic temperature is of the order of $T_0 \approx 1800K$ and $J(300K) \approx 0.99 J(0)$ and frequently can be ignored. The low characteristic temperature of $T_0 \approx 100K$ in the case of Ru leads to $\frac{J(\mathrm{RT})}{J_0} < 0.3$. Therefore, this property can be considered as the origin for a strong temperature dependence in AFis with Ru as a non-magnetic spacer.

It is worth mentioning that this theory just takes into account the bilinear coupling. Therefore, a temperature dependence as described by equation 1.7 is a good verification of dominating bilinear coupling.

1.2.2 Exchange Bias

In 1956, MEIKLEJOHN and BEAN reported *"a new type of magnetic anisotropy, which is best described as an exchange anisotropy. This anisotropy is the result of an interaction between antiferromagnetic material and a ferromagnetic material"* [70, 71]. Of particular technological interest is the *exchange bias effect* produced in ferromagnetic films that are coupled to an appropriate antiferromagnetic film, e.g., IrMn or PtMn.

Cooling a FM/AFM thin film bilayer from $T > T_{\mathrm{N}}(\mathrm{AFM})$ (but keeping $T < T_{\mathrm{c}}(\mathrm{FM})$) in a saturating magnetic field produces an unidirectional anisotropy that shifts the magnetization loop of the pinned FM layer along the field axis. Until now, no basic, generally applicable model to describe the exchange bias effects has existed. The reason is that the essential behavior depends critically on the atomic-level chemical and spin structure at a buried interface [72]. The most important models for exchange bias are:

- phenomenological model with ideal interfaces

- interfacial AFM domain wall model (MAURI et al., Ref. [73])

- random field model (MALOZEMOFF, Ref. [74, 75])

- spin-flop perpendicular interfacial coupling (KOON, Ref. [76])

- uncompensated interfacial AFM spins (MEIKLEJOHN and BEANS, experimentally verified by TAKANO et al., Ref. [77])

A complete review of experimental results and theoretical models can be found, e.g., in references [72, 78, 79]. In this thesis, the focus will be on the phenomenological model and the model of uncompensated spins.

The first model of exchange bias assumes an ideal interface between the ferromagnetic and antiferromagnetic layers, i.e. atomically smooth and single crystalline. The AFM is composed of ferromagnetically oriented spins with anti-parallel alignment between adjacent planes (see figure 1.5(a)), resulting in a plane of fully uncompensated spins at the FM/AFM interface. During the reversal of the FM magnetization in this ideal model, the spins of the FM layer rotate coherently, while the spins of the AFM layer remain fixed. The energy cost is equal to the interfacial exchange energy and the resulting exchange bias field is given by

$$H_{\mathrm{EB}} = \frac{\Delta\sigma}{M_{\mathrm{FM}}t_{\mathrm{FM}}} = \frac{2J_{\mathrm{ex}}\mathbf{S}_{\mathrm{FM}} \cdot \mathbf{S}_{\mathrm{AFM}}}{a^2 M_{\mathrm{FM}}t_{\mathrm{FM}}} \tag{1.9}$$

where $\Delta\sigma$ is the interfacial exchange energy density, J_{ex} is the exchange parameter, $\mathbf{S}_{\mathrm{FM}}$ and $\mathbf{S}_{\mathrm{AFM}}$ are the spins of the interfacial atoms, and a is the cubic lattice parameter [72].
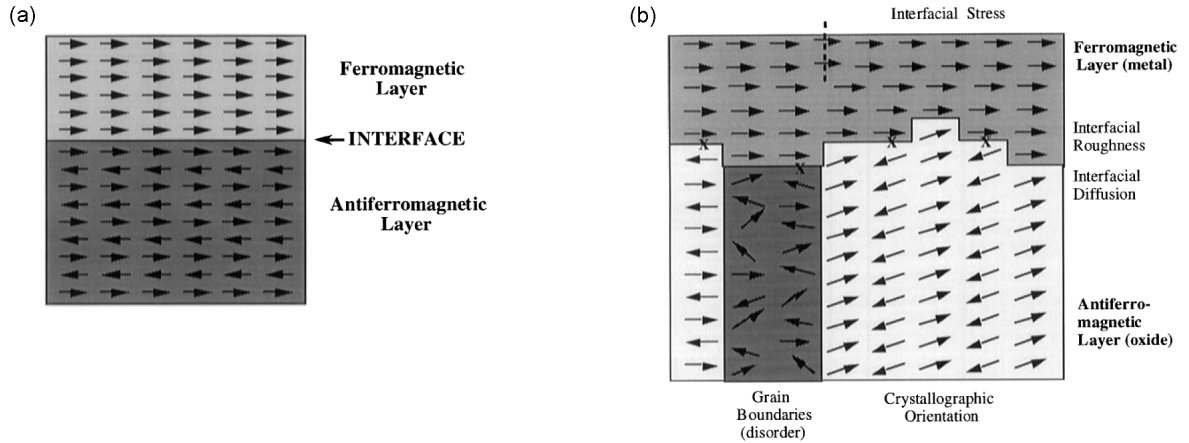

Fig. 1.5: *(a) Schematics of an ideal FM/AFM interface. The AFM interfacial plane consists of a plane of fully uncompensated spins. (b) Schematics of the interfacial complexity of a polycrystalline FM/AFM interface. The X marks identify the frustrated exchange bonds, i.e. the interfacial spins that are coupled antiferromagnetically. Figures taken from Ref. [72].*

The experimentally observed exchange fields are typically less than a few percent of the values predicted by this idealized model [77]. This is attributed to the fact that this simple model does not represent realistically the FM/AFM interfacial environment. Phenomena such as diffusion at the interface or roughness have to be taken into consideration for the reduction of the exchange biasing. Figure 1.5(b) schematically shows the interfacial complexity of a polycrystalline FM/AFM interface. Roughness, in the form of interfacial atomic steps, could produce neighboring antiparallel spins, thereby reduce the number of interfacial uncompensated spins (see figure 1.5(b)).

The first experimental proof of uncompensated spins as the origin for exchange bias has been presented by TAKANO et al. for polycrystalline CoO/NiFe bilayers. They determined the magnetic moments of the uncompensated spins by measuring thermoremanent moments (TRM) in CoO/MgO multilayers. This moment is interfacial and is $\sim 1\%$ of the spins in a monolayer of CoO. Furthermore, the TRM exhibited the same temperature dependence as the exchange bias field of NiFe/CoO bilayers. Since the TRM originates from the uncompensated interfacial AFM spins, they appear to be the spins responsible for the unidirectional anisotropy [77].

From a technological view, it is interesting to investigate the exchange bias phenomena in sub-micrometer scale magnetic elements. This is discussed in section 3.5 of this thesis, for material systems and lateral sizes that are comparable to MRAM demands.

1.2.3 Néel coupling

In 1962, Néel introduced a theory to describe the magnetostatic coupling between two ferromagnetic layers separated by a non-magnetic spacer, which is due to the topographic irregularities of the two interfaces involved [80]. This phenomenon, therefore, is called *Néel coupling*. Sometimes the terminology *orange peel coupling* is used instead.

In magnetostatics, discontinuities in the magnetization at the boundaries of the magnetic material act as *magnetic poles* $(-div\vec{M} = \mu_0\vec{H})$. With the correlated roughness of the magnetic layers as shown in figure 1.6, the "mountains" and "valleys" produce small magnetic dipoles. The most stable orientation is the one where the magnetizations of the two ferromagnetic layers are parallel, because only then the charges on both sides of the spacer cancel out each other. Therefore, the contribution of the Néel coupling is of the ferromagnetic type.
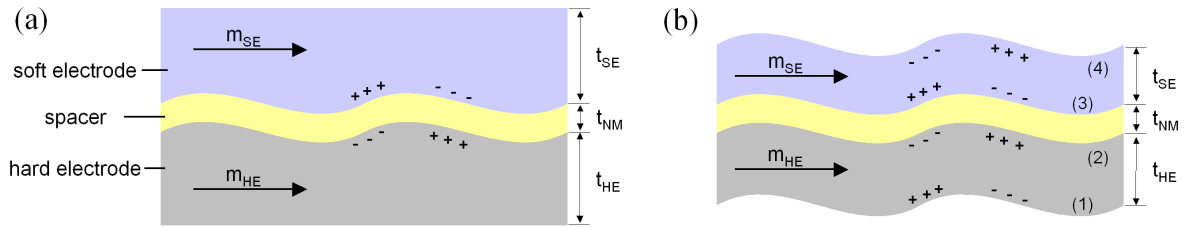
Fig. 1.6: *(a) Schematic of the original Néel model with magnetic films of infinite thickness and correlated interface roughness, and (b) structure with conformal waviness and finite thicknesses of the magnetic layers used by the model of Kool's*

The original Néel model assumes a correlated waviness with amplitude h and wavelength λ between the two ferromagnetic layers of infinite thickness and saturation moments $M_{1,2}$, separated by a non-magnetic spacer with thickness t_{NM} (see figure 1.6 (a)).

The interlayer coupling energy, J_N, due to the Neel coupling is given by [80]

$$J_N = \mu_0 \frac{\pi^2 h^2}{\sqrt{2}\lambda} M_1 M_2 \cdot \exp\left(-\frac{2\pi\sqrt{2}t_{NM}}{\lambda}\right) \qquad (1.10)$$

In magnetoresistive devices, where one magnetic layer remains fixed (hard electrode, HE), and the soft magnetic layer (soft electrode, SE) is switched under application of an external

magnetic field, the shift is determined by the magnetostatic Néel coupling [80]

$$H_N = \frac{J}{\mu_0 M_{SE} t_{SE}} = \frac{\pi^2 h^2}{\sqrt{2}\lambda t_{SE}} M_{HE} \cdot \exp\left(-\frac{2\pi\sqrt{2}t_{NM}}{\lambda}\right) \tag{1.11}$$

Néel coupling for finite electrode thicknesses

This simple model can be expanded by taking into account statistical roughness of the interface [81] and by regarding the finite thickness of the ferromagnetic layers [82, 83]. KOOLS ET AL. extended the Néel model for spin valves with finite magnetic film thicknesses and conformal waviness (see figure 1.6(b)) [82, 84]. In this case, the offset field of the Néel coupling is given by

$$\begin{aligned} H_N &= \frac{\pi^2 h^2 M_{HE}}{\sqrt{2}\lambda t_{SE}} \cdot \exp\left(-\frac{2\pi\sqrt{2}t_{NM}}{\lambda}\right) \\ &\times \left[1 - \exp\left(-\frac{2\pi\sqrt{2}t_{SE}}{\lambda}\right)\right]\left[1 - \exp\left(-\frac{2\pi\sqrt{2}t_{HE}}{\lambda}\right)\right] \end{aligned} \tag{1.12}$$

In equation 1.12, the original Néel equation is corrected by the magnetostatic contributions of the upper interface of the soft electrode and the lower interface of the hard electrode. It has been found that the coupling field increases slightly with the pinned layer thickness and decreases with the free layer thickness [84].

From both models, one can extract the basic features of the roughness induced coupling effects that have been experimentally found for magnetic multilayer devices by various groups [81, 85]. In figure 1.7, the dependencies have been calculated using Néel's and Kool's equations for reasonable interface parameters (given inside the figure).

- *dependence on roughness parameters (wavelength λ and amplitude h):*
  For small wavelengths, the interfacial roughness is dominated by the exponential function in equations 1.10 and 1.12. Therefore, a strong increase of the coupling field, H_N, with the wavelength is found. For large wavelengths, the $1/\lambda$ term is dominating and H_N decreases. Kool's correction for finite thicknesses of the magnetic layers causes a stronger decrease of H_N for large wavelength.
  An increasing amplitude, h, of the roughness causes a strong increase in H_N with a h^2 behavior.

- *dependence on soft electrode thickness t_{SE}:*
  The Néel coupling field, H_N. increases for decreasing soft layer thickness, t_{SE}, as the surface contribution of the ferromagnetic Néel coupling becomes more dominant.

- *dependence on hard electrode thickness t_{HE}:*
  Only Kool's model considers the influence of the finite thickness of the hard electrode. The additional interface causes a reduction of H_N with respect to Néel's model. For increasing t_{HE}, the Néel coupling field, H_N, increases with the total magnetic moment of the hard electrode.
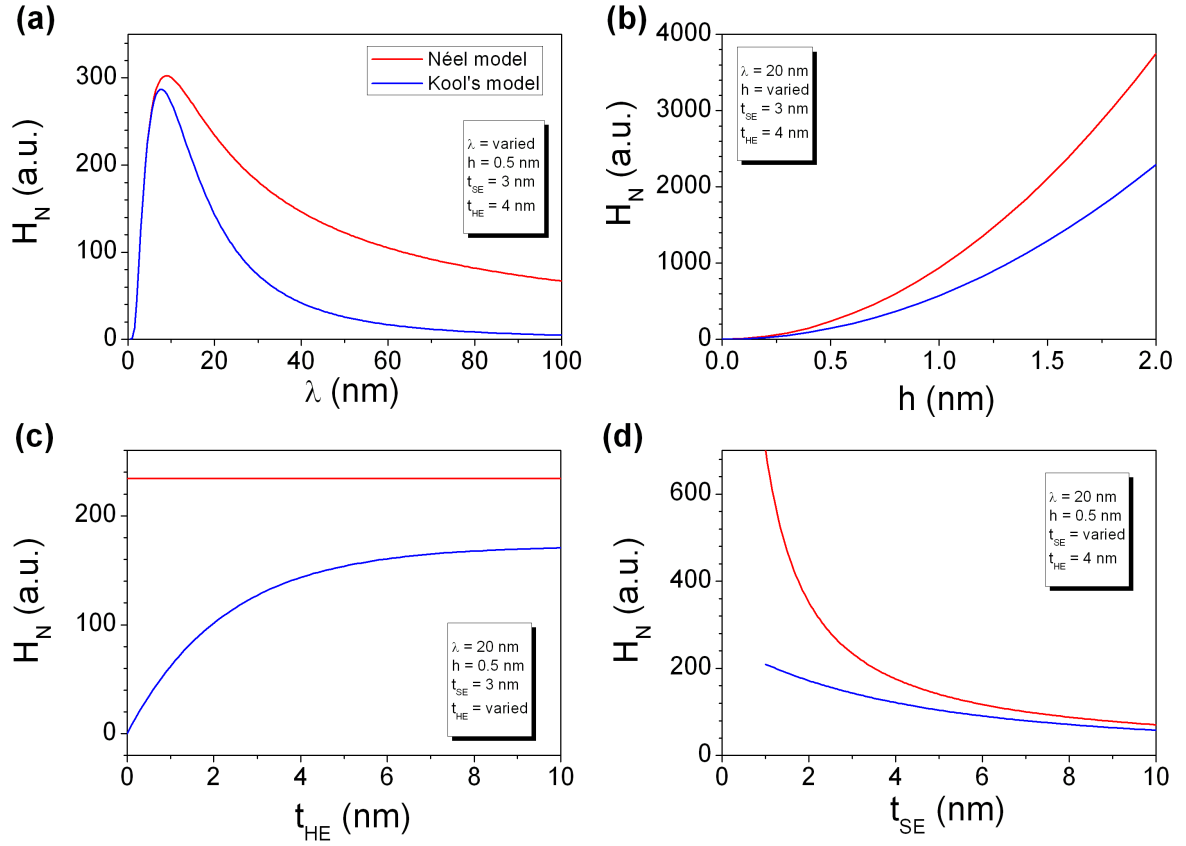
Fig. 1.7: *Calculated Néel coupling field, H_N, and its dependence on (a) roughness wavelength, λ, (b) roughness amplitude, h, (c) soft electrode thickness, t_{SE}, and (d) hard electrode thickness, t_{HE}. The red lines are the calculations for the original Néel's model with infinite thicknesses of the electrodes, the blue lines are calculations for Kool's model with finite thicknesses of the electrodes.*

Néel coupling for devices with pinned AFi hard electrodes

Kool's model can easily be extended for magnetic multilayered systems with more than two ferromagnetic layers. The model has been extended for magnetic tunnel junctions comprising an exchange biased artificial ferrimagnet as a reference electrode and a single magnetic layer as a sensing layer (soft electrode) (see, e.g., Refs. [56, 85, 86]).

Néel coupling for devices with AFi soft electrodes

In the investigation of AFi as the soft electrode in magnetic devices, it is also interesting to look at the influence of AFi layer thicknesses on the Néel coupling. Therefore, we assume a full stack system comprising a single layer hard magnetic electrode with thickness t_{HE}, a barrier of thickness t_b, and a soft electrode of an Artificial Ferrimagnet with thicknesses t_1 (first ferromagnetic layer, FM1) and t_2 (second ferromagnetic layer, FM2), separated by a non-magnetic spacer of thickness t_{NM} (see also figure 1.8(a)). For this case, the interfaces will
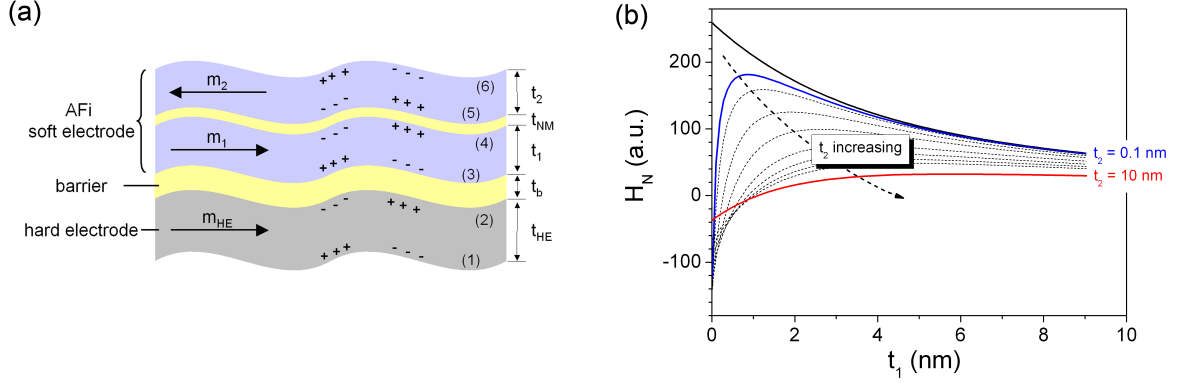
(a)

(b)

Fig. 1.8: *(a) Scheme considered for the calculation of the Néel coupling field H_N for a tunneling device with a single reference layer and an Artificial Ferrimagnet as soft electrode. (b) Calculated dependence of H_N on the AFi layer thicknesses t_1 and t_2. The use of an AFi as soft electrode in magnetoresistive devices can significantly reduce the Néel coupling in comparison to a single layer $(-)$.*

give the following contributions to the Néel coupling field:

$$
\begin{aligned}
H_{\mathrm{N,tot}} &= H_{2,3} - H_{2,4} - H_{2,5} + H_{2,6} - H_{1,3} + H_{1,4} + H_{1,5} - H_{1,6} \quad\quad (1.13)\\
&= \frac{\pi^2 h^2}{\sqrt{2}\lambda(t_1 + t_2)} M_s \left[\exp\left(-\frac{2\pi\sqrt{2}t_b}{\lambda}\right) - \exp\left(-\frac{2\pi\sqrt{2}(t_b + t_1)}{\lambda}\right) \right.\\
&\quad - \exp\left(-\frac{2\pi\sqrt{2}(t_b + t_1 + t_{\mathrm{NM}})}{\lambda}\right) + \exp\left(-\frac{2\pi\sqrt{2}(t_b + t_1 + t_{\mathrm{NM}} + t_2)}{\lambda}\right)\\
&\quad - \exp\left(-\frac{2\pi\sqrt{2}(t_{\mathrm{HE}} + t_b)}{\lambda}\right) + \exp\left(-\frac{2\pi\sqrt{2}(t_{\mathrm{HE}} + t_b + t_1)}{\lambda}\right)\\
&\quad + \exp\left(-\frac{2\pi\sqrt{2}(t_{\mathrm{HE}} + t_b + t_1 + t_{\mathrm{NM}})}{\lambda}\right)\\
&\quad \left. - \exp\left(-\frac{2\pi\sqrt{2}(t_{\mathrm{HE}} + t_b + t_1 + t_{\mathrm{NM}} + t_2)}{\lambda}\right) \right]
\end{aligned}
$$

In figure 1.8(b), the resulting Néel coupling fields depending on the AFi layer thicknesses are shown. For the calculation, the following parameters comparable to the AFi systems investigated within this thesis have been assumed: $t_{\mathrm{HE}} = 4\,\mathrm{nm}$, $t_b = 1\,\mathrm{nm}$, $t_{\mathrm{NM}} = 1\,\mathrm{nm}$, $M_s = 1000\,\mathrm{A/m}$, $\lambda = 20\,\mathrm{nm}$, and $h = 0.5\,\mathrm{nm}$. The thicknesses of the ferromagnetic layers within the AFi (t_1 and t_2) have been varied between 0 and 10 nm.

The opposite magnetization in FM2 results in a decreased Néel coupling field H_N in comparison to a single layer sample (black line). For small thicknesses of FM1, the contributions of FM2 can surpass the ones of FM1, resulting in a compensated Néel coupling field, or even a change in sign (in this example, at $t_1 \leq 1\,\mathrm{nm}$).

It is worth mentioning that the direction of the shift in a complete magnetoresistive device is influenced further by the direction of the net moment of the AFi (schematically shown in
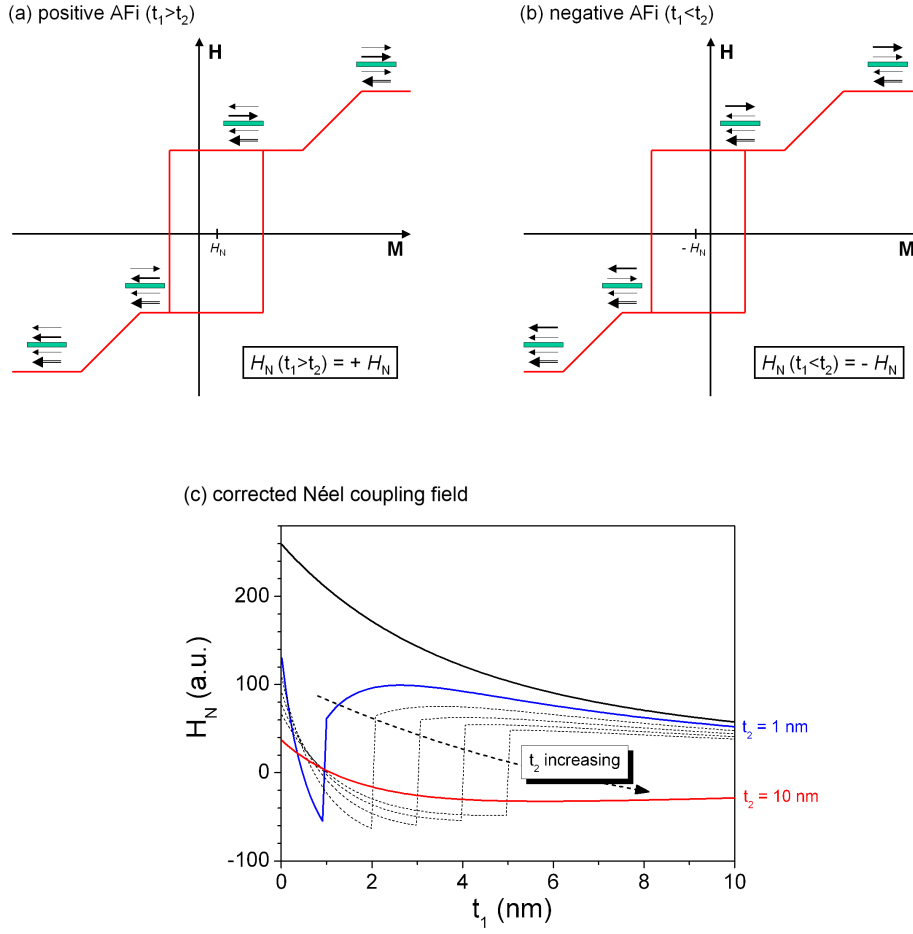
Fig. 1.9: *Schematic magnetization minor loop for (a) a positive AFi ($t_1 > t_2$) and for (b) a negative AFi ($t_1 < t_2$). The direction of Néel shift depends on the sign of net moment. (c) Calculated Néel coupling fields taking the direction of the Néel shift into consideration.*

figure 1.9(a) for a positive and (b) a negative AFi). For a positive AFi, the Néel shift acts as in a magnetoresistive device with a single layer soft electrode. For a negative AFi, the magnetization directions of the AFi layers are directed to the opposite at the ground state (at zero applied field), causing a shift to the other direction. The calculated data from equation 1.13, therefore, have been corrected by (-1) for negative AFi systems. The resulting Néel coupling fields taking this effect into consideration are shown in figure 1.9(c).

In summary, the influence of Néel coupling cannot be controlled solely by smoothness of the interfaces. A further reduction of the Néel shift is possible by using Artificial Ferrimagnets as soft electrodes. However, the above discussed instability of Néel shift around the compensation point of the two FM layers within the AFi forces one to keep a small net moment of the AFi. As we will see in the next section, it is favorable to choose a positive AFi system to sustain the possibility to compensate for stray field coupling effects in sub-micrometer scaled devices. For this reason, in section 3.4 only positive AFi systems have been patterned and investigated in sub-micrometer sizes.

1.2.4 Direct ferromagnetic coupling via pinholes

Direct coupling via defects at the non-magnetic spacer or barrier causes a ferromagnetic coupling between the two ferromagnetic layers [87]. This coupling term is one reason for a parallel orientation in AFi structures, especially if the non-magnetic spacer is thin. The direct ferromagnetic coupling via pinholes is sometimes also described as a special case of RKKY like coupling with a vanishing non-magnetic spacer, i.e. $t_{\mathrm{NM}} \to 0$.

1.2.5 Stray field or dipolar coupling

Stray field or dipolar coupling effects occur at the edges of patterned magnetic multilayers. To compensate for the magnetic poles at both ends of the patterned device, an antiparallel orientation of the soft and hard magnetic layers is favored (see figure 1.10) [87, 88]. Therefore, this coupling effect is of antiferromagnetic character, i.e. the stray field coupling acts to the opposite of the Néel coupling. The dipolar coupling energy is proportional to the magnetic moment of the ferromagnetic layers; hence, it can be reduced by compensating the moment with artificial ferrimagnets.

Fig. 1.10: *Schematics of the stray field coupling for patterned magnetic multilayer samples.*

In dense arrays of magnetoresistive devices, another type of dipolar coupling can influence the switching properties of sub-micrometer sized elements: the direct dipolar coupling between the individual elements of the array favors a homogeneous magnetization direction of all elements along the easy axis of the elements.

Further integration (i.e. decrease of lateral distance) of magnetoresistive cells in MRAM or M-Logic devices requires a reduction of the dipolar interaction between the single bits. As calculated for figure 1.11, this can be achieved by substitution of commonly used single layered soft electrodes with ones consisting of a partially compensated Artificial Ferrimagnet. For the calculation, a homogenous magnetized ellipse of 250nm×400nm has been assumed, using a saturation moment of $M_{\mathrm{s}} = 860\mathrm{kA/m^3}$ and layer thicknesses of 4nm in case of the single layer, and $t_1 = 3$nm and $t_2 = 4$nm in case of the AFi, respectively. The calculations have been performed with the LLG Scheinfein program described in section 1.5. For

Fig. 1.11: *Calculated stray fields in easy axis direction of 250nm×400nm elliptical shaped single layer and AFi elements (with a net thickness of 1nm) in dependence on the distance d from the edge of one ellipse.*

large distances between the cells ($d > 40$nm), the stray field of both the single layer and the AFi, decreases approximately with $1/d$. The stray field coupling can be reduced proportional to the net magnetic moment by the use of an AFi. The behavior of the AFi sample deviates
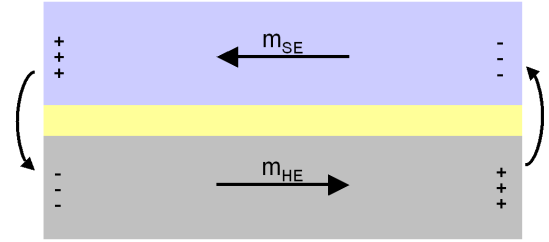
from the single layer only for small distances ($d < 40$nm). This is because of the dominating contribution of one layer near the element.

Furthermore, it has been shown that the dipolar interaction can significantly influence the switching field distribution in dense MRAM arrays [89]. If the elements are spaced closely enough, so that the magnetic dipole field from the neighboring elements is large compared to the intrinsic switching field distribution, then a significant change in the loop squareness can occur (see Ref. [90]):

- As the easy-axis pitch is reduced, a general sharpening of the transition occurs, together with a reduction in the mean switching field. The elements tend to switch in a triggered fashion and the measured switching field in this case is roughly that of the lowest switching field device along each row, with a tightened distribution.

- As the hard-axis pitch is reduced, a broadening of the transition is seen, and a slight increase in switching field occurs. This is caused by a frustrated state in which two adjacent elements lock into opposite directions of magnetization, inhibiting the complete transition of both elements, and resulting in a widened transition.

To reduce the effect of dipolar interaction on the coercivity as well as on the switching field distribution, the arrays investigated within this thesis have been patterned with large lateral distances (a pitch distance approximately three times the dimension of the elements has been chosen). A worst case scenario was calculated before the patterning process, assuming elements of a single layer magnetic material 5nm thick and a saturation moment of $M_s = 1000$kA/m^3. In a point dipole model, the cumulative stray field of the nearest neighbors is less than 1 Oe. This result is also reflected by the calculated stray field in figure 1.11, where the stray field for a single element is much less than 0.1 kA/m (for $d > 200$nm). A significant influence of stray field coupling on the coercivity and switching field distribution, therefore, can be excluded for the elements investigated within this thesis.
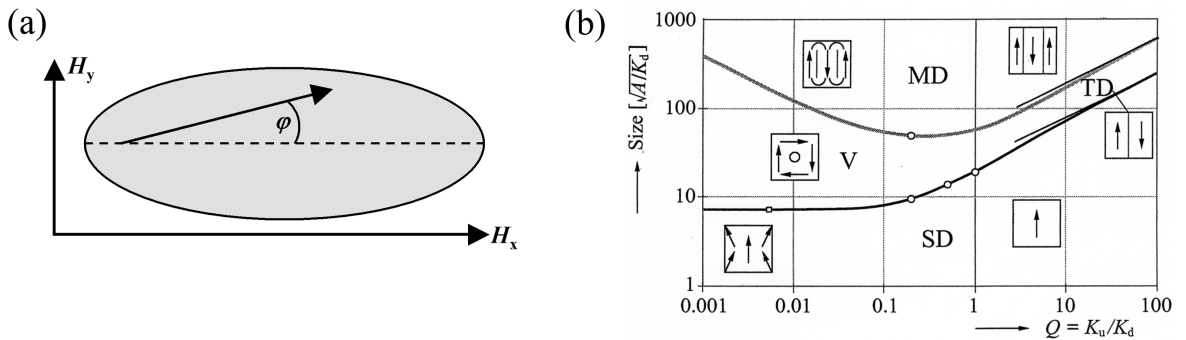

Fig. 1.12: *(a) Definition of geometry for the planar Stoner-Wohlfarth model. (b) Simplified phase diagram based on micromagnetic simulations for the presence or absence of domains, applicable to cubic particles with uniaxial anisotropy [91]. For sizes smaller than $\sim 7\sqrt{A/K}$ a single-domain (SD) state is favored.*

1.3 Magnetization reversal in sub-micrometer magnetic elements

Magnetic elements exhibit different equilibrium zero field domain states depending on their size. The magnetization reversal is strongly influenced by these domain states, as we will discuss later. Qualitatively, three kinds of micromagnetic states can be expected: the *single-domain state (SD)* for small particle sizes, the regular *multi-domain state (MD)* for large particles, and for low-anisotropy particles, an intermediate, continuously flowing or *vortex state (V)* [92]. In Ref. [91] RAVE ET AL. have calculated a phase diagram for cubic particles with uniaxial anisotropy (see figure 1.12(b)). As a critical size for a SD state, approximately 6 to 7 times the domain wall width, Δ, of a magnetic particle can be assumed. For particles with uniaxial anisotropy, Δ is given by $\sqrt{A/K_u}$ where A is the exchange stiffness constant and K_u the uniaxial anisotropy constant of the material. For the investigated CoFeB alloy, $\Delta \approx 325$nm with $A = 1.05 \cdot 10^{-6}$erg/cm and $K_u = 1000$erg/cm^3.

If the size of the elements are comparable to the domain wall width, $\Delta = \sqrt{A/K_u}$, the assumption of uniform magnetization in the element can be considered as a good approximation. Such single-domain particles can be treated using the so-called *Stoner-Wohlfarth* theory (see Ref. [93]) and the resulting switching fields can be used as a first approximation for their coercivity. Within this model, the reversal of magnetization is accomplished by coherent rotation of the uniformly magnetized sample.

1.3.1 Stoner-Wohlfarth

Considering a planar problem with the magnetization in the plane (as is the case in thin film elements), only the angle φ between the anisotropy axis (easy axis) and magnetization vector, and two components of the magnetic field, H_x and H_y, have to be taken into account (see figure 1.12(a)). The total energy of such a particle then is given by [92, 93]

$$
E_{\text{tot}} = \int \left[K_u \sin^2(\varphi) - \mu_0 H_x M_s \cos \varphi - H_y M_s \sin \varphi \right] dV \tag{1.14}
$$

where dV is the volume unit element. The magnetization vector always adjusts to its energy minimum; hence, $\frac{\partial}{\partial \varphi} E_{\text{tot}} = 0$ and $\frac{\partial^2 E}{\partial \varphi^2} E_{\text{tot}} \geq 0$ has to be fulfilled for all configurations of φ and H [93]. As the applied field, H, is varied, these minima shift position with respect to φ, reflecting the rotation of the moment, and they can also change in stability. When a minimum changes to a saddle point, the system becomes metastable and
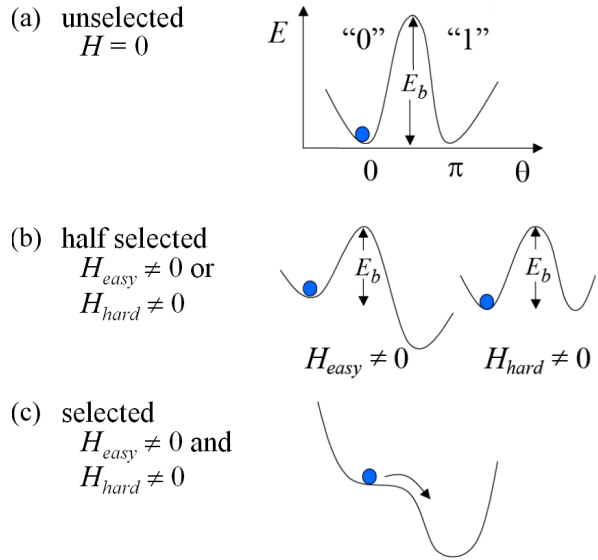

Fig. 1.13: *Energy barrier model of magnetization reversal, illustrating (a) unselected (b) half-selected and (c) selected cells in a MRAM array* [94].

jumps into an adjacent available minimum (see figure 1.13). By calculating the positions of these minima and the conditions for them to change into saddle points, one can map out the hysteresis loops as shown in figure 1.14(b).

The transition between stable and unstable energy states is defined by $\frac{\partial^2}{\partial \varphi^2} E_{\text{tot}} = 0$. If this constraint is fulfilled, the magnetization reversal happens and the switching curve $(H_{\text{x}}, H_{\text{y}})$, the so called *Stoner-Wohlfarth asteroid*, then is defined by

$$H_{\text{k}}^{2/3} = H_{\text{x}}^{2/3} + H_{\text{y}}^{2/3} \tag{1.15}$$

The calculated asteroid is plotted in figure 1.14(a) in reduced units of the magnetic fields ($h = H/H_{\text{k}}$) with $H_{\text{k}} = 2K/(\mu_0 M_s)$. It is worth mentioning that for a zero magnetic hard axis field, where $H_{\text{y}} = 0$, the switching field H_{x} along the easy axis is given by $H_{\text{x}} = H_{\text{k}}$ in accordance with equation 1.15.
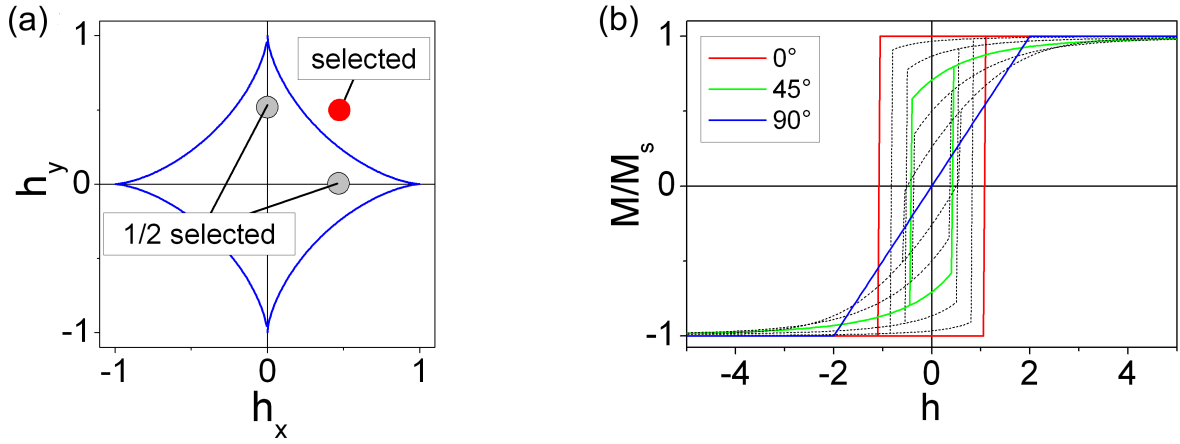

Fig. 1.14: *(a) From equation 1.3.1 calculated Stoner-Wohlfarth asteroid of an ellipsoidal, uniaxial particle. The fields are plotted in reduced units $h = H/H_k$. (b) Corresponding hysteresis loops for various angles φ.*

Addressing and switching of MRAM cells

The sub-micrometer scaled elements investigated in this thesis can be approximated by SD particles with a Stoner-Wohlfarth-like reversal mechanism (i.e. coherent rotation of the SD state). Therefore, the asteroid switching curve of magnetic elements discussed before and shown in figure 1.14(a) can be used to understand the *conventional switching scheme* in a MRAM array.[2]

Such a MRAM device consists of an array of TMR elements arranged in a matrix at the crosspoints of orthogonal metal lines (see figure 1.15). The switching of the free layer is accomplished by crossed magnetic fields, which are generated by currents applied to the lines crossing the MTJ devices. If currents are passed through two of the orthogonal conducting lines (also called *word* and *bit lines*), only the bit at the crosspoint is selected. All other bits in

---

[2]A more sophisticated writing scheme utilizing the properties of patterned AFi structures will be discussed in section 1.4.1.

the array either see only one of the magnetic fields (half selected) or no field at all (except crosstalk from neighboring current lines). For these elements, the applied field is inside the switching asteroid and the energy barrier between the two magnetization states, therefore, cannot be overcome (see figure 1.13). Only with the superposition of both fields the stability region (reflected by the switching asteroid in figure 1.14) is surpassed and the magnetization of the selected cell will flip.
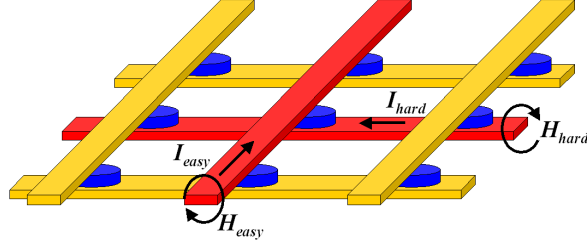

Fig. 1.15: *(a) Schematics of the bit addressing of a MRAM array [94].*

1.3.2 Demagnetization factors

The magnetic field created by the magnetic stray field inside a magnetic body tends to demagnetize the material and is called *demagnetizing field*, $\mathbf{H}_\mathrm{d}$. It acts in the opposite direction to the magnetization, $\mathbf{M}$, which creates it and is proportional to it, namely

$$\mathbf{H}_\mathrm{d} = -N_\mathrm{d}\mathbf{M} \tag{1.16}$$

where $N_\mathrm{d} \equiv \frac{n_\mathrm{d}}{4\pi}$ is the demagnetizing factor. N_d depends on the shape of the body but can only be calculated exactly for an ellipsoid where the magnetization is uniform throughout the sample [95]. For the general ellipsoid with $c \geq b \geq a$, where a,b, and c are the ellipsoid semi-axes, the demagnetization factor along these axes, n_a, n_b, and n_c, respectively, are given by

$$n_a = \frac{abc}{2} \int_0^\infty \left[(a^2 + \eta)\sqrt{(a^2 + \eta)(b^2 + \eta)(c^2 + \eta)} \right]^{-1} d\eta \tag{1.17}$$

Analogous expressions apply to n_b and n_c. The sum of all three coefficients is always equal to one [92].

For special rotational ellipsoids (e.g., prolate, oblate, or slender ellipsoid), there are analytical solutions of the integral function (see, e.g., in Refs. [95, 96]). For the magnetic patterns investigated in this thesis, the patterns can best be approximated by an ellipsoid with thickness t, length ℓ and width w under the assumption of a *very flat ellipsoid* ($t \ll w < \ell$). In this case the demagnetization factors are calculated in Ref. [97] to be

$$
\begin{aligned}
n_\mathrm{x}(u) &= \frac{u}{2} \int_0^\infty \left[(u^2 + s)\sqrt{(u^2 + s)(1 + s)s} \right]^{-1} ds \\
n_\mathrm{y}(u) &= \frac{u}{2} \int_0^\infty \left[(1 + s)\sqrt{(u^2 + s)(1 + s)s} \right]^{-1} ds \\
n_\mathrm{z}(u) &= n_\mathrm{y}(u) - n_\mathrm{x}(u)
\end{aligned}
\tag{1.18}
$$

where $u = \frac{\ell}{w}$ is the aspect ratio of the patterns. The integrands of equation 1.18 can be solved only numerically and their dependence on u is plotted in figure 1.16.
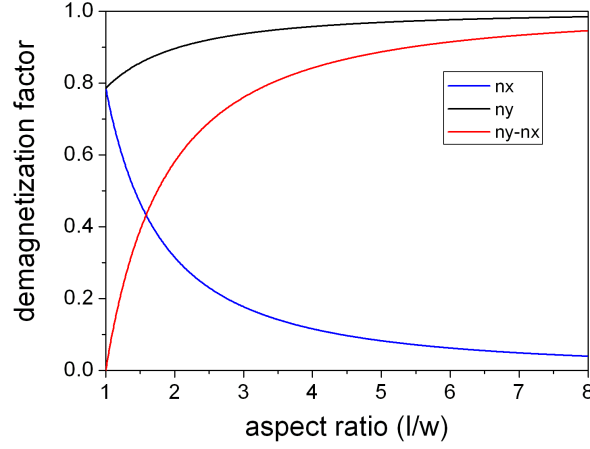
Fig. 1.16: *Calculated demagnetization factors in dependence on the aspect ratio $u = \ell/w$.*

1.3.3 Coercivity in dependence on aspect ratio

If magnetic tunneling devices are patterned into micrometer sized elements, the uniaxial anisotropy is dominated by their shape. Assuming that the elements can be approximated by an elliptical shape of the thin film thickness t, length ℓ, and width w with $t \ll w < \ell$, the uniaxial anisotropy can be derived as [97]

$$H_{\mathrm{k}} = \mu_0 M_{\mathrm{s}} \frac{t}{w} (n_{\mathrm{y}} - n_{\mathrm{x}}) \tag{1.19}$$

For the sub-micrometer scaled elements within this thesis, the switching process can be approximated by a Stoner-Wohlfarth like reversal mechanism (coherent rotation of a SD state). Therefore, the coercivity is directly linked to the shape anisotropy (see 1.3.1) and the dependence on geometry is then given by equation 1.19.

1.4 Switching of sub-micrometer sized AFi layers

The interest in small elements of the AFi system, as described in section 1.2.1, has increased in recent years. These investigations are driven mainly by several reported advantages of these systems for use in magnetic random access memories (MRAM). In such MRAM cells, the reference layer is usually an artificial ferrimagnet (AFi) exchange biased by a natural antiferromagnet. For the soft electrode, single layers of polycrystalline material, e.g NiFe and CoFe, have mostly been used [98]. Recently, soft electrodes of polycrystalline AFis, based on ferromagnetic materials like CoFe and NiFe, have been investigated. They show a further reduction of stray field due to the reduced net moment, smaller switching field distribution and an easier establishment of a single domain structure in patterned elements with small aspect ratio [61, 62].

The switching characteristics of sub-micrometer sized elements of these AFi system cannot be explained explicitly within the model that considers the AFi as one rigid ferromagnetic layer with a reduced moment. One further has to take into account the increase of effective

anisotropy due to the antiferromagnetic coupling, the dipolar coupling effects within the two layers of the AFi, and the demagnetization fields in both layers [64, 99]. Therefore, the situation in sub-micrometer sized AFi soft electrodes is much more complicated, as in the case of single layers.

WORLEDGE has presented a model describing the total energy of these systems in Ref. [99] and has extended this model to consider two FM layers with a thickness asymmetry in Ref. [100]. The fundamental assumption he makes is that the two magnetic particles (layers) can be treated as single domain elements. This assumption is a good approximation for the structure sizes of interest in this thesis, as pointed out before. Furthermore, he assumes elliptically shaped elements with an in-plane magnetization, caused by the large shape anisotropy of thin film elements ($t \ll w, \ell$). A smaller in-plane anisotropy due to the aspect ratio of the elements is directed along the long axis of the element, additionally a uniaxial intrinsic anisotropy is taken into account. Together with the Zeeman energy arising from an external applied field, the total energy density is given by [100]

$$
\begin{aligned}
e(\varphi_1, \varphi_2) =\ & -h_x \left[z \cos \varphi_1 + \cos \varphi_2 \right] - h_y \left[z \sin \varphi_1 + \sin \varphi_2 \right] \\
& + (n_x - jz) \cos \varphi_1 \cos \varphi_2 + (n_y - jz) \sin \varphi_1 sin \varphi_2 \\
& + \frac{z}{2} (n_y - n_x + h_i) \sin^2 \varphi_1 + \frac{1}{2z} (n_y - n_x + h_i z) \sin^2 \varphi_2
\end{aligned}
\tag{1.20}
$$

where $e = Ew/\pi^2 M_s^2 \ell w t_1 t_1$, $h_{x,y,i} = H_{x,y,i} w / 4\pi M_s t_1$, $j = Jw / 4\pi M_s^2 t_1^2$, $z = t_1/t_2 > 1$, E is the energy, $\varphi_{1,2}$ are the angles of the moments of the two layers measured from the x axis, H_i is the intrinsic anisotropy in the x direction, $t_{1,2}$ are the thicknesses, ℓ is length in the x direction, w is width in the y direction, $n_{x,y}$ are the reduced demagnetizing factors in the x and y directions, M_s is the magnetization, J is the exchange coupling between the layers, and $H_{x,y}$ are the applied fields in the x and y directions [100].
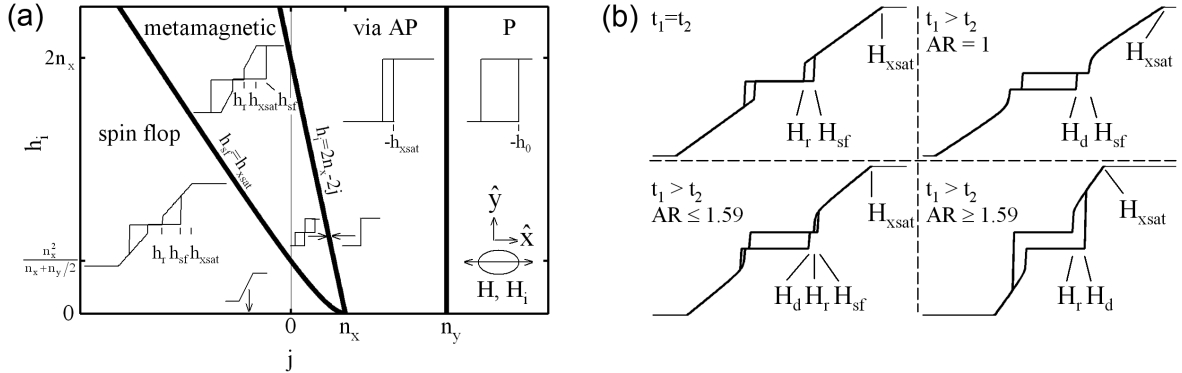
Fig. 1.17: *(a) Magnetic phase diagram for patterned AFi elements as a function of intrinsic anisotropy h_i and exchange coupling j [99]. (b) Examples of the four basic types of easy axis hysteresis loops produced by two coupled layers [100].*

By minimizing the total energy, one can map out the hysteresis loops as a function of h_i, j and the aspect ratio (which determines n_x and n_y). WORLEDGE calculated the phase diagram for an aspect ratio of $u = 2$ and a compensated AFi ($t_1 = t_2$), as shown in figure 1.17(a). For an uncompensated AFi, he figured out four basic types of easy axis hysteresis loops, shown

in figure 1.17(b). It is noteworthy that, for the loops, only the stray field coupling of the two layers within the AFi has been considered ($J_{AF} = 0$). If antiferromagnetic interlayer coupling is additionally considered ($J_{AF} < 0$), the plateau and saturation fields increase significantly. Thus, the fourth magnetization loop (bottom right in figure 1.17(b)) only occurs for very high aspect ratios [101].

Neglecting the intrinsic anisotropy,[3] the saturation field of the AFi can be expressed by two contributions: one originating from the antiferromagnetic interlayer coupling, and the other resulting from the stray field coupling. Whereas the first depends on $-\frac{J}{\mu_0}\frac{m_1+m_2}{m_1 m_2}$, as derived from equation 1.4, the latter depends on $\mu_0 M_s \frac{t_{tot}}{w} n_x$ [99], where $t_{tot} = t_1 + t_2$ is the total thickness of the AFi. The second contribution depends only on the x-component of the demagnetization factor, n_x, since the y-components in the case of an AF coupled system are compensated for external magnetic fields larger than the plateau field ($H > H_p$).

1.4.1 Spin-flop switching scheme
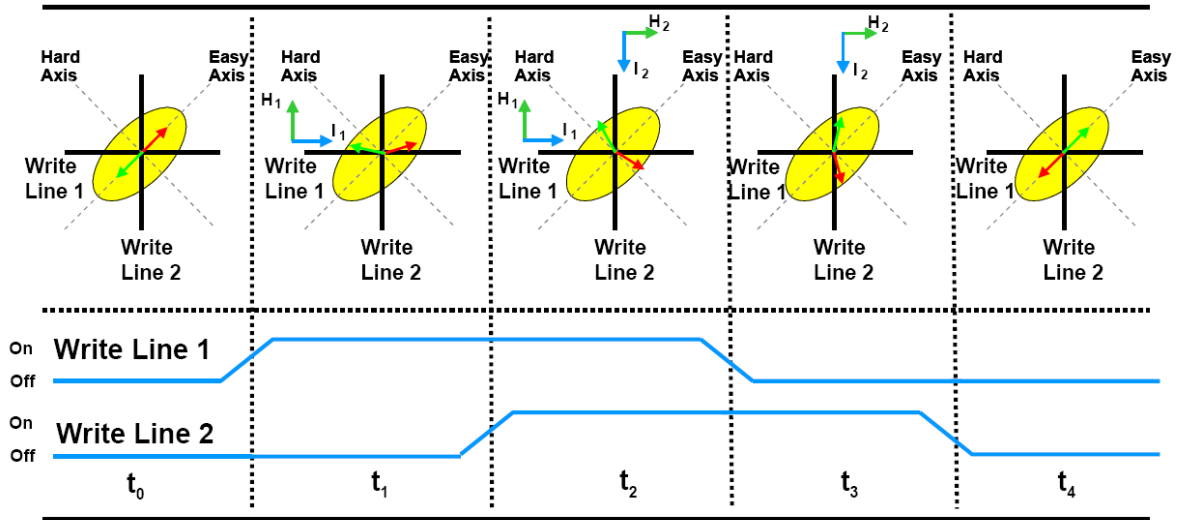
Fig. 1.18: *Schematics of the spin-flop switching scheme [102].*

The conventional MRAM switching scheme discussed in section 1.3.1 has one main disadvantage: the energized current lines reduce the energy barrier of all half-selected bits, making them more susceptible to disturbance mechanisms (see figure 1.13).

Recently, a novel switching scheme has been suggested that avoids this disadvantage. It utilizes an AF-coupled system as the soft electrode, but the magnetic bits are oriented in a 45°C angle with respect to the word and bit lines of the MRAM array [103]. A first working 4Mb MRAM device using this *spin-flop* switching (also called *toggle-bit* or *Savtchenko* switching in the literature) has been presented by Freescale/Motorola at the "International Electron Devices Meeting (IEDM)" in 2004 [102, 60].

---

[3]The intrinsic anisotropy is small in comparison to the anisotropy induced by stray field, the shape and the interlayer coupling for the samples within this thesis

The field sequence used for writing the bit and the response of the two AFi layers is shown in figure 1.18. Switching is initiated by applying two orthogonally oriented, time delayed field pulses, H_1 and H_2, oriented in-plane at $\pm 45°$ with respect to the easy axis of the elements. The switching can be separated into five time steps, t_0 to t_4. At the initial state (t_0), no external field is applied and the moments are aligned antiparallel. If only one of the field lines is energized (t_1), the magnetization vectors form a so-called *spin-flop* or *scissors state*, resulting in a small net moment along the applied field axis. If the second field is applied at t_2, this net moment is turned by $45°$ and finally by $90°$ if the first field line is switched off (t_3). These states relax to the final state if all fields are switched off (t_4) and the bit has reversed its magnetizations relative to the initial state. Because of the inherent symmetry, this sequence toggles the bit to the opposite state with respect to the existing state of the initial magnetization directions. Therefore, a disadvantage of this switching scheme is that a pre-read is necessary to determine if a write is required. The spin-flop switching, however, also has strong advantages, making it a promising candidate for future MRAM devices:

- *switching fields and write disturbance*
  The field required to switch the bit under half-select can be many times larger than the field required for full select, greatly improving the write select problem. Furthermore, the activation energy initially increases under application of a half-select field, providing greatly enhanced selectivity over the conventional approach [100].

- *scalability*
  If the elements are scaled down, the write margin, defined as $H_{\text{sat}}/H_{\text{p}}$ increases, because H_{sat} increases faster than H_{p} for small patterned elements. Furthermore, toggle cells scale better than cells used for conventional Stoner-Wohlfarth like switching, because the net moment is reduced. This greatly reduces the bit-to-bit magnetostatic interaction (see section 1.2.5) [100].

- *unipolar current drivers*
  Only unipolar current pulses are required, improving the array efficiency over conventional MRAM because the unipolar pulses do not require area-consuming drive transistors for the opposite polarity [102].

In recent publications, attention has been given to the dynamics of spin-flop switching in AFi structures [104, 105]. In these numerical calculations, it has been shown that an ultrafast writing process in less than 2.5ns can be achieved, i.e. operational speeds in the GHz regime are possible. Furthermore, NEMBACH ET AL. have shown in computer simulations that direct writing without a pre-read is possible at these speeds. Therefore, they suggest unipolar current pulses that are positively or negatively time-delayed with respect to each other [105].

1.4.2 Spin-transfer switching

So far, the presented methods to switch the magnetization in a magnetoresistive device have been based on currents generating a magnetic field. In 1996, SLONCZEWSKI and BERGER have theoretically predicted that the reversal of the magnetization can also be achieved by a current perpendicular to the plane of magnetic multilayers [9, 10]. The central idea of this novel method is a spin transfer from a polarized current to the magnetization of the free layer. In 2000, the experiments of the Cornell group at Co/Cu/Co nanopillars have demonstrated

for the first time that the magnetization of a magnetic layered structure is indeed switched back and forth by an applied current through the multilayer (critical currents of approximately $1 \times 10^7 \mathrm{A/cm}^2$ are needed) [106, 107].

Recently, spin-transfer switching at MTJs with low RA products have been reported [108]. In order to reduce the critical current density, various methods have been presented, e.g., the use of low moment free layers such as CoFeB [109], the introduction of additional scattering layers like Ru [110], and so-called *dual spin-filters (DSF)* [108].

OCHIAI ET AL. have presented spin-transfer experiments in current-perpendicular-plane GMR nanopillars with an AFi-like free layer comparable to the ones investigated in this thesis. Their experiments with spin-transfer switching show a reduction in the critical current density to $\sim 1 \times 10^6 \mathrm{\ A/cm}^2$ required to turn the magnetization. Furthermore, these AFi free layers can be switched between the two states by the same polarity of the current. These interesting behaviors of the AFi free layer is attributed to a majority electron spin transfer torque from the thick to the thin FM layer, enhanced by the presence of a Ru layer [111].

1.5 Micromagnetic simulation

Only the macroscopic model of Stoner-Wohlfarth has been discussed so far to explain the magnetization reversal in magnetic elements. Other models describing magnetic properties can be classified by their typical length scale into a hierarchy of descriptive levels[112]:

- *Phase, or magnetic texture analysis* $(> 0.1mm)$:
  The phase theory goes back to NÉEL, and describes the domain areas of equal magnetization directions as a *phase*. More generally, it describes the distribution function *(texture)* of magnetization directions. Therefore, the knowledge of single domains is not necessary in this picture.

- *Domain, or magnetic microstructure analysis* $(1 \ldots 1000\mu m)$
  Within this length scale, the *magnetic microstructure* of a sample, the shape, and detailed spatial arrangement of domains and domain boundaries are described.

- *Micromagnetic analysis* $(1nm \ldots 1\mu m)$:
  Description of the *internal magnetic structures* (including domain walls) and their substructures in terms of a continuum theory of a classical magnetization vector field. The principles of the theory go back to LANDAU and LIFSHITZ [113], and will be discussed in more detail in this chapter, since the investigated magnetic patterns can be treated within this theory due to their characteristic sizes in the sub-micrometer range.

- *Atomic level theory* $(< 1nm)$:
  Description of the origin, interaction, mutual arrangement, and statistical thermodynamics of elementary magnetic moments.

The most physical way to describe a magnetization state is achieved by the atomic level theory, which only takes into account physical *(real)* parameters and interactions (exchange interaction, crystalline anisotropy caused by the spin-orbit interaction, dimensions of atomic magnetic moments, etc.). For samples on the larger scale, a lot of atoms are involved and, therefore, a description on the atomic level is too complicated. To achieve a simplified description of the magnetization state the micromagnetic description is used that introduces phenomenological parameters (energy contributions).

Total free energy

In the micromagnetic approach, the vector field of magnetization directions is chosen so that the *total free energy* reaches a minimum [92]. We will focus first on the contributions to the total free energy of a magnetic sample:

- *Exchange energy*

  The volume exchange energy, E_{ex}, describes the preference for a constant equilibrium magnetization direction, $\vec{\mathbf{m}}$, and is the fundamental property of a ferromagnet. Deviations from this ideal case invoke an energy penalty, which can be described by [113, 92]

$$E_{\text{ex}} = \int A(\vec{\mathbf{r}}) \cdot (\nabla \, \vec{\mathbf{m}}(\vec{\mathbf{r}}))^2 \, d^3\mathbf{r} \tag{1.21}$$

  where A is the exchange stiffness constant.

- *Stray field energy*

  The stray field energy simplifies the dipole-dipole interaction between single spins by using a phenomenological quantity, as the calculation of the interactions of the magnetic moments would be very time consuming due to their long range character.

  The stray field, H_{stray}, is defined as the field generated by the divergence of the magnetization. The sinks and the sources of the magnetization act like positive and negative *"magnetic charges"* for the stray field. This stray field adds to the external field and acts like a demagnetizing field in the interior of a sample. The energy connected with the stray field is given by [92]

$$E_{\text{stray}} = -\frac{1}{2} M_{\text{s}} \int \mathbf{H}_{\text{stray}} \vec{\mathbf{m}} \, dV \tag{1.22}$$

  If the stray field energy is large in comparison to the exchange energy, as is the case for magnetically soft materials, its contribution can be reduced by forming magnetization patterns with parallel orientation to the interfaces (edges). Therefore, the reduction of E_{stray} is often one reason for domain formation.

- *Anisotropy energy*

  The dependence of the energy of a ferromagnet on the directions of the structural axes is described by the *anisotropy energy* term. This basically depends on the crystal anisotropy of the material. In the simplest case of uniaxial anisotropy, which is fulfilled for the materials investigated in this thesis [114], the anisotropy energy, E_{a}, can be described by [92]

$$E_{\text{a,uni}} = \int K_1 \sin^2(\theta) \, dV \tag{1.23}$$

  where θ is the angle between anisotropy axis and magnetization direction, and $K_{1,2}$ are the *anisotropy constants* of the material.

- *Zeeman energy*

  The interaction energy of the magnetization vector field of the sample with an external field, $\mathbf{H}_{\text{ext}}$, is given by the *Zeeman energy* [92]

$$E_{\text{Z}} = -M_{\text{s}} \int \mathbf{H}_{\text{ext}} \mathbf{m} \, dV \tag{1.24}$$

  The Zeeman energy favors the magnetization parallel to the external field. Therefore, the application of an external field causes domain nucleation and magnetization reversal in the sample.

If other energy terms, like magnetoelastic energies or anisotropy energies of higher order, are neglected, the total free energy is given by the sum of the discussed energy contributions:

$$E_{\text{f}} = E_{\text{ex}} + E_{\text{stray}} + E_{\text{a,uni}} + E_{\text{Z}} \tag{1.25}$$

Landau-Lifshitz-Gilbert equation

Micromagnetic simulations are based on a variational method which is derived from thermodynamic principles, as established initially by LANDAU and LIFSHITZ [113]. According to this principle, the vector field of magnetization directions, $\vec{\mathbf{m}} = \frac{\vec{\mathbf{M}}(\vec{\mathbf{x}})}{M_{\text{s}}}$, is chosen so that the *total free energy* reaches a minimum (under the constraint of normalization $\mathbf{m}^2 = 1$) [92].

The effective field, $\mathbf{H}_{\text{eff}}$, at the location $\vec{\mathbf{x}}$ can be described by [115]

$$\mathbf{H}_{\text{eff}}(\vec{\mathbf{x}}) \equiv \frac{\partial E_f}{\partial \vec{\mathbf{m}}} = \nabla_{\vec{\mathbf{m}}} E_f = \lambda 2\vec{\mathbf{m}} \tag{1.26}$$

where λ is a scalar called *Lagrange multiplicator*. By vectorial multiplication with $\mathbf{M}(\mathbf{x})$, one gets the equation

$$\mathbf{M}(\mathbf{x}) \times \mathbf{H}_{\text{eff}} = 0 \tag{1.27}$$

For a solution to this equation, the torque has to vanish. Therefore, the magnetization and the direction of the effective field have to stay parallel. The magnetization will vary with time as long as this condition is not fulfilled, leading to

$$\dot{\mathbf{M}} = \gamma \mathbf{M} \times \mathbf{H}_{\text{eff}} \qquad \text{or} \qquad \dot{\mathbf{m}} = \gamma \mathbf{m} \times \mathbf{H}_{\text{eff}} \tag{1.28}$$

The constant γ is called the *gyromagnetic ratio*. Equation 1.28 describes a precession of the magnetization around the effective field. During this motion, the angle between magnetization and field remains unchanged as long as no *losses* (eddy currents, Barkhausen jumps, diffusion of lattice defects, spin scattering effects, etc.) are taken into account. To describe unspecified local or quasi-local dissipative phenomena, like the relaxation of magnetic impurities or the scattering of spin waves on lattice defects, a dimensionless empirical damping factor, α_G, is

introduced in the *Landau-Lifshitz-Gilbert equation*. The damping term allows the magnetization to turn towards the effective field until both vectors are parallel in the static solution [92].

$$\dot{\mathbf{m}} = -\gamma_G \, \mathbf{m} \times \mathbf{H}_{\text{eff}} \; - \; \alpha_G \, \mathbf{m} \times \dot{\mathbf{m}} \qquad (1.29)$$

The Landau-Lifshitz-Gilbert equation is usually not solvable analytically. A magnetic state, $\mathbf{m}_L$, that minimizes the total free energy of the system, therefore, is found by numerical methods.

For the simulation of the switching behavior of the investigated samples, a commercially available simulation program was used.[4] The algorithm allows one to numerically calculate a solution to equation 1.29 for a given problem under consideration of the above described energy terms. In comparison to other codes (e.g., the *Object Oriented Micromagnetic Framework (OOMMF)* [116], the Scheinfein program allows one to easily define a multilayer problem and considers the interlayer coupling between two ferromagnetic layers, as discussed in chapter 3.1.

---

[4]LLG Micromagnetics Simulator$^{\text{TM}}$developed by M.R. Scheinfein, see http://llgmicro.home.mindspring.com

2 Sample preparation and characterization techniques

The investigated samples have been deposited, processed and characterized by different methods that will be described in the following paragraphs. The deposition was done by RF and DC magnetron sputtering processes at Siemens. For electron beam lithography, the facilities at the University of Bielefeld have been used. Most of the characterization has taken place at Siemens, using a wide range of methods, e.g., *Alternating Gradient Field Magnetometery (AGM)* and *Vibrating Sample Magnetometery (VSM)* for magnetic characterization of the unpatterned films, and spatial resolved *Magneto-Optical Kerr Effect (MOKE)* for investigation of sub-micrometer sized magnetic elements[1]. Multilayer systems for the characterization of the spin-dependent transport properties have been patterned by a simple contact mask process with ultraviolet lithography at Siemens and at the University of Bielefeld. These samples have been characterized electrically by a four-probe measurement method. Finally, the measurement setup of the high resolution magnetic force microscope (HR-MFM) at Swissprobe AG is discussed. This has been used to obtain several high resolution MFM images of antiferromagnetically coupled sandwiches and exchange bias systems.

2.1 Sample preparation and corresponding techniques

2.1.1 Thin film deposition

Several methods are used for technical thin film deposition, e.g., evaporation, Chemical Vapor Deposition (CVD), Molecular Beam Epitaxy (MBE), laser ablation, and sputtering. From the point of technical relevance, the sputtering process is the most important one, and has been used for the preparation of the samples discussed in this thesis.

Sputtering processes have various advantages [117]:

- almost any material can be sputtered - including metals, multi-component films (alloys, compounds, etc.), and insulators

- the ability to control the sputtering parameters (like pressure, sputtering gas, and energy), allows one to adjust deposition rates, thickness, uniformity and smoothness with high accuracy

- high deposition rates in comparison to other thin film deposition techniques

- scaling from laboratory devices to large scale production is possible

---

[1]The NanoMOKE2^{TM}system of Durham Magneto Optics Ltd. has been purchased and installed under my responsibility during the time of the PhD. Various hardware modifications and software add-ons have been developed by myself to implement additional measurement procedures and to automatize the standard MOKE measurements at our lab (see Appendix A).

The sputtering process involves the physical deposition of a material from a target to a substrate by the usage of a plasma. The plasma is generated from a sputtering gas; usually, an inert gas like Ar is used. Sputtering processes can be classified by the way the plasma is generated.

The easiest way to generate the plasma is the so-called *glow discharge*. The simplest setup for this consists of a constant voltage source, a cathode (positively charged) and a target material that is used as an anode (negatively charged). By applying high voltages between the electrodes, a plasma is generated, and the positive ions of the sputtering gas are accelerated towards the anode. The ions bombarding the target may have enough energy to cause the ejection of surface atoms and emission of secondary electrons, which will cause further ionization of the sputtering gas in the chamber. The principal source of electrons to sustain the plasma is the secondary electron emission caused by the bombardment of the cathode by the ions, so that a self-sustaining condition is established. The target atoms that are struck out by the ions will traverse the chamber and be deposited on the substrate. Since the chamber is large in comparison to the mean free path of the atoms, the atoms are deflected by scattering events. Therefore, a sputtering process results in an almost undirected (isotropic) deposition of the material on the substrate.

To deposit material from insulating targets (like oxide materials) a radio frequency (RF) field is used instead of the DC voltage. The RF-powered discharge operates in similar to the dc-powered. In both cases, a voltage is applied between the cathode and the anode, a breakdown occurs and a plasma is formed then sustained.

A further optimization of the sputtering process, and an increase in deposition rate can be achieved by the so-called *magnetron sputtering*. An additional magnetic field (the *magnetron field*), together with the electrical field, forces the secondary electrons into a circular orbit above the target. This enhances the density and efficiency of the plasma approximately by a factor of 10. Therefore, the magnetron sputtering can be operated with lower gas pressures and voltages in comparison to glow discharge plasmas.

A detailed description of the sputtering processes discussed above can be found, e.g., in the articles of MAISSEL and WEHNER in the "Handbook of Thin Film Technology" [117, 118].

Deposition of investigated samples

All thin film systems investigated in this thesis have been deposited by RF and magnetron sputtering using two different commercial sputtering tools, one manufactured by Leybold GmbH (Germany), the other one by Kenotec Srl (Italy). In both systems, it is possible to produce full stack GMR and TMR sequences without breaking the vacuum. A detailed control of the sputtering and oxidation conditions is possible and thin film systems with the necessary high homogeneity and smoothness over a full 3" wafer (or 5" in case of the Kenotec) can be deposited.

All samples have been deposited on thermally oxidized SiO_2 wafers at a base pressure of $5 \cdot 10^{-8}$mbar. A magnetic field of approximately 4kA/m was applied during deposition in order to induce the easy axis in the magnetic layers. Unless otherwise noted, all investigated AFi samples for use as soft magnetic electrodes have been grown on a 1.2nm thick Al layer, oxidized in an Ar/O_2 plasma for 48 seconds without breaking the vacuum, to have similar growth conditions as in a MTJ. Subsequent deposited Ta/TaN layers served as a capping layer. It has been confirmed by Auger electron depth profiling that the capping used was sufficient to protect the sample for heat treatment up to 350 to 400°C at ambient conditions.

It was the purpose of this work, to integrate an amorphous ferromagnetic alloy into the magnetic tunneling stack and to characterize these samples by various means. As the amorphous alloy $Co_{60}Fe_{20}B_{20}$ has been chosen, because of its high spin polarization leading to high TMR values [26]. For the study of artificial ferrimagnets, which are of special interest in this thesis, the ferromagnetic layer of commonly used CoFe/Ru/CoFe or NiFe/Ru/NiFe trilayers has been substituted by this amorphous CoFeB alloy, while still using the Ru as the non-magnetic spacer to mediate the antiferromagnetic coupling.

2.1.2 Lithography

For transferring patterns onto the multilayers, different lithography techniques are available. In principal, they can be divided into mask based (parallel) and writing (serial) processes. The advantage of parallel processes is a rapid duplication of images of the mask, but the disadvantage is the complicated and expensive mask production. In serial processes, a direct writing with a focused beam of electrons (e-beam lithography), ions (FIB - focused ion beam lithography) or photons (laser direct writing) is used.

For the electrical measurements of TMR junctions and the characterization of sub-micrometer scaled magnetic elements by spatial resolved MOKE experiments, different lithographical techniques have been chosen.

As the electrical measurements on full-stack elements have only been used to check the basic electrical properties of the magnetic tunneling devices, i.e. the resistance area product (RA) and the current versus voltage (IV) characteristics, a simple UV light mask lithography process was chosen. It was not the purpose of this study to investigate the electrical properties of sub-micrometer scaled TMR elements; this has been done elsewhere (see, e.g., Ref. [119]).

The sub-micrometer scale elements investigated by various measurement methods have been patterned by an electron beam (e-beam) process described later. This process has been chosen because it gives the possibility to easily write small arrays with different shapes, aspect ratios and sizes. Only by using this technique, it was possible to access the sub-micrometer range with reasonable efforts and costs. Furthermore, three different techniques have been evaluated for the use to generate sub-micrometer scaled elements on full wafer scale: *Laser interference lithography* (University of Duisburg) [120, 121], *step and flash imprint lithography* (S-FIL^{TM}by Molecular Imprints Inc.) [122, 123], and electron beam lithography at a mask producing company (ML&C Jena). All the methods had their own disadvantages. This led us to the conclude, that the conventional e-beam lithography technique described in the next section was the most flexible tool for generating the sub-micrometer scale patterns.

The sizes of the investigated patterns are in the sub-micrometer to micrometer range and are comparable to up-to-date feature sizes used for MRAM prototypes that are announced by major semiconductor companies, e.g., Freescale, Altis and Cypress. With advanced lithography processes, like *Phase-Shift-Projection*, it is possible to scale down CMOS devices to sizes smaller than the resolution limit given by the Raleigh law [124, 125]. With these methods, patterns at feature sizes of $0.09 \mu m$ are currently used in semiconductor fabrication and can also be used in the future for fabrication of magnetic memory devices (state of autumn 2005).

The investigation of magnetic and transport properties in magnetic tunnel junctions in the deep sub-micrometer range, that may find an application in MRAM devices, have been recently investigated by many groups (see, e.g., Koop et al. in Refs. [126, 127]).

E-beam lithography

Since the de Broglie wavelength of 10kV electrons is of the order of 1/100nm, the image definition of electron beam written structures is not diffraction-limited. The diameter of the spot is limited by spherical abberations in the electromagnetic lenses [128]. As an example, the minimum spot diameter of the Zeiss/LEO 1530 scanning electron microscope (SEM) used for e-beam lithography is specified as approximately 1nm [129].

As a basis for electron beam lithography, conventional scanning electron microscopes (SEM) are utilized. These microscopes can be equipped with special hard- and software, converting them to a relatively low priced lithography system for the given resolution. One of these "SEM conversion tools" has been used for preparing the sub-micrometer size samples investigated in chapter 3.4, consisting of a "Zeiss/LEO 1530"[2] electron microscope and the "Elphy-Plus" lithography system from Raith[3].

For commercial use (e.g., for mask production), special electron lithography systems with a higher wafer throughput are available. Examples of these kind of tools are *vector-scan-systems*, *spot-mask-writer*, *shaped-spot-* and *cell-projection-systems* [130].

If the electron beam penetrates the resist and the sample during the pattern writing, various interactions between the electrons and the resist or the sample occur. Some of these effects are summarized as "proximity effects" and broaden the written features, thus limiting the feature size of patterns written by electron beam lithography:

- *Backscattering and large-angle scattering:*
  The backscattering of electrons on the sample surface is a long range effect. The backscattered electrons have almost the same energies as the incoming beam and can therefore easily exposure the resist.

- *Forward scattering:*
  Electrons scattered in a forward direction within the resist broaden the volume of exposure. This can only be avoided with thinner resist thicknesses or higher acceleration voltages of the electron gun.

- *Secondary electron diffraction:*
  The generation of secondary electrons in the resist cannot be avoided. These low energy electrons broaden the exposed volume around the spot [131]. Special resists with low free mean pathes for low energy electrons have therefore been chosen.

Preparation of sub-micrometer scale structures

The sub-micrometer size samples investigated in section 3.4 of this thesis have been patterned by single step e-beam lithography and an Ar-ion etching process. A positive e-beam resist was used[4], leading to patterns with a small edge roughness and high reproducibility across the whole array. At every sample, different arrays of ellipses with a nominal width of 250nm and varying lengths have been defined. The lateral distances have been chosen to be three times the dimension of the elements. Therefore, dipolar coupling between the individual ellipses within an array can be neglected [90]. Each of the arrays extends over $25 \times 25\mu$m.

---

[2]see http://www.smt.zeiss.com for further information
[3]see http://www.raith.com/ for further information
[4]The positive, PMMA based resist AR-P 610.03 supplied by Allresist GmbH (Germany) was used. See Ref. [132] for product sheet.

After the development[5], the written patterns have been covered by a Ta layer of appropriate thickness (ranging from 8 to 15nm). This capping was removed in a lift-off process in a bath of solvent under application of ultrasonic agitation.[6] During etching with a 80 $\mu A/cm^2$ Ar ion current, the samples were tilted by approximately 30 degrees and rotated to obtain a uniform etch profile over the whole sample. The etching depth was monitored by a secondary ion mass spectrometer (SIMS) attached to the etching facility.
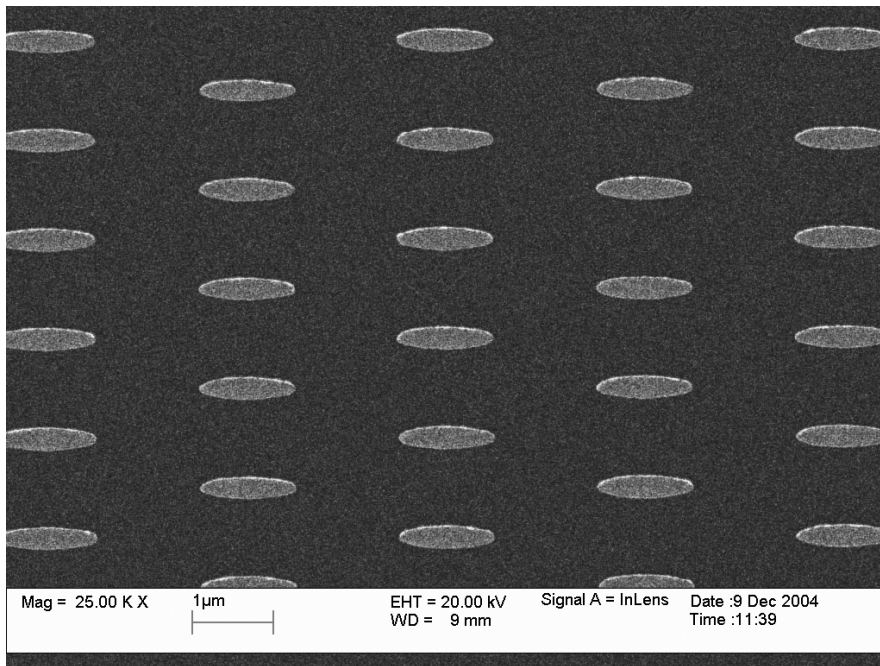

Mag = 25.00 K X	1µm	EHT = 20.00 kV WD = 9 mm	Signal A = InLens	Date :9 Dec 2004 Time :11:39

Fig. 2.1: *SEM image of one of the investigated samples, showing elliptical shaped elements of the size of* $0.27 \times 1.17 \mu m^2$.

As an example for the fabricated arrays, figure 2.1 shows a SEM image of a completely patterned array with elliptically shaped elements of $0.27 \times 1.17 \mu m^2$. The image confirms the high uniformity of the patterns. The sizes and the uniformity of all the arrays have been characterized by scanning electron microscopy after the patterning process, and show a width of 250-270nm. Due to a tendency to over-exposure, ellipses with larger aspect ratios ($u = l/w > 5$) show slightly larger widths (up to 300nm).

UV lithography

For preparation of the investigated full stack TMR junctions, a conventional photolithography process with a contact mask has been used. In photolithography processes, the sample has to be covered by a photo-resist, that shows a high absorption for wavelengths between 200 and 450nm [136]. Parallel light from a UV source is transmitted through a mask and an image of the patterns is projected onto the sample. Three different methods are commonly used in

---

[5]Developer AR 600-55 and Stopper AR 600-60 supplied by Allresist GmbH (Germany) was used. See Refs. [133, 134] for product sheets.

[6]The solvent AR 300-70 supplied by Allresist GmbH (Germany) was used. See Ref. [135] for product sheet.
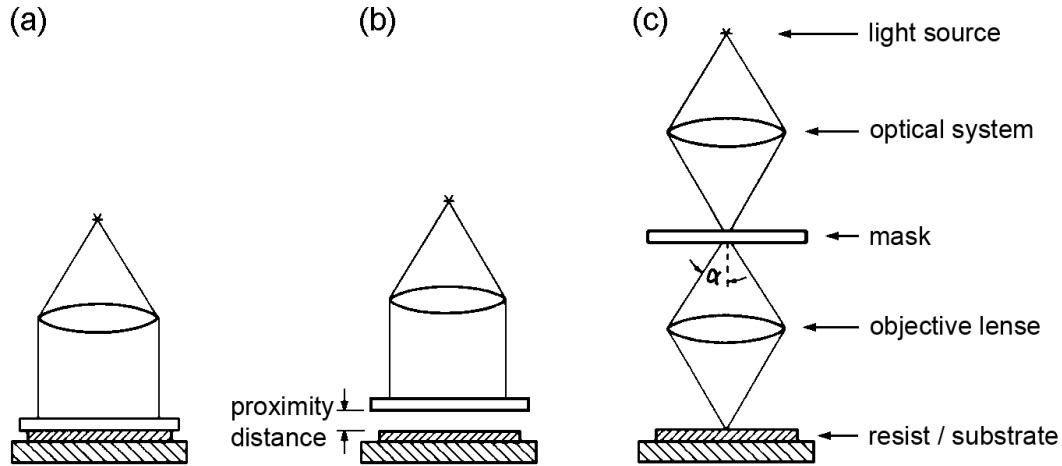
Fig. 2.2: *The basic methods of photo lithography: (a) contact, (b) proximity and (c) projection mode [136].*

lithography processes: contact, proximity and projection mode (see figure2.2) [137].

In contact mode lithography, the substrate is directly applied to the mask. Because of the direct contact, a high resolution is possible, but there is a high possibility of misalignment and defects in the resist [136]. For the investigated samples, the simple contact mask method has been chosen, since the pattern definition consisted of a single step lithography process, avoiding the problem of misalignment. As the other methods are not relevant within this thesis, a detailed discussion is omitted.

2.2 Characterization techniques

2.2.1 Alternating Gradient Magnetometery (AGM)

The Alternating Gradient Force Magnetometer (AGM) is a type of a Vibrating Sample Magnetometer (VSM), but with a higher magnetic sensitivity (10^{-8}emu). The magnetic sample is mounted on the end of a cantilevered rod that incorporates a piezoelectric element. The sample is magnetized by a dc field (variable in magnitude), and is simultaneously subjected to a small alternating field gradient. The alternating field gradient exerts an alternating force on the sample, proportional to the magnitude of the field gradient and to the magnetic moment of the sample. The resulting deflection of the cantilever rod is measured by the voltage output of the piezoelectric element. By operating at or near a mechanical resonance frequency of the cantilever, the output signal is greatly amplified [138].

A commercially available tool from *Princeton Measurement Corp.* was used for AGM measurements within this thesis. The principle setup is shown in figure 2.3. The additional *gradient* coils are put in a $(a), (-a)$ configuration and generate an alternating gradient field in the sample plane. The gradient field can be adjusted between approximately 15Oe/mm (gradient 1), 1.5Oe/mm (gradient 0.1) or 0.15Oe/mm (gradient 0.01), depending on the selected sensitivity of the tool. The field is varying with time by $Hsin(\omega t)$. The field gradient, $\frac{dH_{\mathrm{X}}}{dx}$,
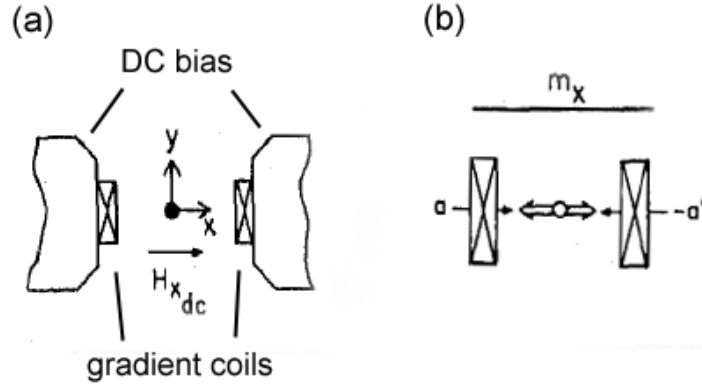
Fig. 2.3: *(a) Principal of the geometry at the AGM setup and (b) geometry of the coils generating the gradient field [138].*

exerts an alternating force proportional to the magnetic moment:

$$F_{\mathrm{X}} = m_{\mathrm{X}} \frac{dH_{\mathrm{X}}}{dx}$$

The sample is placed on a probe that is free to oscillate. The force acts on the sample and causes the probe to move with period, ωt, that is measured by piezo-electrical crystals. The fundamental resonance frequency of the probe, f_0, is given by

$$f_0 = \frac{1}{2\pi} \frac{t}{\ell^2} \sqrt{\frac{Y}{\rho}}$$

where t and ℓ are the thickness and the length of the cantilever, Y is the elastic modulus and ρ is the density [138].

Before making a measurement, the correct frequency and phase has to be found in an *autotune procedure*. During this procedure, the phase of the lock-in amplifier is adjusted so that the in-phase and quadrature output voltages, V and V^*, behave as shown in figure 2.4 when the frequency is varied. The magnetic moment, m_{X}, of the sample and the amplitude of the gradient field are held constant as the frequency is slowly varied. The mechanical gain at resonant frequency can be expressed by a quality factor, Q, which can be determined by

$$Q = \frac{f_0(V\mathrm{max})}{f_B(V\mathrm{max}/2) - f_A(V\mathrm{max}/2)}$$

Here, f_A and f_B denotes the frequencies at which the in-phase lock-in output drops to half its peak value [138].

Two things have to be considered: first, the resonance frequency is lowered by attaching a mass to the end of the rod. The mass of the sample should be chosen to be small so that the resonance frequency is not reduced below 100Hz [139]. Second, centering along the gradient axis is particularly important when measuring a material which has a low coercive field, since the net ac field from the gradient coils is only zero at the center and increases with the amount of offset along the gradient axis [138].
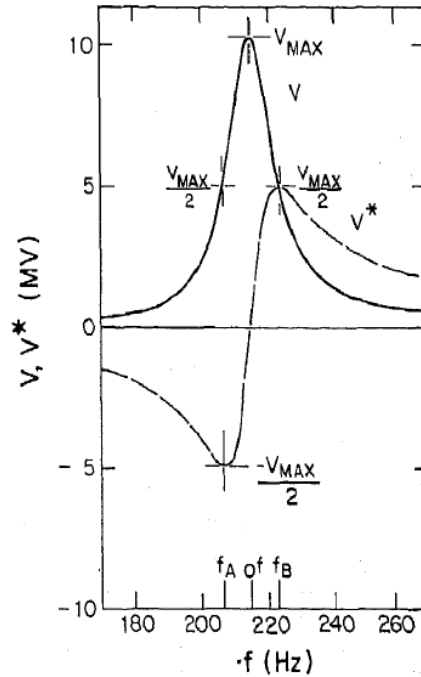
Fig. 2.4: *In-phase and quadrature lock-in output as a function of the gradient frequency [138].*

Therefore, the size of the samples measured is always a compromise between the S/N ratio (possible to increase by higher moment/larger sample or higher gradient field) and the accuracy in measuring of H_C and switching field distribution, $\sigma(H_C)$, due to the influence of the gradient field. The sample size was chosen to be $(4 - 5\text{mm})^2$ for the measurements within this thesis. For accurate evaluation of the moment, a high gradient field was chosen (15Oe/mm); for investigation of the coercivity and the hysteretic behavior, a smaller gradient field was applied (1.5 or 0.15Oe/mm).

2.2.2 Magneto-optical Kerr Effect (MOKE) Magnetometery

Observations of magnetic domain patterns by magneto-optical methods have a long history. In opaque materials, the *Faraday effect* [140], and in reflection, the *Kerr effect* is used [141, 142]. Both effects are based on changes in the properties of polarized light interacting with a material that is subjected to a magnetic field.

The Faraday effect can rarely be applied, as only few magnetic materials are transparent. Since all materials investigated within this thesis are metallic and highly reflective, only the Kerr effect is of interest here. Most of the models explaining magneto-optical effects describe the earlier discovered Faraday-effect. Nevertheless the reader should keep in mind that almost all described effects have a counterpart in the reflective Kerr effect.

The origin of the magneto-optic effect is presently described in the context of either macroscopic dielectric theory or microscopic quantum theory. In the latter, the coupling between the electrical field of light and the electron spin within a magnetic medium occurs through spin-orbit interaction. In the following we will focus on the phenomenological (macroscopic)
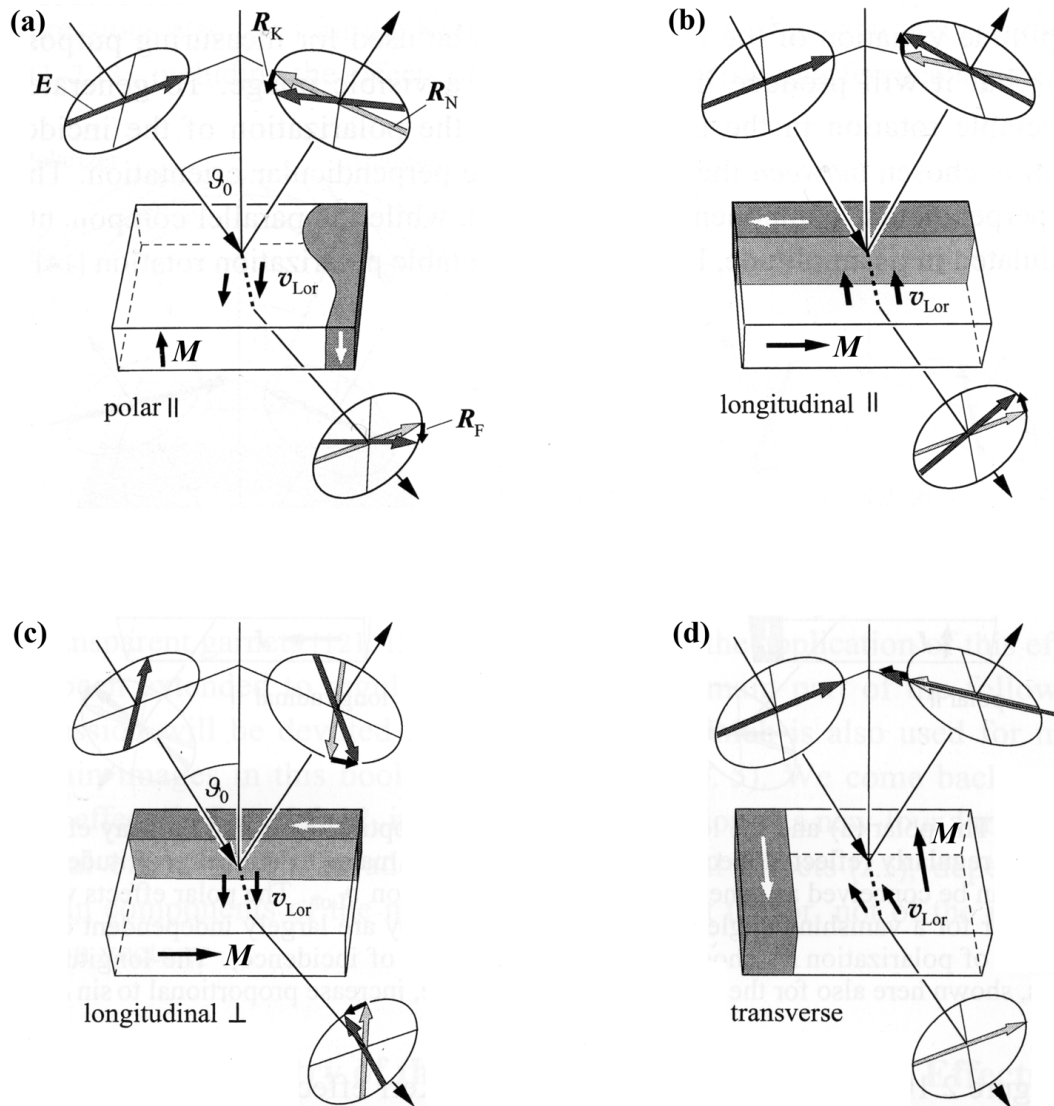
Fig. 2.5: *(a)Polar, (b) longitudinal (parallel polarization), (c) longitudinal (perpendicular polarization) and (d) transverse geometry of the magneto-optical Kerr and Faraday effect. R_N is the regularly reflected electric field amplitude. The magneto-optical amplitudes R_K and R_F are the Kerr and Faraday amplitude, respectively, and can be conceived as generated by the Lorentz motion, v_{Lor} [92].*

description, as it is based on Maxwell's discussion [143]. A complete review of the microscopic model is given in Ref. [144].

Maxwell's description of the magneto-optic effect is based on the analysis of the dielectric properties of a medium. He expressed linearly polarized light as being a superposition of two circularly polarized components. He so realized that the Faraday effect is a result of the different propagating velocities of the two circular modes. There are two processes observable in a magnetized medium. First, the two circularly polarized modes gain different phase shifts due to their different propagating velocities, resulting in a rotation of the polarization plane. This process is the conventional Faraday rotation. Second, the different absorption rates of the medium for the two circularly polarized modes affects the ellipticity. In general, both effects exist in a magnetized medium and the amount of rotation and ellipticity is proportional to a component of the magnetization [144].

There are different setups possible for MOKE experiments, depending on geometrical relations between the polarization direction, the plane of incident and the magnetization direction [92]:

- *Polar Kerr effect (figure 2.5(a)):*
  For the polar geometry, the magnetization points along the surface normal. The effect is strongest at perpendicular incidence of the beam, and it is then independent of the direction of polarization. The polar effect results in a rotation of the plane of polarization.

- *Longitudinal Kerr effect (figures 2.5(b)/(c)):*
  For the longitudinal Kerr effect, the magnetization has to be in the plane of incidence and parallel to the surface of the sample. Since the signal is proportional to $sin(\vartheta_0)$, where ϑ_0 is the angle between surface normal and the incoming beam, the signal is vanishing for an incoming beam in the direction of the surface normal. Therefore, the beam has to be inclined relative to the surface to obtain a measurable signal. Furthermore, the longitudinal Kerr effect can be differentiated into the parallel and perpendicular case, depending on the orientation of the polarization direction with respect to the plane of incident. The magnitude of both configurations is the same but of opposite sign.

- *Transverse Kerr effect (figure 2.5(d)):*
  For transverse orientation, the magnetization is perpendicular to the plane of incidence but still lies in the plane of the sample. Light of parallel polarization will result in an amplitude variation of the reflected beam. It is noteworthy that in transmission there is no transverse effect for either polarization.

Due to the chosen magnetic materials and the thin films studied within this thesis only the in-plane magnetization is of interest. Therefore, the magneto-optical setup used for the characterization utilizes the longitudinal and transverse Kerr effects. An angle of $\vartheta_0 = 45°$ has been chosen between incidence and the sample normal. In figure 2.6 the setup of the NanoMOKE2$^{\text{TM}}$ setup is schematically shown. The light is generated by a temperature and power stabilized diode laser system and has a wavelength of 635nm. The diode is specified for a maximum output power of 2.25mW (continuous wave). The emitted light is coupled into a glass fibre to obtain a single mode beam and is linearly polarized in the plane of the optical table and, therefore, it is parallel to the plane of incidence. The beam is then focused on the sample to achieve a spatial resolution of the measurement. Several lens systems are available, resulting to spot diameters of 2.8μm to 5μm for the standard quadrupole magnet system (10μm spot diameter in case of the dipolar magnet system). The beam reflected from
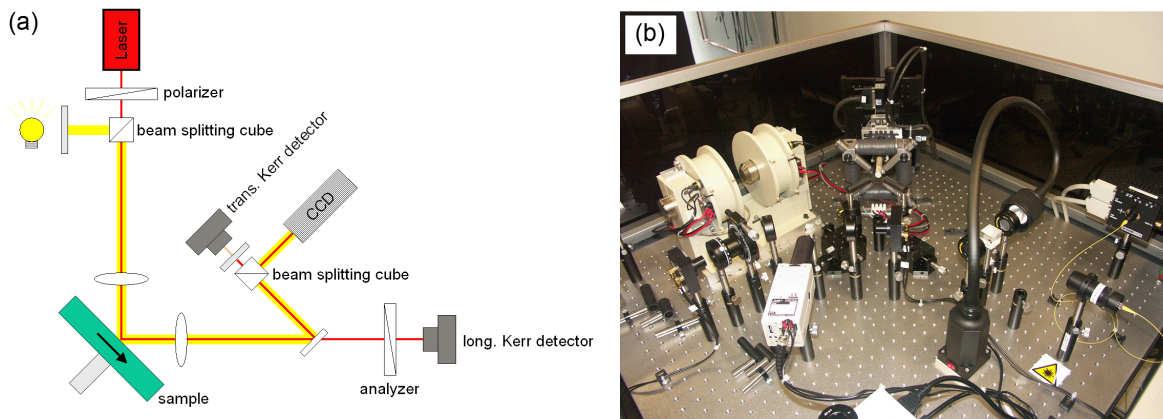
Fig. 2.6: *(a) Schematic and (b) photograph of the NanoMOKE2^{TM} setup.*

the sample is split in two components by a half-transparent mirror. The transmitted part of the beam is analyzed by a polarizer and a photo-detector, therefore detecting the longitudinal Kerr effect. Alternatively, a rotatable $\frac{\lambda}{4}$ plate (also called compensator) can be placed in front of the analyzer. This compensator converts the elliptically polarized signal back into linearly polarized light which can again be detected by the analyzer and polarizer. The reflected part from the mirror is attenuated to fit the dynamic range of a second photo detector. The signal of this detector is, therefore, sensitive to variations in the amplitude of the signal, thus measuring the transverse Kerr signal. The complete MOKE setup is sensitive to both effects (longitudinal and transverse) at the same time.

2.2.3 Scanning Electron Microscopy (SEM) and electron beam lithography

As described in section 2.1.2, a Zeiss/LEO 1530 Scanning Electron Microscope has been used for e-beam lithography. This tool has also been used for detailed characterization of the lateral dimensions of the patterned elements. Although this method has some disadvantages (e.g., no topological information can be extracted from the images, charging effects at the polymer residuals can increase the inaccuracy of the evaluated dimensions), it has been chosen for its high data acquisition rate in comparison to other methods[7].

2.2.4 X-Ray Diffractometery (XRD)

X-ray diffractometery (XRD) is a technique in which the pattern is recorded, that is produced by the diffraction of X-rays through the lattice of atoms in a specimen. This diffraction pattern is then analyzed to reveal the nature of the lattice. This leads to an understanding of several structural properties, like the crystalline, grain, defect and phase structure of the sample.

A detailed description of the XRD methods has recently been given, e.g., in the thesis of S. HEITMANN. Therefore, the reader is referred to Ref. [145] for further information.

---

[7]More than 450 arrays of sub-micrometer sized elements have been patterned and had to be characterized during these studies

2.2.5 Transmission Electron Microscopy (TEM)

For the structural investigation of full magnetic tunnel junctions, high resolution transmission electron microscopy (HR-TEM) has been used. In analogy to an optical microscope, a TEM uses a wide beam of electrons passing through a thin specimen. This transmitted beam is then projected onto the viewing screen (or CCD camera), forming an enlarged image of the specimen. Due to the above mentioned high energies of the electrons used in electron microscopes, the resolution is not diffraction-limited. The electron lenses have more imperfections or aberrations than a glass lens for light and this has important implications for the resolution of the electron microscope.

A main advantageous characteristic of a transmission electron microscope is the possibility to obtain information in real space (imaging mode) and reciprocal space (diffraction mode) almost simultaneously. Depending on the used mode, different properties of the material can be observed (see also figure 2.7) [146, 147]:
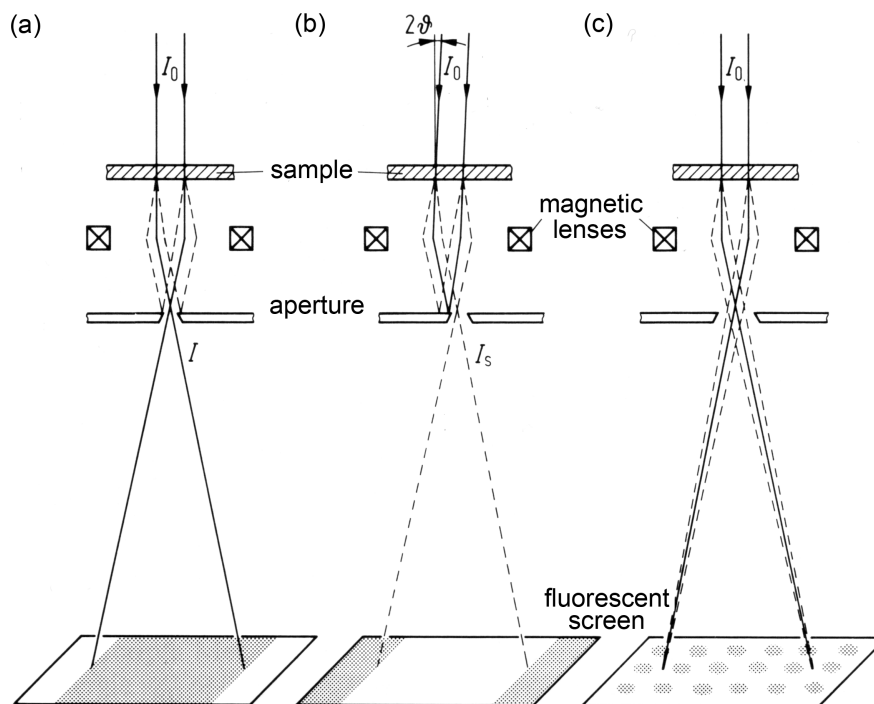

Fig. 2.7: *Schematics of the different TEM modes: (a) Brightfield (BF), (b) darkfield (DF), and (c) electron diffraction (ED) mode [146].*

- *Brightfield (BF) mode:*
  An aperture is placed in the back focal plane of the objective lens which allows only the direct beam to pass. In this case, mass-thickness and diffraction contrast contribute to image formation: thick areas, areas in which heavy atoms are enriched, and properly oriented crystalline areas appear with dark contrast.

- *Darkfield (DF) mode:*
  One or more diffracted beams are allowed to pass the objective aperture. The direct
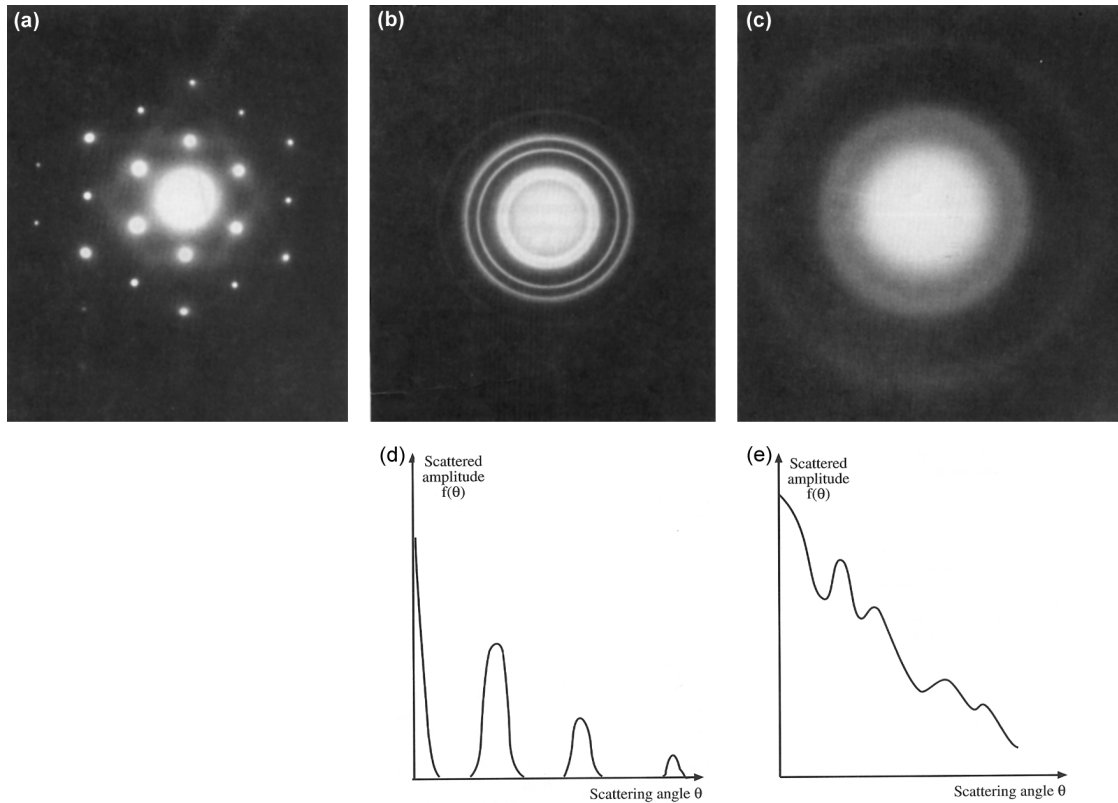
Fig. 2.8: *Several kinds of diffraction patterns obtained from (a) an Al single crystal, (b) a polycrystalline Au, and (c) an amorphous carbon sample. Change in the scattering amplitude for an (d) polycrystalline, and (e) amorphous specimen. All images are taken from Ref. [148].*

beam is blocked by the aperture. In contrast to the direct beam, the diffracted beam has interacted strongly with the specimen, and often very useful information is present in DF images, e.g., about planar defects, stacking faults or particle size.

- *Electron diffraction (ED) mode:*
  Electron diffraction is a collective elastic scattering phenomenon with electrons being scattered by atoms in a regular array (crystal). The incoming plane electron waves interact with the atoms, and secondary waves are generated which interfere either constructively or destructively with each other. The scattering event can be described as a reflection of the beams at planes of atoms (lattice planes). The Bragg law gives then the relation between interplanar distance, d, and diffraction angle, θ:

$$n\lambda = 2d\sin\theta$$

Since the wavelength, λ, of the electrons is known, interplanar distances can be calculated from ED patterns. Furthermore, information about crystal symmetry can be obtained. Consequently, electron diffraction represents a valuable tool in crystallography.

In figure 2.8, diffraction patterns obtained from different samples are exemplarily shown. In case of a crystalline sample, where all atoms are placed on a well defined lattice, the intensity

of the diffracted beams has a maximum at specific angles around the central spot, given by Bragg's equation.

In a polycrystalline film, where all crystal orientations are uniformly distributed, the diffraction pattern will consist of sharp rings around the central spot, as shown in figures 2.8(b)/(d). For an amorphous specimen, the atoms are almost (but not quite) randomly arranged. A random arrangement would result in a continuous decrease of amplitude with scattering angle, given by the so-called *scattering factor* (see e.g. Ref. [148]). However, there are certain interatomic spacings that tend to occur in an amorphous structure, e.g., first- and second-nearest neighbor spacings are usually relatively well defined. As a result, the amplitude of diffraction is stronger at some angles than at others, which we see as rings of diffuse intensity shown in figures 2.8(c)/(e).

It is, therefore, hard to distinguish between really amorphous or (sub)nanocrystalline material in diffraction mode, and this question is still debated in the scientific community. Although the diffraction pattern looks similar to that from polycrystalline material, the rings are broader and there are no diffraction spots (speckles) [148].

For further information, a complete review of all TEM methods, including electron diffraction and analytical electron microscopy, can be found, e.g., in Ref. [148].

2.2.6 Atomic Force Microscopy, Magnetic Force Microscopy (AFM/MFM)

Since the first invention of *Scanning Tunneling Microscopy (STM)* by BINNIG and ROHRER in 1982 [149], various kinds of scanning probe measurements (SPM) developed to useful tools for studying surface properties of materials from atomic to the micron size. Most common and available as commercial tools are *Scanning Tunneling Microscopes (STM)*, *Atomic Force Microscopes (AFM)* and *Magnetic Force Microscopes (MFM)*.

The basic setup for a SPM contains a cantilever with a small probe tip, a piezoelectric scanner which moves the tip over the sample, and a feedback mechanism to control the vertical (z) position of the tip. Finally, a computer is used that drives the scanner, measures and converts the data into an image.

In AFM mode, the surface of a sample is probed with a sharp tip, some microns long and often less than 10nm in tip diameter. The tip is located at the free end of a cantilever that is 100μm to 200μm long. Forces between the tip and the sample surface cause the cantilever to bend or deflect. A detector measures the cantilever deflection as the tip is scanned over the sample [150].
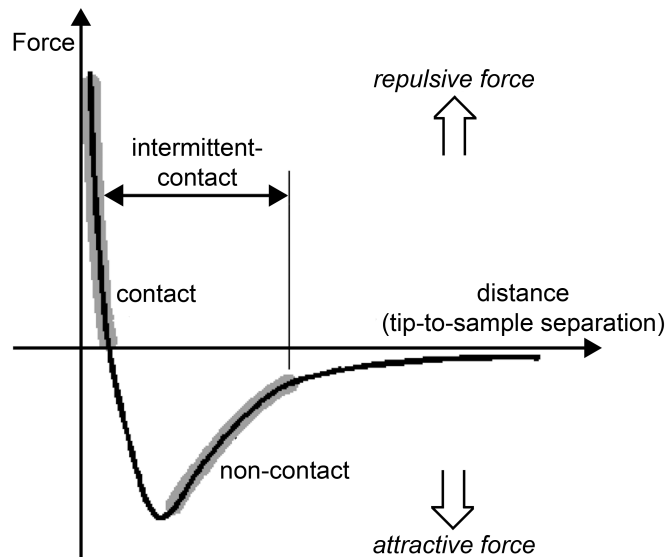

Fig. 2.9: *Interatomic force versus distance curve [150].*

The AFM cantilever is deflected by several forces between the tip and the sample. For short distances the repulsive force originated by the Pauli principle is dominating. The long-range interaction can be described by van-der-Waals forces and is attractive. The interaction between tip and sample can be described as a superposition of these forces, as for example described by the Lennard-Jones potential $V(r) \sim (r_0/r)^{12} - (r_0/r)^6$, with r_0 being the hard sphere radius. This results in the force versus distance curve schematically shown in figure 2.9. Depending on the distance between sample and tip, one differentiates between *contact mode* (repulsive range) and *non-contact mode* (attractive range) AFM.

For MFM, a magnetically coated tip is used instead of the non-magnetic one. Therefore, it is possible to additionally detect the magnetic interactions between the sample and the tip. Basically, there are two different operation modes in magnetic force microscopy possible:

- Scanning at constant distance to the sample (varying height):
  In this MFM mode each line is scanned twice in a row. For the first scan, the sample is scanned in a close distance between the cantilever and the sample. Therefore, the attractive van der Waals force dominates, and the image reflects the topological properties of the sample. In the second scan, the tip is lifted to typically $50 - 100$nm above the surface and the distance between the tip and the sample surface, acquired in the first scan, is held constant. Here, the long-range magnetic interaction between the out of plane component of the magnetization (or the stray field in case of in-plane magnetization) and the magnetic tip dominates.

- Scanning at constant height of the cantilever (varying distance):
  In this mode, the height of the tip is held constant and the deflection of the cantilever is detected while scanning over the surface. Therefore, the signal consists of a convolution of the different forces, i.e. the topological contrast and the magnetic interaction between tip and sample are superimposed. To separate the topological from the magnetic information, one has to perform two measurements on the same area with reversed magnetization of the tip.

The first method is used in the MFM setup of DI/Veeco Instruments, as it has been used for several MFM measurements. Due to problems in the signal to noise ratio and with periodic signal oscillations, the sensitivity of this tool was not sufficient to obtain satisfying images of the low moment samples under study.

The MFM measurements on sub-micrometer scaled magnetic elements presented in section 3.4.4 and 3.5 have been performed with a high resolution magnetic force microscope (HR-MFM) in a collaboration with Swissprobe AG, Switzerland. The system is operated at ambient temperature and high-vacuum conditions ($< 10^{-5}$mbar). The mechanics of this system is thermally compensated and the complete setup is thermally and acoustically insulated. Thus, the tool is specified for a spatial resolution of < 0.2nm and a magnetic resolution of < 10nm [151]. Therefore, it has been possible to image the magnetic properties of AFi samples as well as exchange biased samples with sub-micrometer sized elements.

The HR-MFM setup of Swissprobe utilizes the second measurement method, where the height of the cantilever is held fixed. As a disadvantage, one always gets a convolution of the topological contrast and the magnetic interaction between tip and sample. This measurement method has clear advantages for flat samples with low topology (e.g., harddisk media). In case of patterned samples with a pronounced topology, the scan has to be performed twice with different orientations of the tip magnetization. In order to obtain the information about

the magnetic interaction, both images have to be digitally subtracted. Since this procedure is very time consuming for the samples studied in section 3.4, the results shown are obtained in a single scan. Therefore, the presented data always contain both effects, topological and magnetical interactions.

For all presented data, the magnetic tip was magnetized with the magnetic south pole (S) at the apex of the tip. Therefore, a negative (positive) pole at the sample acts as an attractive (repulsive) force, thus originating an increase (decrease) in the detected frequency shift. Thus it is also possible to correlate the dipolar contrast at the MFM images to a magnetization configuration within the magnetic particles.

3 Results and discussion

This chapter covers the experimental results obtained on either AF coupled or exchange biased systems and their discussion. In the first part, emphasis is on the use of artificial ferrimagnets as soft magnetic electrode in magnetoresistive devices. The first section reports on the unpatterned thin film systems, and a comparison between polycrystalline AFis containing $Co_{75}Fe_{25}$ and amorphous AFis containing $(Co_{75}Fe_{25})_{80}B_{20}$ is given. In the following sections, the structural and transport properties of these systems are discussed. The fourth section covers the investigation of sub-micrometer scaled CoFeB/Ru/CoFeB systems in comparison to magnetic single layers of the same area. Finally, a short discussion is presented about the potential of CoFeB based hard electrodes in magnetoresistive devices.
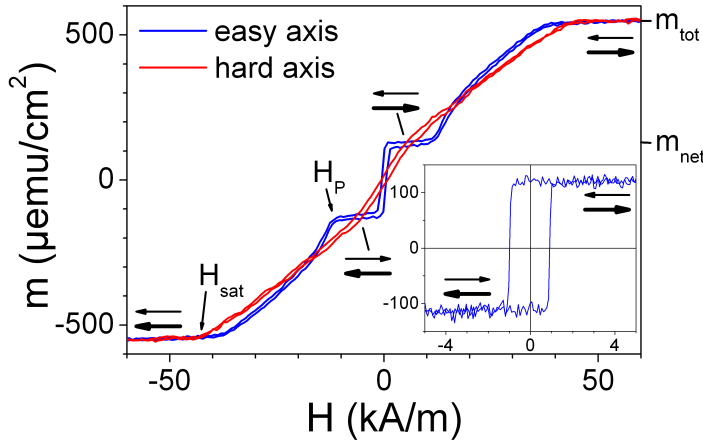
3.1 Unpatterned CoFe/Ru/CoFe and CoFeB/Ru/CoFeB

Fig. 3.1: *Major loop AGM measurement of a CoFeB(4)/Ru(1.1)/CoFeB(3) AFi in direction of easy and hard magnetization axis. The inset shows the minor loop measurement of the same sample in easy axis configuration.*

As discussed in section 1.2.1 and as described by equations 1.5 and 1.6, the concept of an artificial ferrimagnet allows one to adjust the magnetic properties of the soft layer. Compared with a single ferromagnetic layer the AFi can be regarded as a rigid magnetic body with a reduced magnetic moment and enhanced anisotropy. The gain in coercivity can be expressed by a factor $Q = \frac{m_{\text{tot}}}{m_{\text{net}}}$. The Q value and thus the coercivity of the AFi, $H_c^{\text{AFi}} = QH_c^{\text{SL}}$, can be easily tailored by modifying the thickness of the ferromagnetic layers.

So far, only AFi systems of polycrystalline materials like CoFe and NiFe have been discussed in literature. It was the purpose of the studies within this thesis to extend the knowledge of AFi soft electrodes to include amorphous alloys.

3.1.1 Experimental and simulated magnetization loops

A typical room temperature magnetization curve, $M(H)$, of an antiferromagnetically (AF) coupled system with a Ru spacer is shown in figure 3.1 after annealing at 250°C. The $M(H)$
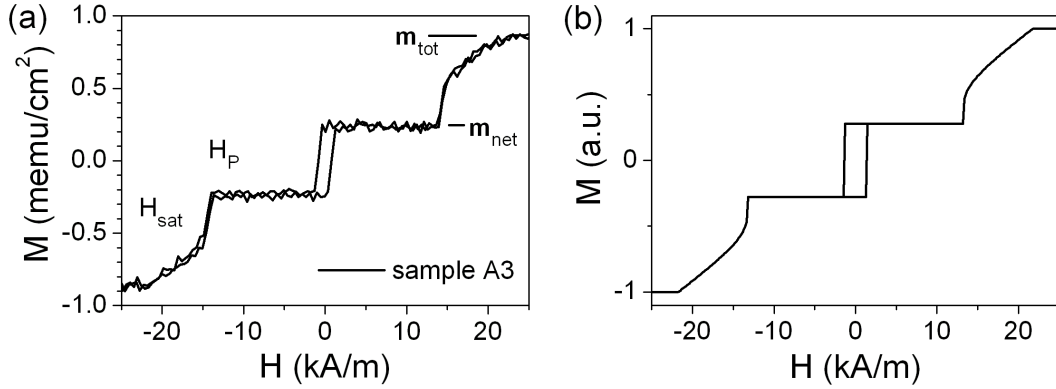
48

Fig. 3.2: *(a) Magnetization loop M(H) for sample A3 (CoFeB(4.5)/Ru(0.95)/CoFeB(3)) obtained by AGM at RT. (b) Simulated magnetization loop obtained by energy minimization of the total energy of the AFi with $J = -0.06 mJ/m^2$ and $K_u = 2000 J/m^3$, in good agreement with experimental data.*

curve shows a well defined anisotropy and a good antiparallel alignment during the magnetization reversal of the net moment of the AFi. A strong AF interlayer exchange coupling can be determined from the loop. From the AGM measurements, one can extract the saturation field, H_{sat}, the total and the net moment of the AFi, allowing calculation of the measured Q-value, $Q = \frac{m_{tot}}{m_{net}}$, the individual magnetization of the layers, $m_{1,2}$, and the coupling energy $J = -\mu_0 H_{sat} \frac{m_1 m_2}{m_1 + m_2}$. The coupling, J, of the sample shown in figure 3.1 can be evaluated to -0.071 ± 0.003 mJ/m^2.

Figure 3.2(a) shows the $M(H)$ loop of a similar CoFeB based AFi that will also be investigated in the following sections. For this sample, a slightly higher net moment and a Ru thickness of 0.95nm has been chosen. Figure 3.2(b) presents the simulated loop calculated by minimization of the total energy of the AFi. Taken into account were: the experimentally obtained moments and bilinear coupling energy, the uniaxial anisotropy energy and the Zeeman energy. No biquadratic contribution has been considered. The very good agreement of the experimental and simulated $M(H)$ loops shows that, indeed, the biquadratic term can be neglected for the samples under study.

Comparing the experimental and simulated $M(H)$ loops, one can also conclude that all samples show a very strong anisotropy at room temperature. If the coupling strength and the magnetic moments evaluated from the AGM measurements are taken into account, the experimental data are best fitted with an uniaxial anisotropy constant $K_u = 2000 J/m^3$. Most interestingly, the experimental data show a pronounced plateau and an abrupt change of the magnetization for $H > H_p$. This behavior is most likely attributed to a narrow distribution of anisotropy in the amorphous material around the easy axis of the system and is not observed in comparable stacks of polycrystalline material.

3.1.2 Coupling versus spacer thickness

In order to investigate the coupling characteristics of the CoFeB based AFi in dependence of the spacer layer thickness, a series of samples will be discussed, consisting of CoFeB(4)/Ru(t_{Ru})/CoFeB(3). The thickness of the non-magnetic Ru-spacer has been varied
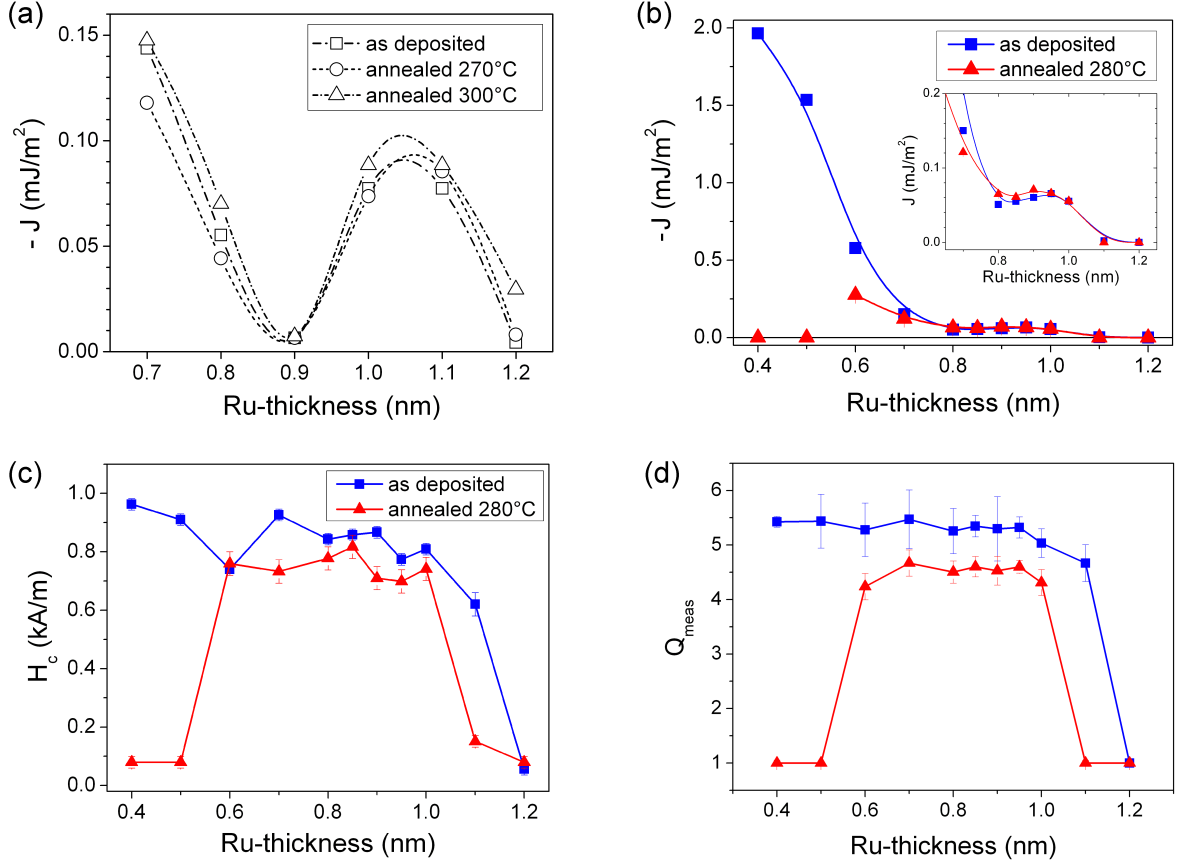
Fig. 3.3: *(a) Experimental results of coupling strength versus Ru spacer thickness, t_{Ru}, for artificial ferrimagnets of CoFeB(4)/Ru(t_{Ru})/CoFeB(3) as published in Ref. [63]. (b) Reproduced results on the Kenotec sputtering tool. The graph shows comparable oscillating behavior as in the previous case. (c) Coercivity and (d) measured Q-value versus the Ru spacer thickness for samples of the Kenotec series. Lines are guides to the eye.*

in the first series of samples between $t_{Ru} = 0.7$ and 1.2nm, in steps of 0.1nm.

The spacer layer dependence of the evaluated coupling is plotted in figure 3.3. The first graph is for AFi systems sputtered at the Leybold system and the results have been published in Ref. [63]. They show an oscillating behavior in the antiferromagnetic region in accordance with the model of interlayer exchange coupling discussed in section 1.2. The coupling has its second antiferromagnetic maximum at spacer thicknesses of 1.0 to 1.1nm and achieves a value of approximately -0.08 mJ/m^2. Therefore, the coupling is approximately by a factor of 10 lower and the second maximum of AF coupling is slightly shifted to higher spacer thicknesses than in artificial ferrimagnets of polycrystalline CoFe/Ru/CoFe [2, 56]. As will be discussed in detail in section 3.1.4, the coupling at room temperature does not change significantly after annealing treatment with temperatures up to 325°C. Nevertheless, from studies at elevated temperatures, a strong temperature dependence of the coupling is found (see section 3.1.5).

After these promising results, the same target materials have been installed in our second sputtering tool (Kenotec), and similar multilayers have been deposited. Results obtained from

the same FM combination are shown in figures 3.3(b)-(d). The basic features, i.e. the absolute value of the coupling strength and the oscillating behavior, could be reproduced. However, the position of the second maximum of AF coupling is less pronounced and shifted to slightly lower Ru-thicknesses, resulting in a maximum of coupling at $x = 0.9 - 0.95$nm. This difference of about 0.1nm (less than 1 monolayer) is most likely attributed to differences in thickness calibration of the sputtering tools.

Due to higher process stability in the Kenotec sputtering tool, a wider range of spacer thicknesses could be investigated with the second series of samples. In the "as deposited" state one achieves high coupling strength even at spacer thicknesses below 0.6nm. After annealing at 280°C, the AF coupling vanishes for these thicknesses, most likely caused by an increase in direct coupling through pinholes, but also, a ferromagnetic interlayer exchange coupling due to the RKKY like behavior is possible. Independent of the origin, the coupling is of ferromagnetic type for the annealed samples, as can be concluded from the coercivity data shown in figure 3.3(c). For stable AF coupling a H_c^{AFi} of 0.8kA/m was found, whereas the coercivity at $x < 0.6$nm decreased to ~ 0.1kA/m. Regarding the relation $H_c^{\mathrm{AFi}} = QH_c^{\mathrm{SL}}$, the system can be considered as a single ferromagnetic layer for small layer thicknesses. For large thicknesses ($x > 1.1$nm), the argument of pinholes does not hold anymore. Most likely that the system enters the regime of ferromagnetic interlayer exchange coupling, as it is described by the RKKY-like, oscillating coupling behavior.
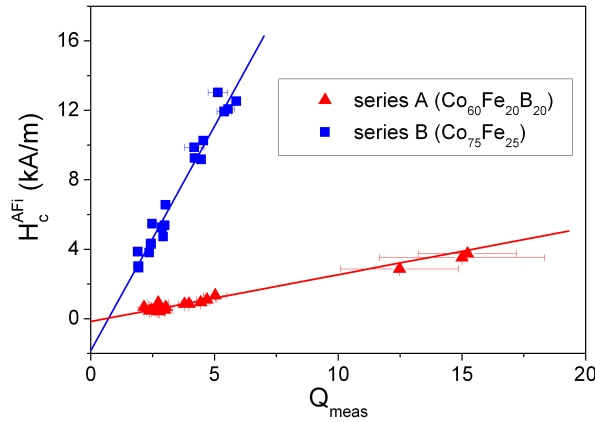
3.1.3 Dependence of coercivity on Q value

Fig. 3.4: *Dependence of coercivity on the measured Q value of CoFe and CoFeB based AFi systems. Data points shown are evaluated for all samples at different annealing conditions, increasing the number of points.*

The dependence of coercivity on the Q value will be discussed by focusing on two series of samples with varying Q values. All material systems have been sputtered starting with an Ta/AlO$_x$ seed layer to ensure the same growth conditions, as in case of the top electrode in full stack MTJ systems, and are capped with 10nm of Ta to protect them from oxidation.

Series A consists of three positive AFis of CoFeB(t_1)/Ru(1.1)/CoFeB(3). The thickness of the first CoFeB layer was $t_1 = 3.8$, 4 and 5nm, which gives nominal Q-values of 8.5, 7 and 4, respectively. Additionally, one negative AFi has been sputtered with CoFeB(3)/Ru(1.1)/CoFeB(3.8).

	Q_{nom}	Q_{meas} (ad)	Q_{meas} (270°C)	J (270°C) [mJ/m^2]
series A				
CoFeB(3.8)/Ru(1.1)/CoFeB(3)	8.5	2.7	2.5	-0.05
CoFeB(4)/Ru(1.1)/CoFeB(3)	7.0	5.0	4.0	-0.07
CoFeB(5)/Ru(1.1)/CoFeB(3)	4.0	3.0	2.7	-0.04
CoFeB(3)/Ru(1.1)/CoFeB(3.8)	8.5	9.4	15.2	-0.11
series B				
CoFe(5)/Ru(0.9)/CoFe(8)	4.3	4.2	4.3	-1.18
CoFe(7)/Ru(0.9)/CoFe(10)	5.7	5.1	5.1	-1.18
CoFe(3)/Ru(0.9)/CoFe(6)	3.0	2.9	2.9	-1.11
CoFe(3)/Ru(0.9)/CoFe(7)	2.5	2.4	2.4	-1.13
CoFe(3)/Ru(0.9)/CoFe(9)	2.0	1.9	2.0	-1.16

Tab. 3.1: *Overview of the samples considered for the study of the coupling dependence on Q value and annealing temperature. The nominal and measured Q values in the as deposited state (ad) and at an annealing temperature of $270°C$ are given. The last column shows the coupling strength, J, after annealing at $270°C$.*

Series B consists of $CoFe(t_1)/Ru(0.9)/CoFe(t_2)$ with various thicknesses t_1 and t_2, leading to nominal Q values in the range of 2 to 5.7. All investigated samples are listed in table 3.1 with their nominal and measured Q values at the given annealing conditions.

From the minor loops, one can extract the coercivities, H_c^{AFi}, of the AF coupled systems. When plotted against Q_{meas}, the coercivity shows a linear behavior as predicted by equation 1.6 (see figure 3.4). The linear fit of the data gives $H_c^{\text{AFi}} = (0.29 \cdot Q - 0.17)\text{kA/m}$ in the case of the amorphous CoFeB-AFi, and $H_c^{\text{AFi}} = (3.2 \cdot Q - 3.5)\text{kA/m}$ for the polycrystalline CoFe-AFi, respectively. Considering equation 1.6, this leads to single layer coercivities of 0.29kA/m and 3.16kA/m, respectively, in good agreement with the measured coercivity of $H_c^{\text{SL}} = 0.27$ to 0.35kA/m for a 3.5 nm thick single layer of CoFeB and $H_c^{\text{SL}} = 2.4$ to 3.0kA/m for a 5nm thick single layer of CoFe.

Due to the linear behavior, the coercivity can easily be tailored within a large window by varying the Q value of the system. Most interestingly, the coercivity of the CoFeB-AFis is approximately nine times smaller than in artificial ferrimagnets consisting of polycrystalline $Co_{75}Fe_{25}$ (see figure 3.4), qualifying this AFi-system as an promising material combination for soft magnetic electrodes in magnetoresistive applications.

For all CoFeB samples it is found that Q_{meas} depends slightly on the annealing temperature. For samples of series A, Q_{meas} significantly deviates from the nominal Q value. This is most likely attributed to microstructural differences between the two series, originated by the use of two different sputtering tools for sample preparation. The discrepancy between nominal and measured Q values in the case of series A can be explained by the observed thicker magnetically dead layers of the upper CoFeB layer in comparison to the bottom layer. This already holds in the "as deposited" state. As verified by Auger depth profiling, the capping layer of 10nm of Ta protects the multilayers against oxidation up to annealing temperatures of 400°C [152]. This ensures that the difference in the magnetic dead layer thickness between the two CoFeB layers originates from a stronger intermixing of the upper CoFeB interfaces rather than an
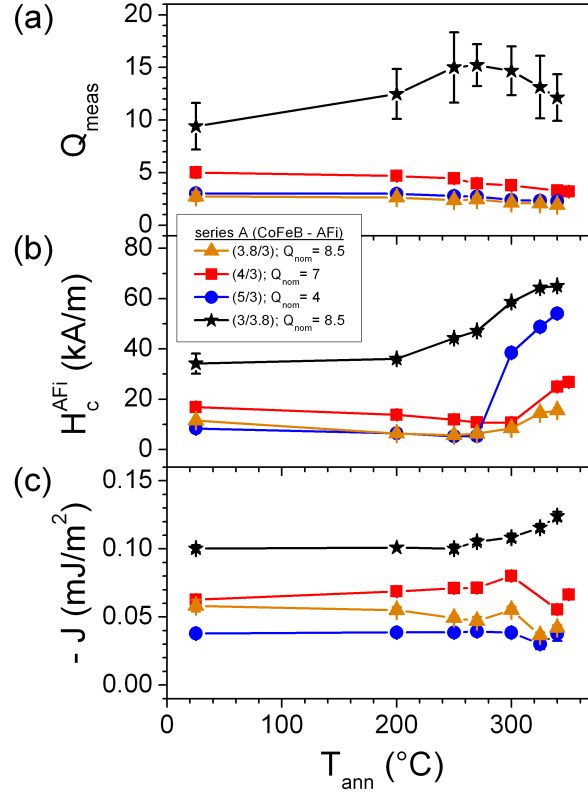
Fig. 3.5: *(a) Measured Q value, (b) coercivity H_c^{AFi} and (c) coupling J of the CoFeB-trilayers versus annealing temperature T_{ann}. The values in parentheses are the nominal layer thicknesses, t_1 and t_2, of the AFi.*

oxidation of the upper layer. This leads to an increase in m_{net} and, therefore, a decrease in Q_{meas} in the case of the *positive* AFis. For the same reason the *negative* AFi of series A shows a much higher Q_{meas} in comparison to the nominal Q of 8.5.

3.1.4 Annealing temperature dependence and stability

As already presented in figure 3.3(a), the coupling at the second AF maximum remains stable against annealing up to more than 300°C. It was the purpose of a further study to investigate the magnetic properties of the CoFeB-AFi in dependence of the annealing conditions. Therefore, the samples of series A have been annealed on a hot plate at constant temperatures between 200 and 350°C for 15 min and have been protected from oxidation by a constant Ar-flow. The ramp-down times varied between 1 and 2 hours, depending on the applied annealing temperature. A field of approximately 400 kA/m was applied along the deposition-induced easy axis during annealing and cooling.

All samples were then investigated by Alternating Gradient Magnetometry (AGM). From the major and minor loops, the key parameters characterizing the magnetic properties have been extracted: the saturation field of the AFi (H_{sat}), the plateau field (H_p), the total and net area magnetization (m_{tot} and m_{net}, respectively), and the coercivity (H_c^{AFi}). From these data, one can calculate the coupling strength, J, and the measured Q. All data evaluated from
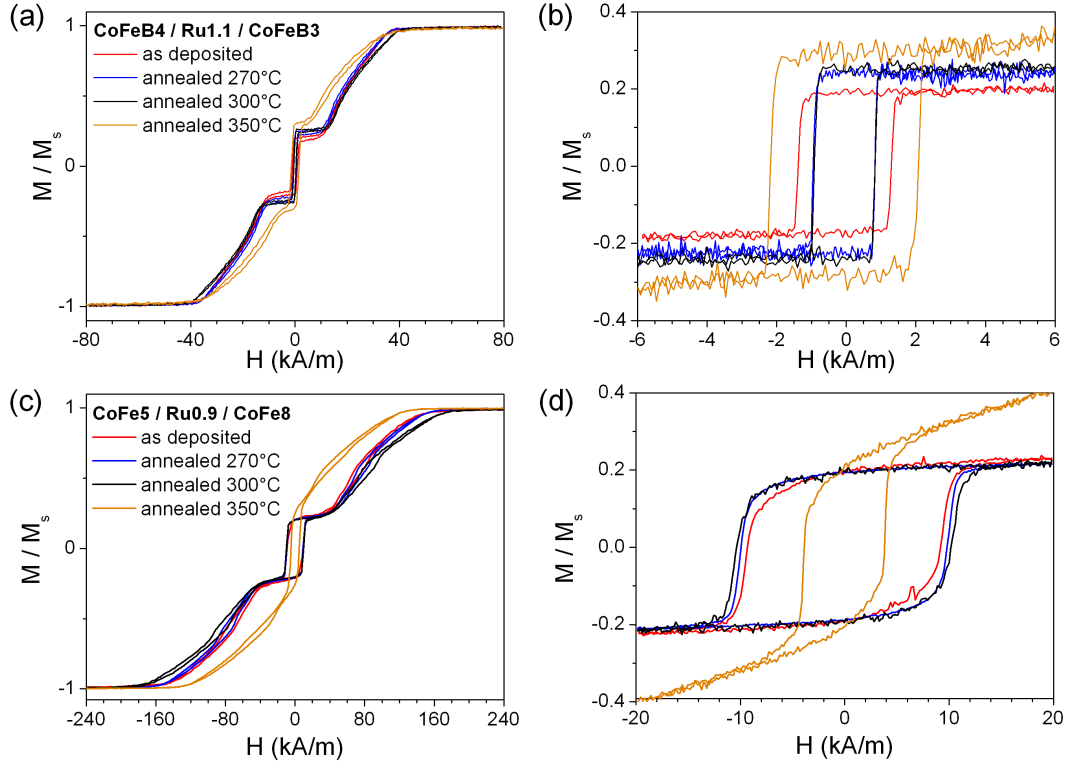
Fig. 3.6: *(a)/(b) Major and minor loop magnetization measurements of a CoFe based AFi of series B, and (c)/(d) for a CoFeB based AFi of series A in dependence on the annealing temperature.*

series A are shown in figure 3.5.

Apart from the significant deviation of the measured Q value to the nominal one, as discussed before, a slight decrease with annealing temperature is found for the *positive* AFis (see figure 3.5(a)). In the case of the *negative* AFi, a strong increase of Q value for temperatures up to 270°C is found, which is also reflected by a constant rise in coercivity in this temperature range, as expected by equation 1.6.

However, the increase of coercivity for $T_{ann} > 300$°C is also seen in the *positive* samples of series A, where the argument of an increasing Q value does not hold. For those systems, the coercivity slightly decreases in the temperature range of 200 to 300°C and for temperatures higher than 300°C, it strongly increases (see figure 3.5(b)). This abrupt increase is observed regardless of the thickness of the CoFeB and the materials interfacing it. This strongly suggests that the origin of the coercivity increase at these temperatures is not caused by interdiffusion, but by the change from amorphous to polycrystalline phase as reported for other CoFeB alloys [153]. Furthermore, the same abrupt increase of coercivity is also seen in tunnel junctions using a single layer of CoFeB as the soft electrode in the same temperature window [152].

The third key factor affecting the coupled trilayers is the coupling energy; this can be evaluated from the experimental data using equation 1.4. As can be seen in figure 3.5(c), the coupling is already set in the "as deposited" state for all samples. In the temperature window between 300°C and 340°C, the coupling decreases. Above 340°C, the plateau field, H_p, quickly

disappears. Figures 3.6(a) and (b) show the major and minor loops for different annealing temperatures of CoFeB(4)/Ru(1.1)/CoFeB(3). A similar behavior of the magnetization loops is found for the CoFe based AFi of series B as shown in figures 3.6(c) and (d). It is worth mentioning that for $T_{ann} > 340°C$, the saturation field is still pronounced for both samples, excluding the possibility of pinhole formation at this temperature because a direct FM coupling would result in an abrupt switching of the two layers at a much lower coercivity. Therefore, the vanishing plateau is either related to an increase in the distribution of the anisotropy direction or to a transition from a bilinear to a dominating biquadratic coupling [154].

The AF coupling strengths, $J_{af} = -J$, varies for the *positive* samples of series A between 0.037 and 0.063mJ/m^2, whereas the *negative* AFi shows a coupling of 0.12mJ/m^2. This discrepancy can be explained by the fact that the magnetic dead layer thickness is larger for the upper FM layer. In the case of the *negative* AFi, this leads to a decrease of its net moment with a resulting increase in the saturation field and in J_{AF}. Nevertheless, as a first approximation, the coercivity of the unpatterned AFi systems can be considered to be independent from the absolute value of coupling for the samples under study. This is confirmed experimentally by the linear behavior of the coercivity versus Q value in figure 3.4. To further prove this assumption, calculations of the magnetization reversal in dependence on the coupling have been performed within the simple energy model of the unpatterned AFi presented in section 1.2.1. The resulting dependence of coercivity on the

Fig. 3.7: *Dependence of the normalized coercivity, $H_c/H_c(J_{af} = 10mJ/m^2)$, on the AF coupling strength, $J_{af} = -J_{lin}$. The datapoints have been obtained by simulation using the energy model of the AFi presented in section 1.2.1.*

coupling strength, J_{af}, is shown in figure 3.7. For small coupling strength, the coercivity is strongly increasing and it asymptotically reaches a constant value for large coupling strength. The experimental window of J_{af} is indicated in the plot, and a change in coercivity by the increasing coupling strength is less than 10%, thus underlining the aforementioned assumption.

In summary, the CoFeB/Ru/CoFeB sandwiches exhibit a stable coupling for annealing up to $T_{ann} \approx 325°C$. The onset of transition from a bilinear to a biquadratic dominated coupling takes place at similar annealing temperatures as it is the case at the polycrystalline CoFe samples. At the same time, the coupling energy, J, of the CoFeB based AFis is in the order of $-0.1mJ/m^2$; this is by one magnitude smaller than in polycrystalline CoFe based AFis. The coercivity of the amorphous AFi is by a factor of nine smaller than in the polycrystalline samples and scales linearly with the measured Q-value. Combined with the high spin polarization of this CoFeB alloy, reflected by a measured TMR effect of approximately 70% [26], this material system may be a potential candidate as a soft magnetic electrode in magnetic tunnel junctions. Therefore, the CoFeB based AFi will be investigated in sub-micrometer scale elements in section 3.4.
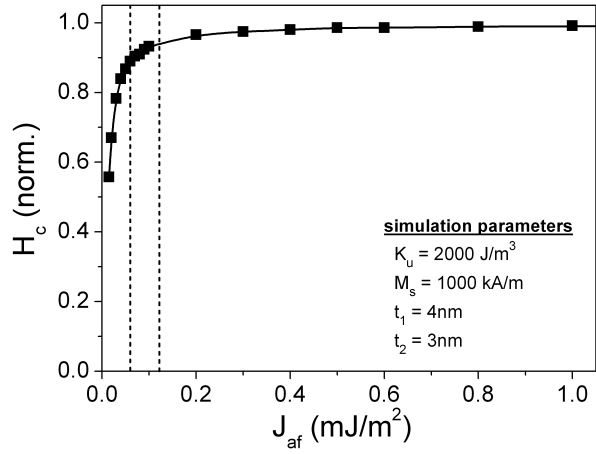
	H_{sat}^{AGM} $\left[\frac{kA}{m}\right]$	J^{AGM} $\left[\frac{mJ}{m^2}\right]$	$H_{sat,0}$ $\left[\frac{kA}{m}\right]$	T_0 [K]	v_F $\left[\times 10^7 \frac{cm}{s}\right]$
series A CoFeB(t_1)/Ru(0.95)/CoFeB(3)					
A1: $t_1 = 3.5$	29.8	-0.060	53.4 ± 0.6	142.9 ± 1.2	1.12 ± 0.01
A2: $t_1 = 4$	26.3	-0.060	44.1 ± 0.4	149.8 ± 1.3	1.18 ± 0.02
A3: $t_1 = 4.5$	23.9	-0.060	40.4 ± 0.2	146.2 ± 0.7	1.14 ± 0.01
series B CoFeB(3.5)/Ru(t_{Ru})/CoFeB(3)					
B1: $t_{Ru} = 0.8$	23.9	-0.061	50.3 ± 0.7	140.7 ± 1.4	0.93 ± 0.01
B2: $t_{Ru} = 0.85$	23.1	-0.053	49.0 ± 0.7	135.3 ± 1.3	0.95 ± 0.01
B3: $t_{Ru} = 0.95$	29.8	-0.060	53.4 ± 0.6	142.9 ± 1.2	1.12 ± 0.01
B4: $t_{Ru} = 1.0$	19.1	-0.036	48.2 ± 0.4	120.0 ± 1.3	0.99 ± 0.01
B5: $t_{Ru} = 1.05$	10.7	-0.022	33.4 ± 0.4	103.2 ± 1.4	0.89 ± 0.01

Tab. 3.2: *Saturation field (H_{sat}^{AGM}) and coupling strength (J^{AGM}) evaluated from AGM measurements, zero temperature saturation field ($H_{sat,0}$), characteristic temperature (T_0) and Fermi velocity (v_F) evaluated from fittings of the experimental data with equation 1.8.*

3.1.5 Temperature dependence of AF coupling

The reliable switching of sub-micrometer sized elements in dense MRAM arrays is limited by the thermal stability limit of the elements; this is comparable to the problem in magnetic storage devices [155]. To increase the thermal stability, materials with high intrinsic or shape anisotropy have to be used in order to increase the relative energy barrier (see figure 1.13). As a drawback, the coercivity of the magnetic bits is also increasing, which therefore increases the currents needed for reversing the magnetization of the bits. To compensate for this disadvantage, a heat assisted writing scheme for magnetic elements has been suggested [156].

Recently, the so called *spin-flop switching* has been announced for use in MRAM, using artificial ferrimagnets (AFi) as a soft magnetic electrode and the concept of bit toggling rather than switching [60]. As already discussed in section 1.4.1, the spin-flop or plateau field, H_P, has to be overcome in this novel switching scheme, thus inducing a net moment of the magnetizations of the AFi electrode. The bit is then reversed by a rotation of the net moment.

To combine both approaches, namely the heat assisted writing in a spin-flop switching scheme, it is necessary to gain a deeper knowledge of the temperature dependence of coupling. It was the purpose of this study to investigate the saturation field (and therefore the coupling strength) and the plateau field in CoFeB based AFi systems in an operating range from RT to 330°C. Due to the stable coupling up to $\sim$ 350°C and the high TMR values that have been obtained with these CoFeB alloys, the CoFeB based AFi is also a promising candidate for integration as a soft magnetic electrode in MTJs, while using thermal assisted spin-flop switching.

Theoretical models predict a temperature dependence of the coupling as discussed in section 1.2.1. From Equation 1.7, it can be derived that the saturation field should behave as $H_0 \frac{T/T_0}{\sinh(T(T_0))}$ with the characteristic temperature given by $T_0 = \frac{\hbar v_F}{2\pi k_B t_{NM}}$. For Ru, the Fermi velocity is of the order of 10^7cm/s, and therefore about one order of magnitude smaller than in

most non-magnetic metals [54]. This comparable low Fermi velocity results in a characteristic temperature of ~ 100K, originating a strong temperature dependence of coupling versus temperature in Ru based FM/NM/FM trilayers.

As listed in table 3.2, two series of samples have been prepared. In series A, the thickness t_1 of the magnetic layer in contact with the AlO_x was varied from 3.5 to 4.5nm, in steps of 0.5nm (CoFeB (t_1)/Ru(0.95)/CoFeB(3)). In series B, the Ru thickness (t_{Ru}) was varied from 0.8 to 1.05nm around the 2nd AF coupling maximum, while using an almost compensated CoFeB(3.5)/Ru(t_{Ru})/CoFeB(3) AFi. After deposition, all samples were heat treated at 300°C for 10min. and cooled down to room temperature (RT) under application of a constant magnetic field of ~ 40kA/m, which is well above the saturation field, H_{sat}^{AGM}.
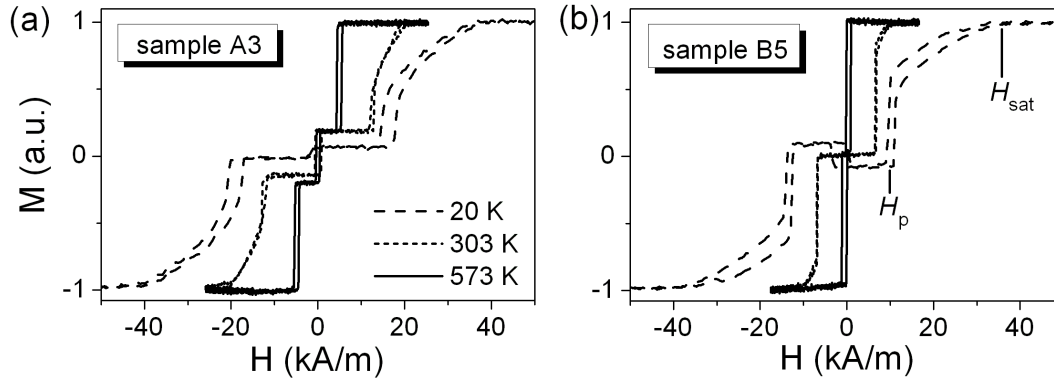

Fig. 3.8: *Magnetization loops at various temperatures, $M(H,T)$, obtained by MOKE for (a) sample A3 and (b) sample B5. See table 3.2 for nomenclature of the samples.*

Before performing the MOKE measurements with varying temperature, M(H) loops of all samples have been obtained by alternating gradient field magnetometery (AGM) at room temperature (RT). From these measurements, it was possible to evaluate the saturation field, H_{sat}^{AGM}, as well as the net and total magnetic moment, thus allowing calculation of the coupling, J^{AGM}. As an example, a magnetization loop of sample A3 has been already presented in figure 3.2(a). The coupling strength has a constant value of -0.06mJ/m^2 for the samples of series A, whereas for series B, the coupling strength varies with spacer thickness from -0.02 to -0.06mJ/m^2 with the maximum for $t_{Ru} = 0.95$nm, in accordance with the oscillating behavior presented before. All results of the AGM measurements are listed in table 3.2.

The temperature stage of the MOKE setup (see appendix A for details) enabled us to obtain magnetization loops of the samples at varying temperatures between room temperature and 330°C. Additionally, low temperature measurements have been performed in a similar NanoMOKE^{TM} setup by J. Nogues and J. Sort in a temperature range between 10K and 300K.[1]

With both setups, magnetization loops have been recorded in a temperature range from 10K to 600K in steps of 10K. Due to the strong dependence of coupling in the CoFeB/Ru/CoFeB trilayers, a strong decrease of saturation and plateau field with the temperature is expected. Some of the temperature dependent magnetization loops, $M(H,T)$, for samples A3 and B5

---

[1] The low-temperature measurements have been performed in a collaboration with the Institucio Catalana de Recerca i Estudis Avancats (ICREA) at the Departament de Fisica, Universitat Autonoma de Barcelona.
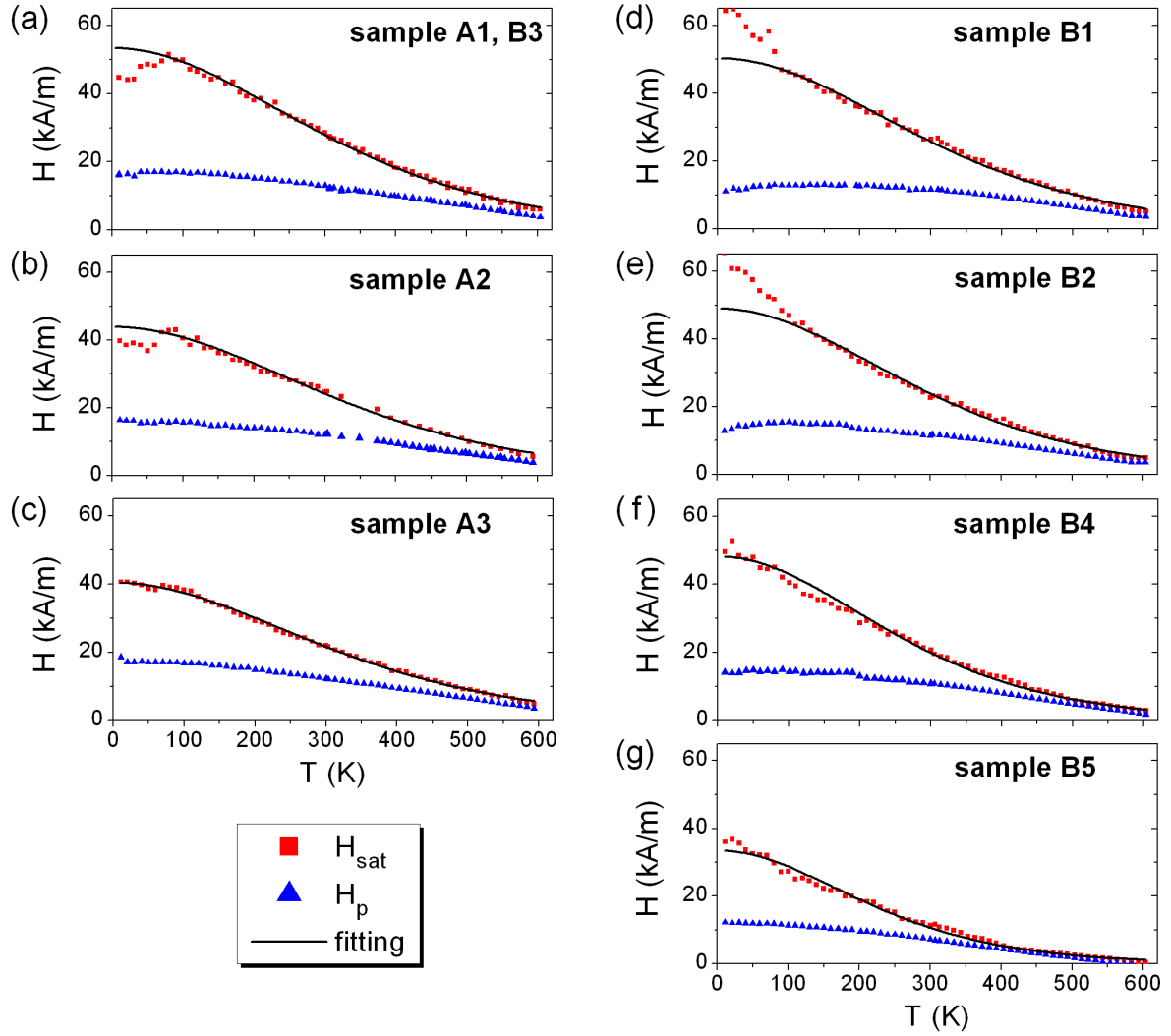
Fig. 3.9: *Saturation and plateau field with varying temperature for (a)-(c) samples of series A and (d)-(g) series B, respectively. The lines are fits of the $(T/T_0)/(\sinh(T/T_0))$ dependence to the experimental data. The extracted values of the zero temperature saturation field, H_0, and the characteristic temperature, T_0, are listed in table 3.2.*

obtained by MOKE are shown in Fig. 3.8. Similar loops of all samples have been obtained and at RT, they show identically behavior as has been found by AGM measurements. The significant differences between the MOKE measurements for $|H| < H_p$ is attributed to the different setups for the two temperature ranges. The setups create different phase shifts between the Kerr signal coming from the two ferromagnetic layers [112]. However, these phase shifts only affect the detected Kerr rotation, but does not influence the measurement of H_{sat} and H_p, as can also be concluded from the seamless transition of H_{sat} and H_p around RT, as presented in figure 3.9. Here, the behavior of $H_{sat}(T)$ and $H_p(T)$ is shown for all samples.

It is observed, that both, H_{sat} and H_p, decrease with increasing temperature. The saturation field data have been fitted with the $(T/T_0)/(\sinh(T/T_0))$ behavior as described by equation 1.2.1. Most of the samples show a high agreement between the fitted loop and the experimental data, but some show a deviation from the expected behavior for $T < 100K$. Since the model only takes into account the temperature dependence of the spacer layer contribution to the coupling, these deviations may be caused by additional contributions from the interfaces and magnetic layers [157]. As the reason for the deviation is not clear, these data have not been taken into account for the fittings. From these fittings one can obtain values of the zero temperature saturation field, $H_{sat,0}$, and the characteristic temperature, T_0. All values obtained from the fittings are listed in table 3.2.

Since the Ru spacer thickness and the coupling has been held constant for the samples in series A, T_0 and, accordingly, v_F are constant. For the samples in series A, the extracted values for T_0 are approximately 145K. This leads to a Fermi velocity of $v_F \approx 1.15 \times 10^7 \text{cm/s}$, which is in accordance with the values obtained in Co/Ru/Co multilayers [68].

Secondly, it is observed from the M(H,T) measurements, that H_{sat} has a stronger dependence on the temperature than H_P in the samples under study. Therefore, the quotient H_{sat}/H_p decreases as a function of T for almost all samples (see figures 3.9). Finally, the separation of plateau and saturation field, which is necessary for the spin-flop writing of MRAM bits, decreases for elevated temperatures. Although, samples B4 and B5 show a vanishing plateau field at elevated temperatures, causing an increase of H_{sat}/H_p for $T > 510K$ and T> 425K, respectively. In terms of the magnetic phase diagram calculated for AFi structures by WORLEDGE in Ref. [99] (see also figure 1.17), all samples approach the phase boundary between the spin-flop and the metamagnetic phase (defined by the condition $H_{sat} = H_p$) with increasing temperature.

To investigate the origin of this behavior, additional magnetization loops of the AFi system have been simulated using the model mentioned in section 3.1.1. The resulting $M(H)$ behavior, for one branch of the magnetization loops, is shown in dependence of the AF coupling strength and the uniaxial anisotropy constant in figures 3.10(a) and (c), respectively. The quotient H_{sat}/H_p has been evaluated from these loops and is shown in figure 3.10(c) and (d). It is evident that the margin between spin-flop and saturation field can be increased, if either the AF coupling is increased or the intrinsic anisotropy of the AFi is decreased.

From the quantum well model of coupling it is predicted that the exchange coupling oscillates in sign with a period of π/k_F, and the amplitude of the oscillation decays as $1/t_{NM}^2$, where $k_F = \frac{\hbar v_F}{m_e}$ is the Fermi wave vector in the spacer layer [69]. In Fig. 3.11(a), the coupling strength, J^{AGM}, and zero temperature saturation field, $H_{sat,0}$, in dependence of the Ru thickness are presented. Both show the expected oscillating behavior around the 2nd AF coupling maximum. In Fig. 3.11(b), the evaluated dependence of v_F on the Ru spacer thickness is shown, and a maximum of Fermi velocity around the second AF coupling maximum (at $t_{Ru} = 0.95$nm) is found.
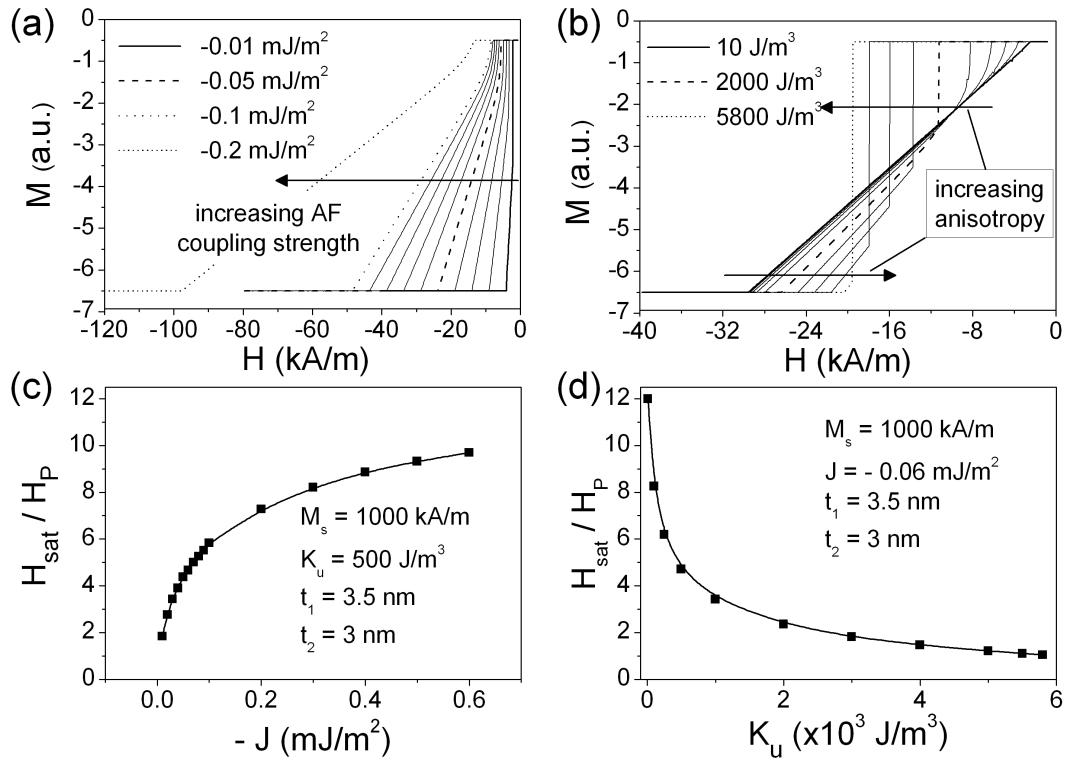
Fig. 3.10: *Calculated magnetization loops in dependence on (a) the coupling strength, J, and (b) the uniaxial anisotropy, K_u. The energy model of the AFi described in section 1.2.1 was used. Values of H_{sat}/H_p have been extracted from the M(H) loops for (c) varying J_{af} and (d) K_u. The simulation parameters used are noted.*
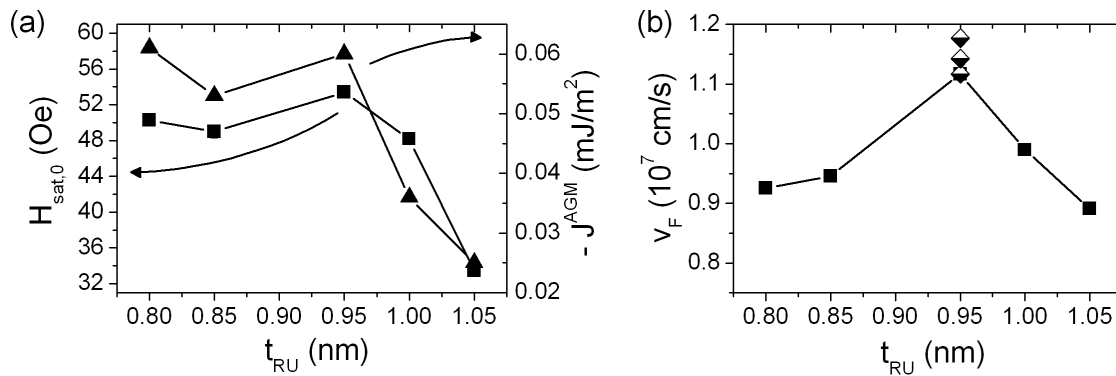

Fig. 3.11: *(a) Dependence of room temperature coupling strength (J^{AGM}) obtained from AGM measurements and zero temperature saturation field ($H_{sat,0}$) in dependence of the Ru spacer thickness. Both show the expected oscillating behavior around the 2nd AF coupling maximum. (b) Evaluated Fermi velocities in dependence on the Ru spacer thickness. The three data points at $t_{Ru} = 0.95$ are from the samples of series A, showing an almost constant Fermi velocity irrespective of the net moment.*

In conclusion, the temperature dependence of the saturation field and, therefore, the coupling strength for CoFeB/Ru/CoFeB trilayers has been investigated in this section. From these studies, we evaluated the characteristic temperature to be $\sim 145\text{K}$ and a Fermi velocity of $1.15 \times 10^7\text{cm/s}$; this is in good accordance with the results of Co/Ru/Co trilayers presented by others. The AFis based on amorphous CoFeB show a high anisotropy with a low distribution of the anisotropy direction around the easy axis of the system. While the narrow distribution is essential for application of these AFis as a soft magnetic electrode in MTJs, the absolute value of the anisotropy has to be decreased. As a consequence, this would increase the margin between the plateau and saturation field, necessary for spin-flop switching and especially important for operation at elevated temperatures or in heat assisted writing schemes.

3.2 Structural investigations on CoFeB

From the annealing studies on series A (in section 3.1.4), it is indicated that the onset of crystallization for the CoFeB is at around $T_{\text{ann}} \approx 350°\text{C}$ and strongly affects the magnetic properties of these systems. Since one of the advantages of the chosen CoFeB composition is its amorphicity and, therefore, its low coercivity, further microstructural investigations on the phase transition are of interest. It was the purpose of the studies in this section to directly investigate the structural character of CoFeB thin films.
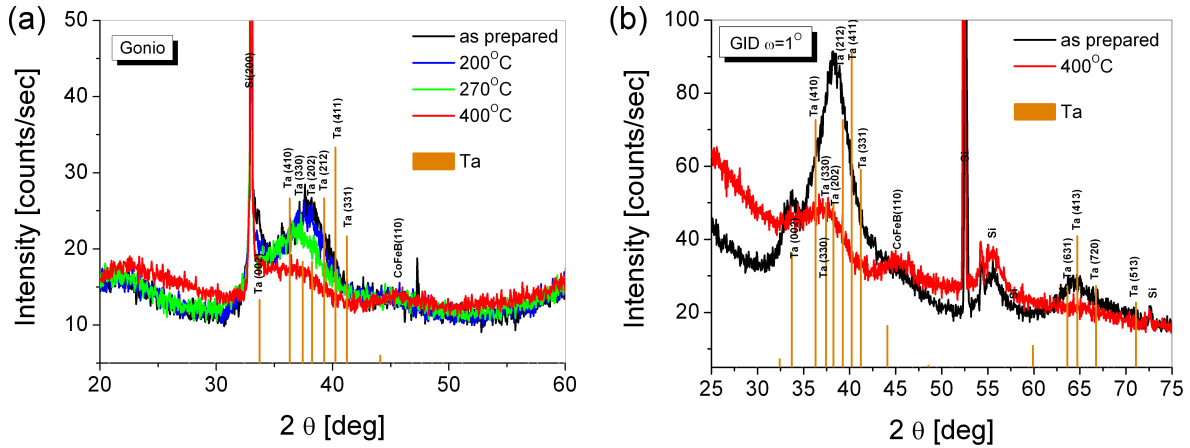

Fig. 3.12: *(a) $\theta - 2\theta$ and (b) Grazing incident X-Ray Diffraction (GID) scan of Ta(5)/Al1.2(oxid.)/CoFeB(20)/Ta(10) after annealing treatments of the sample.*

3.2.1 XRD measurements

For X-Ray diffraction measurements (XRD), samples of Ta(5)/Al(1.2, oxid.)/CoFeB(20)/Ta(10) have been sputter deposited on a Si/SiO$_2$ wafer. Because of signal/noise issues, the CoFeB layer has been chosen to be much thicker than in the investigated systems so far. To have the same growth conditions as in the previously investigated samples, the same seed layers have been used. Different pieces of the wafer have been thermally treated at temperatures between

200°C to 400°C and have been analyzed by XRD. [2]

The $\theta - 2\theta$ scans of the samples are shown in figure 3.12(a). The CoFeB shows no clear peak, indicating that there is no preferred texture of the CoFeB layer. This only changes slightly at $T_{\text{ann}} = 400°C$, where a broad distribution around 45° appears. These results are also reflected in the grazing incident X-ray diffraction (GID) scans of the samples shown in figure 3.12(b). In conclusion, there are no indications from XRD measurements of a strong texture in the CoFeB layer, thus confirming the assumption of an amorphous phase in our CoFeB thin film systems. Only at elevated temperatures is a texture, may be this is favorably initiated at the interfaces.

The second piece of information that can be extracted from the XRD measurements is that the Ta signal of the samples is distributed over different textures. The signal most likely originates from the capping Ta layer, since the bottom Ta layer usually grows amorphous and provides a broad background signal [158]. The decrease in Ta peak intensity with increasing annealing temperature is most likely caused by an oxidation of the capping layer.

The small angle diffraction scans after the annealing procedure are presented in figure 3.13. They show a regular oscillation of the signal with a low decrease in oscillation amplitude with angle, indicating smooth interfaces in the multilayer stack.
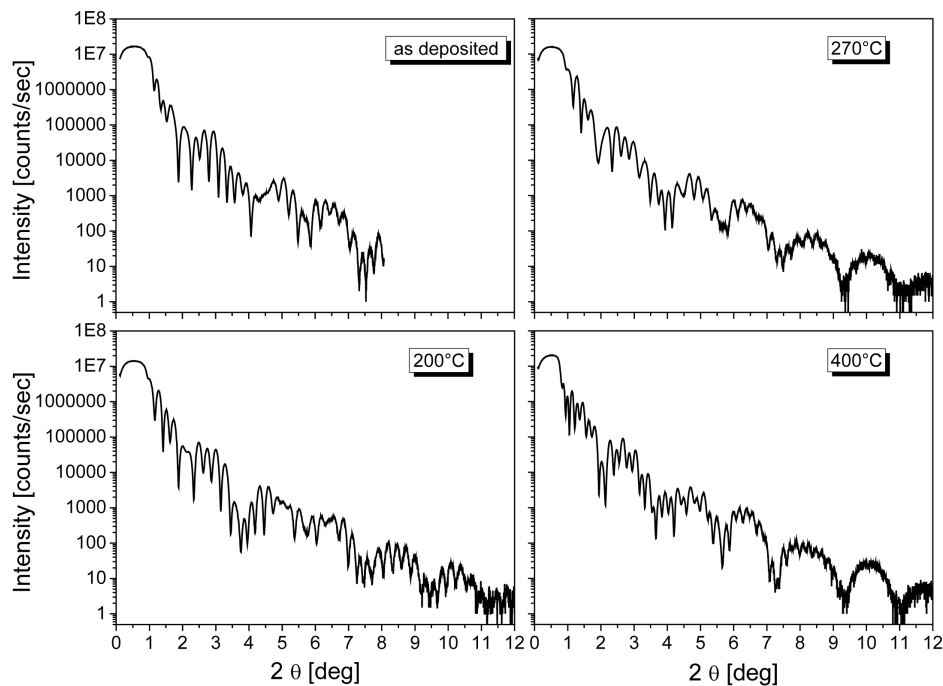

Fig. 3.13: *Small angle diffraction scan of Ta(5)/Al1.2(oxid.)/CoFeB(20)/Ta(10) after annealing process at different temperatures.*

3.2.2 HR-TEM images

The microstructural properties of a MTJ consisting of IrMn(8)/CoFe(3)/Ru(0.8)/CoFe(2.8)/Al(1.2, oxid.)/CoFeb(4) have been investigated by high resolution transmission electron microscopy (HR-TEM).[3] The transport properties of the same tunnel junction will be discussed in comparison to other MTJ stack systems in the next paragraph. The resulting HR-TEM images are shown in figure 3.14 and have also been published in a comparative study of various amorphous Co based alloys in Ref. [159].

It is observed that both the top electrode and the Al_2O_3 barrier reveal a typically noncrystalline microstructure without long range ordering. To prove this, an electron diffraction pattern of the CoFeB soft electrode has been acquired.
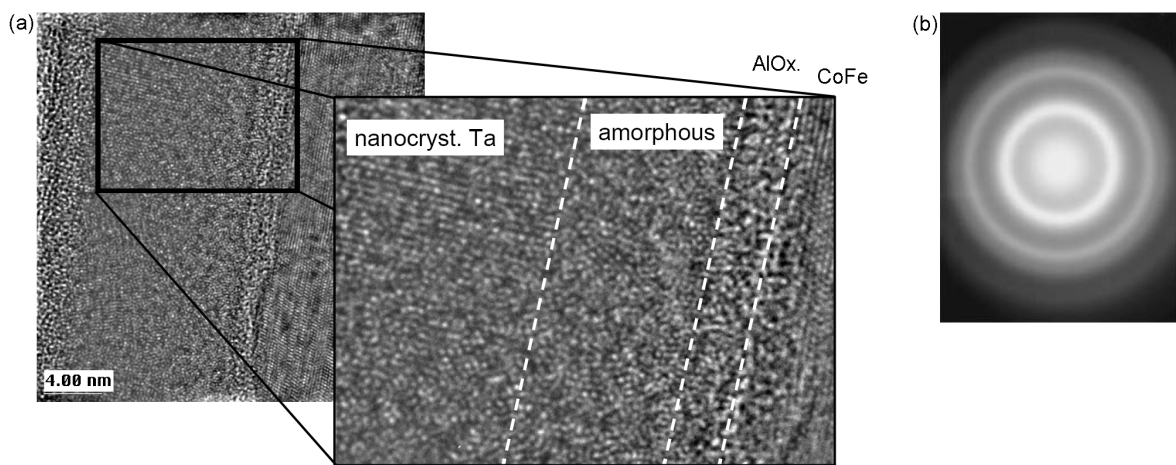

Fig. 3.14: *(a) Cross section HR-TEM images for MTJ 1 with CoFeB as the soft magnetic electrode, showing a typical noncrystalline microstructure in the barrier and the upper electrode layers, and thus a matched common interface. (b) Electron diffraction rings obtained from the relevant upper electrode layer (courtesy of M. Seibt and Y. Luo, University of Göttingen, Germany)*

As described in section 2.2.5, it is hard to distinguish between amorphous and (sub)nanocrystalline material in diffraction mode. As shown in figure 3.14(b), the diffraction image of the CoFeB film under study shows diffuse rings around the central spot [4]. Therefore, this result most likely indicates a disordered atomic arrangement but with short-range order for the CoFeB soft electrode (see Ref. [159] for detailed analysis).

On the other hand, the CoFe at the bottom magnetic electrode shows a polycrystalline lattice structure, suggesting that the interface with the barrier layer is structurally incoherent. At a few positions, the interfaces become more or less undulated, which evidently arises from orientation-dependent growth of the polycrystalline layers, but they remain rather correlated.

The larger magnetoresistive tunnel effect observed within the CoFeB based MTJs in comparison to tunnel junctions with polycrystalline electrodes, can be partly attributed to the

---

[3]HR-TEM images have been made by M. Seibt, IV. Physikalisches Institut, and Y. Luo, I. Physikalisches Institut, Universität Göttingen, Germany

[4]A similar effect of line broadening can also happen in polycrystalline samples by overexposure or wrong development of the photographic film. To my knowledge, this possibility has been ruled out during the experiments.

microstructural match across the amorphous Al_2O_3/CoFeB interface. The spin-independent scattering and spin transfer of the tunneling electrons may be diminished, compared with incoherent interfaces [159, 160]. It is worth mentioning that amorphous CoFeB interfacing the AlO_x barrier on both sides should, therefore, give a further increase of TMR ratio, as it has been already shown by other groups [26].
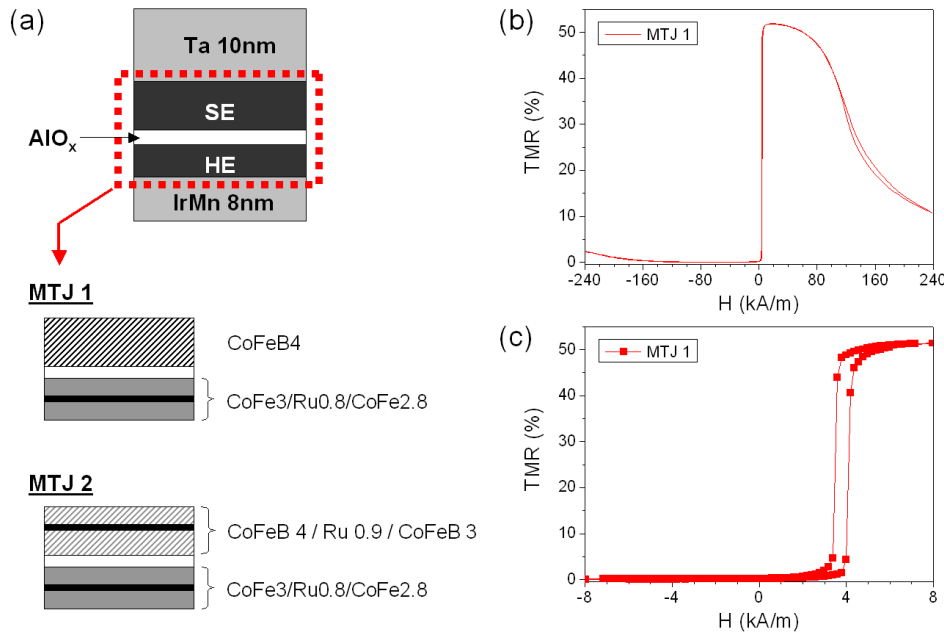
3.3 Transport properties

Fig. 3.15: *(a) Schematics of the investigated MTJ stack systems. (b)/(c) Transport measurements of "MTJ 1" at room temperature showing a TMR ratio of $\sim 50\%$.*

3.3.1 MTJ with CoFeB/Ru/CoFeB based soft electrode

To prove the concept of an artificial ferrimagnet as a soft magnetic electrode in magnetic tunnel junctions (MTJ), we have integrated an amorphous CoFeB-AFi in a complete MTJ stack system. To compare the results to a commonly used stacking with a single layer soft electrode, two similar systems have been prepared (see figure 3.15(a)):

- *MTJ 1 (CoFeB single layer as soft electrode):*
  IrMn(8)/CoFe(3)/Ru(0.8)/CoFe(2.8)/Al(1.2,oxid.)/CoFeb(4)

- *MTJ 2 (CoFeB-AFi as soft electrode):*
  IrMn(8)/CoFe(3)/Ru(0.8)/CoFe(2.8)/Al(1.2, oxid.)/CoFeB(4)/Ru(0.9)/CoFeB(3)

Both system have been deposited on an appropriate seed layer and have been protected from oxidation by a Ta capping layer. After deposition the exchange bias was set with a field anneal at 270°C. The conventional stack system (MTJ 1) shows a high TMR ratio of $\sim 50\%$
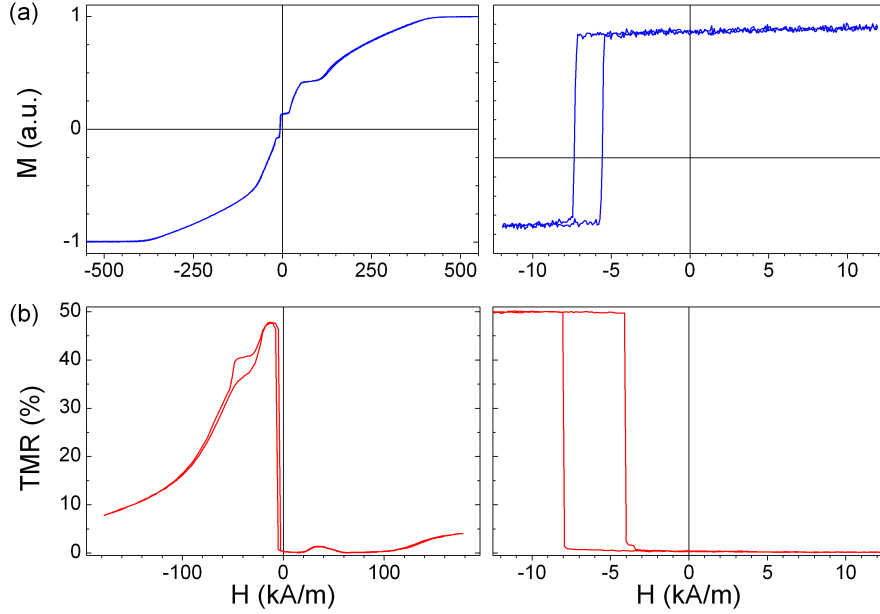
Fig. 3.16: *(a) Major and minor magnetization loops and (b) transport measurements of "MTJ 2" with CoFeB-AFi as soft electrode.*

at room temperature (see figure 3.15(b)/(c)), thus indicating a high spin polarization of the ferromagnetic electrodes.

Figure 3.16(a) shows the major and minor magnetization loops as obtained from MTJ 2. The soft magnetic AFi sense layer has a coercivity of $H_c = 1$ kA/m that is comparable to the same AFi investigated in section 3.1.3, indicating that the additional underlayers only weakly influence the coercivity. A well defined plateau field ($H_p \approx 17$ kA/m) and a saturation field of $H_{sat} = 36$ kA/m is observed for the top AFi. From these values, the coupling energy can be obtained, which is comparable with the corresponding AFi of series A. The high Néel-coupling of $H_N = 6.4$ kA/m most likely results from the roughness induced by the buffer layer which has not been optimized. The magnetoresistive measurement (figure 3.16 (b)) shows the same TMR amplitude of $\sim 51\%$ as MTJ 1 with the CoFeB single layer as soft electrode. A rectangular switching of the soft electrode AFi has been achieved at $H_c = 1.9$ kA/m. The increase in coercivity is probably caused by domain-wall pinning at the boundary edges of the element [161], since SEM images show very high edge roughness of the measured elements with $12.5 \times 12.5 \ \mu m^2$.

3.3.2 Improvements of TMR with amorphous CoFeB electrodes

Since these early investigations of CoFeB based MTJs, further improvements have been made at our lab utilizing amorphous CoFeB as soft magnetic electrodes in combination with an AlO_x barrier. A transport measurement of such an optimized stack system is shown in figure 3.17. The highest TMR ratio that has been obtained was $\sim 65\%$ in good accordance to the highest reported TMR values in literature for comparable material systems [26]. This optimized stack consists of an almost compensated exchange biased CoFe-AFi as the hard magnetic electrode and a single layer of CoFeB as the soft electrode. The key factor for these improvements has

been the systematic study of the oxidation conditions (see Refs. [152, 160]). As a result, it turns out that the oxidation times have to be slightly shorter than in MTJs with polycrystalline materials interfacing the barrier. Concluding from the coinciding MR results obtained from MTJ 1 and MTJ 2 in section 3.3.1, the same improvement of TMR ratio in an optimized stack system with a CoFeB based AFi as a soft magnetic electrode is expected.
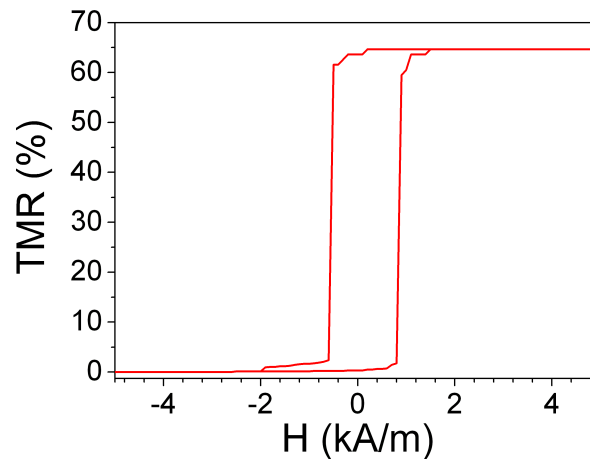

Fig. 3.17: *Transport measurement of an improved MTJ stack with CoFe-AFi hard electrode and CoFeB soft electrode.*

Furthermore, a comparative study of polycrystalline and amorphous electrodes in a magnetic tunnel junction depending on the annealing temperature has been carried out. The results of these studies have been discussed in detail in a recent publication [152]. It turns out that the thermal stability of the TMR increases for stack systems employing the amorphous alloy. Most interestingly, more than 20% of TMR is achieved after annealing at 400°C for the case of two CoFeB electrodes interfacing the barrier. This larger thermal stability is mostly attributed to the microstructural quality of the AlO_x/CoFeB interfaces, as pointed out in section 3.2.2. However, the drawback of integrating the CoFeB alloy into these systems is a drastic and unfavorable increase of the resistance area (RA) product of the MTJ.

3.4 Sub-micrometer sized CoFeB/Ru/CoFeB elements

It was one purpose of this study to investigate the switching behavior of the amorphous CoFeB-AFi in sub-micrometer size elements, where shape anisotropy and the magnetostatic edge coupling have also to be taken into account. These contributions lead to an *effective anisotropy* for patterned elements which is different from the anisotropy of continuous films. Until now, results combining sub-micrometer size elements of coupled amorphous AFi systems are rarely published. To our knowledge, only electrical measurements of MTJs consisting of an amorphous AFi soft electrode are presented in Ref. [162]. Therefore, the results presented in the following paragraph have been recently published by us (see Ref. [163]).

3.4.1 Micromagnetic simulation

So far, a macroscopic energy model has been used to discuss the properties of unpatterned AFi systems with respect to various dependencies (e.g., see sections 1.2.1 and 3.1). For micrometer and sub-micrometer scale elements, this model is not longer appropriate, as already discussed in section 1.5. Therefore, the micromagnetic code of Scheinfein has been used for the simulation of these patterns.

parameter	value
cellsize	5nm
saturation moment	$M_s = 860$ emu/cm^3
exchange coupling	$A_{i,j} = 1.05 \times 10^{-6}$ erg/cm
uniaxial anisotropy	$K_u = 2.4 \times 10^3$ erg/cm^3
bilinear coupling	$J_{AF} = -4 \times 10^{-9}$ erg/cm
biquadratic coupling	$J_{BQ} = 0$ erg/cm

Tab. 3.3: *Parameters used for micromagnetic simulation, unless otherwise noted in the text.*

Unless otherwise noted, the material properties listed in table 3.3 have been used for the following simulations. All parameters have been chosen in accordance with experimental results obtained from CoFeB based trilayer systems. No edge roughness, in addition to the deviation from the ideal shape caused by the discretization, has been considered. A fully saturated orientation of both layers with negative saturation was chosen as an initial state. For all field steps during the simulation, a small bias field of $H_y = 0.04$kA/m has been applied in order to break the symmetry of the system and achieve a better agreement between the simulation and the experimental data. It was previously investigated that this bias field is in a range not to alter the behavior other than breaking the symmetry.

Figures 3.18 and 3.19 show the domain patterns of sub-micrometer sized CoFeB(4)/Ru(1)/CoFeB(3) trilayers for various applied magnetic fields at the switching and spin-flop range. The lateral sizes of the simulated elements have been set to 250nm×500nm and 250nm×1500nm, respectively. For the small aspect ratio element, the switching apparently takes place by rotation of the spins. In the larger aspect ratio element a 360° domain wall configuration is found as an intermediate state during the reversal process. Nevertheless, this configuration is not to be considered as a stable state, and the switching takes place in a comparably small field window as in the smaller elements.

In the spin-flop range, defined by $H_p < H < H_{sat}$, the thinner layer has to turn into the direction of the applied field. This process is driven by a larger Zeeman energy in comparison to the interlayer exchange energy. For the small element, a so called "c-state" is formed; this is more pronounced in the thin layer than in the thick one because, in the thin layer, the magneto static energy is smaller. For the larger aspect ratio element, it is energetically more favorable to turn the magnetization via a multidomain state.

Furthermore, it is observed that the coercivity increases with increasing aspect ratio by approximately 1.3kA/m. The saturation field, however, decreases with increasing aspect ratio. Both properties will be discussed within the experimental results in the following sections.

Fig. 3.18: *Finite element simulation of CoFeB(4)/Ru(1)/CoFeB(3) trilayer with a dimension of 250nm×500nm. The domain patterns of the two layers are plotted for various external magnetic fields at the switching and spin-flop range. The color wheel indicates the angles of the individual spins.*
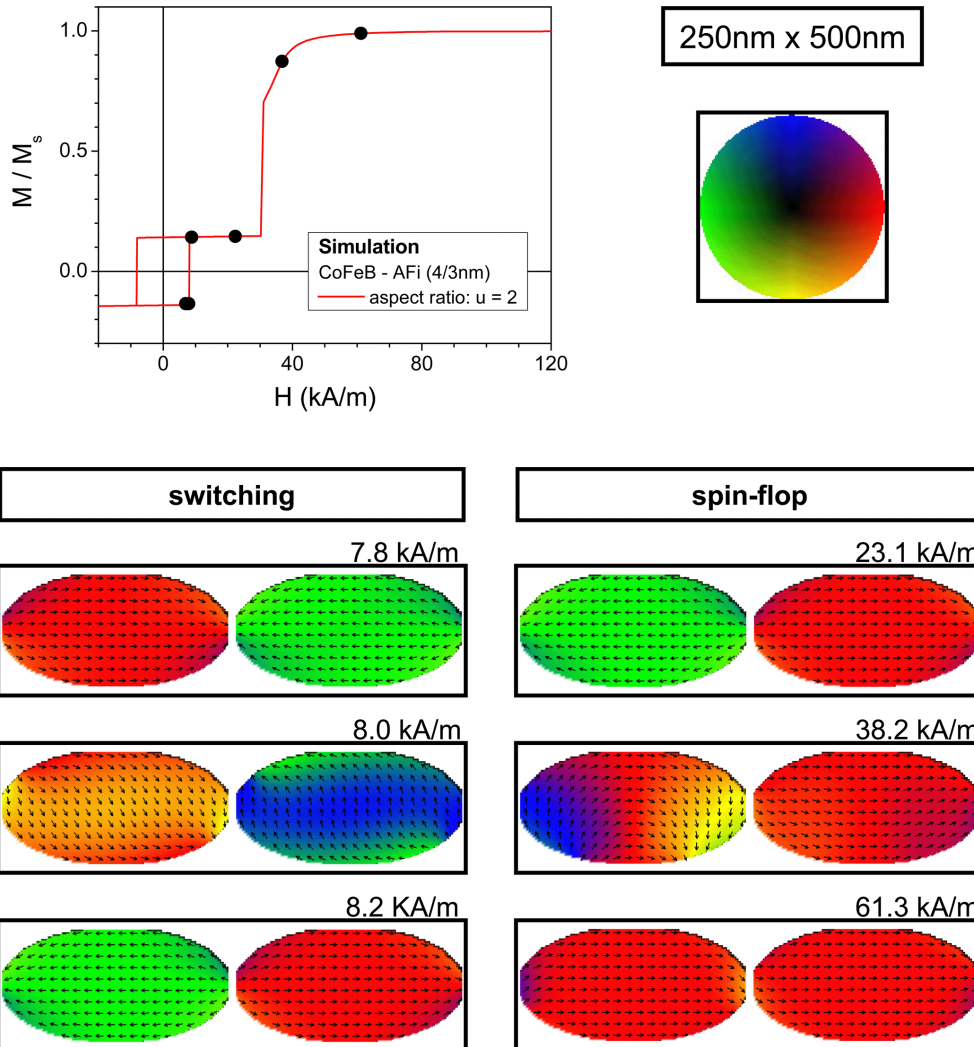
Fig. 3.19: *Finite element simulation of CoFeB(4)/Ru(1)/CoFeB(3) trilayer with a dimension of 250nm×1500nm. The domain patterns of the two layers are plotted for various external magnetic fields at the switching and spin-flop range. The color wheel indicates the angles of the individual spins.*
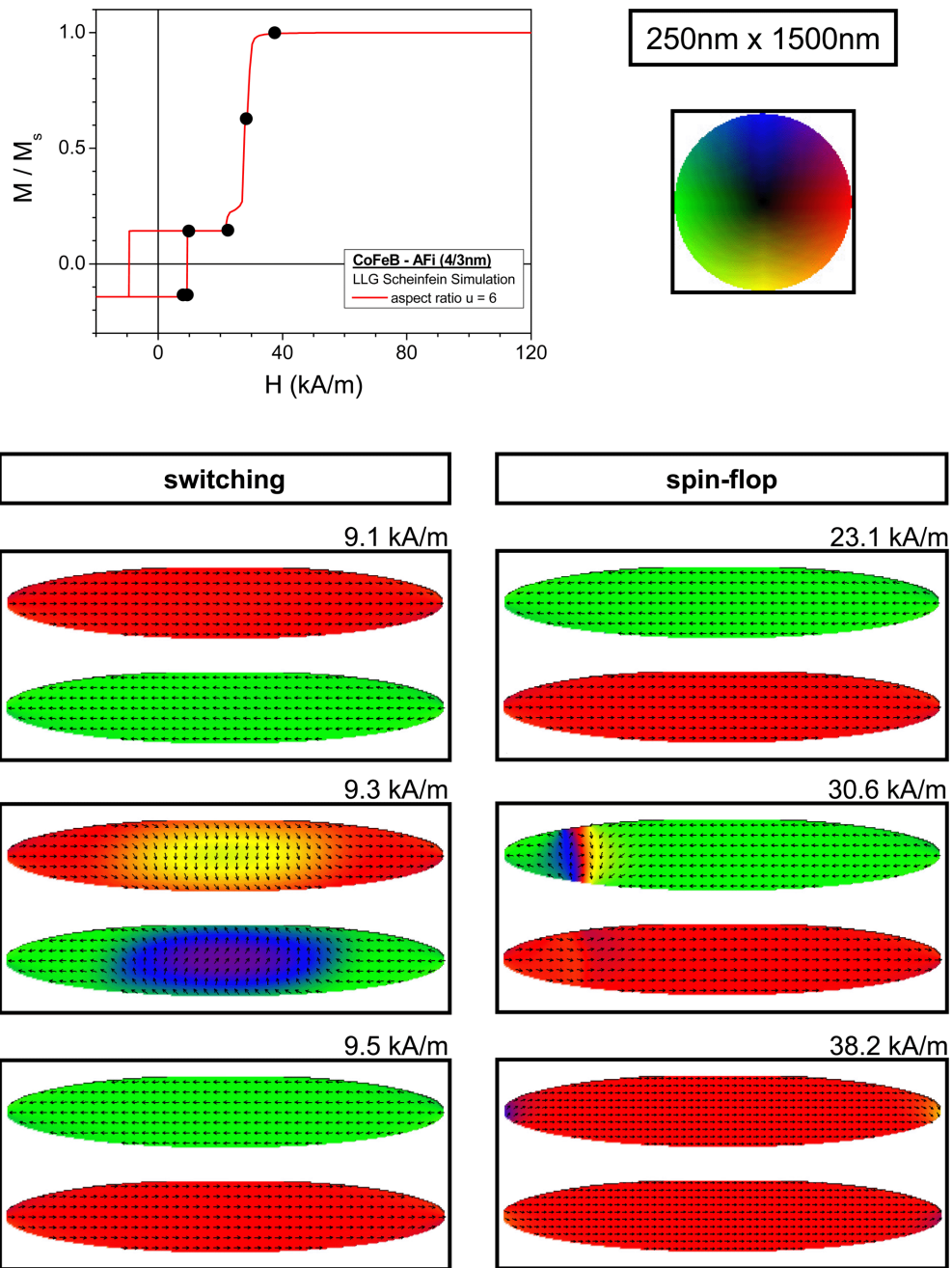
3.4.2 Experimental results and discussion

In this section, the experimental results on the sub-micrometer scale AFi patterns are presented in dependence on various parameters (e.g., aspect ratio, net moment and coupling strength). The results are also compared to micromagnetic simulations, that have been performed for the CoFeB based AFis.

The sub-micrometer sized patterns have been prepared by electron beam lithography as described in section 2.1.2. After patterning all samples have been field annealed for 20min. at 150°C and 475kA/m applied parallel to the long axis of the ellipses using a vacuum annealing furnace to strengthen the easy axis of the elements with respect to the geometry. Magnetization loops of all arrays have been recorded by our NanoMOKE2 ^{TM} setup with a typical laser spot diameter of 4μm.

sample	system	Q_{meas}	H_{sat} $\left[\frac{\text{kA}}{\text{m}}\right]$	J $\left[\frac{\text{mJ}}{\text{m}^2}\right]$
A	CoFeB(3.5) / Ru(0.95) / CoFeB(3)	7.7	29.8	-0.06
B	CoFeB(4.0) / Ru(0.95) / CoFeB(3)	5.1	26.3	-0.06
C	CoFeB(4.5) / Ru(0.95) / CoFeB(3)	3.7	23.9	-0.06
D	CoFeB(4)			

Tab. 3.4: *Investigated samples and parameters extracted from the AGM measurements of the unpatterned layer systems.*

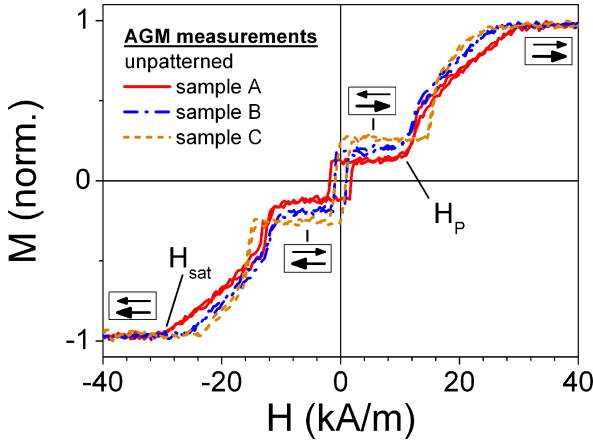### Dependence of saturation field on aspect ratio

Fig. 3.20: *Magnetization loops of unpatterned samples taken by AGM, showing a well established coupling for all AFi samples. The saturation field, H_{sat}, and the plateau field, H_p, are indicated for sample A.*

Room temperature magnetization curves, $M(H)$, of the unpatterned AF coupled sandwiches are shown in figure 3.20. From the $M(H)$ loops, obtained by AGM, one can evaluate the coupling to -0.06mJ/m^2 for all investigated AFi samples. The values are in accordance to the oscillatory coupling dependence on the Ru spacer thickness around the second antiferromagnetic maximum as presented before. All data extracted from the AGM measurements are given in table 3.4.

As an example, in figure 3.21 we show representative magnetization loops of patterned arrays of all AFi samples as obtained by MOKE measurements. All elements shown have a constant width of approximately 250nm to 270nm. The length of the elements has been varied, resulting in the aspect ratios given in the figure. The strong AF coupling is maintained after the patterning and annealing steps. Additionally, the saturation field increases with decreasing aspect ratio (i.e. length or size) of the ellipses, due to
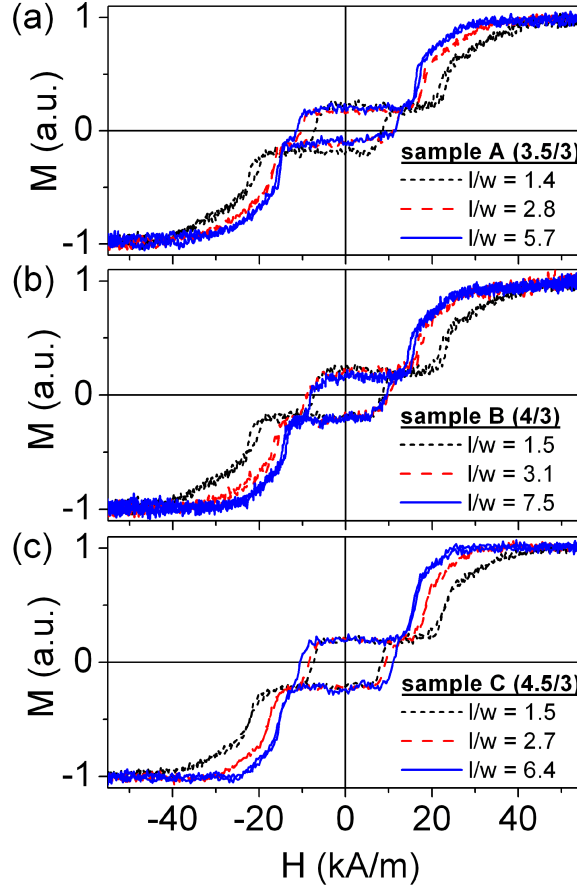
Fig. 3.21: *Major magnetization loops of some of the patterned arrays measured by MOKE, showing a well established coupling and $H_p > H_c$ for all samples. The width of approximately 250 to 270nm was kept constant for all investigated samples.*

an increase in stray field coupling between the layers within the AFi system. For large aspect ratios, H_{sat} achieves the values of the unpatterned samples.

As derived in section 1.4, the saturation field can be expressed by the contributions of antiferromagnetic and strayfield coupling. We have also seen that the strayfield contribution only depends on the x-component of the demagnetization factor, n_{x}, since the y-components in case of an AF coupled system are compensated for external magnetic fields larger than the plateau field ($H > H_{\text{p}}$).

The experimental data has been fitted with the n_{x} behavior as shown in figure 3.22(a). The fitting shows a good accordance between the experimental data and the model, thus verifying the dependence of the saturation field on n_{x} for small aspect ratios. From the fitting parameters, one can further extract the saturation field for an infinitely elongated ellipse to 28.6 kA/m for sample A, 24.2 kA/m for sample B and 22.8 kA/m for sample C, respectively. These values are in agreement with the measured saturation fields of the unpatterned AFi samples which are directly related to the interlayer coupling (see Tab. 3.4). Furthermore, micromagnetic simulations of AFi elements of comparable size confirm this behavior, as presented in figure 3.23(a).

Dependence of coercivity on aspect ratio

For $H < H_{\mathrm{p}}$, the AF coupling remains stable. As can be seen from figure 3.21, the AFi reverses its magnetization like a single ferromagnetic layer with a reduced net moment and enhanced effective anisotropy. Therefore, it is possible to measure minor magnetization loops in a small field window (± 10 to ± 15 kA/m, depending on H_{p} of the sample) and extract the coercivity, H_{c}, of the arrays (see figure 3.22(b)).
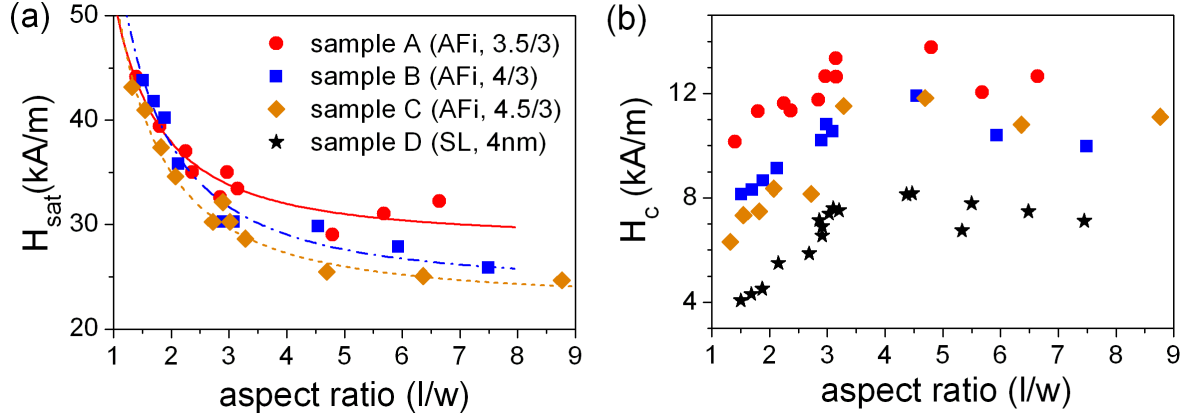

Fig. 3.22: *(a) Saturation field, H_{sat}, and (b) coercivity, H_c, of patterned samples versus the aspect ratio $u = \ell/w$. The width of approximately 250 to 270nm was kept constant for all investigated samples. The dashed lines in (a) represent a fit with a function proportional to the demagnetization factor n_x.*

For small aspect ratio ($u < 4$), H_{c} increases with u by approximately 3.5 kA/m and remains constant for larger aspect ratios (see figure 3.22(b)). Due to a tendency towards overexposure for the large aspect ratios during lithography, the slight decrease in coercivity for these patterns is most likely attributed to the slightly larger width of the ellipses. The same behavior of the coercivity versus aspect ratio holds also for the single layer sample. The increase of H_{c} for small aspect ratios is caused by the increase in shape anisotropy, which for an ellipse is $H_{\mathrm{k}} = 4\pi M_{\mathrm{s}} \frac{t_{\mathrm{net}}}{w}(n_{\mathrm{y}} - n_{\mathrm{x}})$ as derived in equation 1.19. Only the demagnetization factor $(n_{\mathrm{y}} - n_{\mathrm{x}})$ depends on the aspect ratio for the patterned samples with constant width. Therefore, the experimental results of figure 3.22(b) are in qualitative accordance with the $(n_{\mathrm{y}} - n_{\mathrm{x}})$ dependence on aspect ratio (see figure 1.16). Deviations from the calculated dependence for large aspect ratios are likely due to micromagnetic differences: small elements are stabilized by a non vanishing stray field, arising from the magnetic poles of the elements. These stray fields stabilize the overall magnetization of the elements so that the reversal can be more accurately approximated by a single domain mechanism. For large aspect ratios, the magnetic poles are better separated, thus minimizing the stray field coupling and, as a result, a nucleation driven magnetization reversal, most likely initiated by edge domains, is more favorable, leading to an almost constant coercivity [161].

Figure 3.23(a) shows the dependence of coercivity versus aspect ratio, $u = \ell/w$, together with saturation field versus u, as evaluated from micromagnetic simulations for comparable AFi elements. The discussed behavior is reproduced with qualitative accordance in the simulations. Nevertheless, in comparison to the fittings within the model, the coercive field depends more
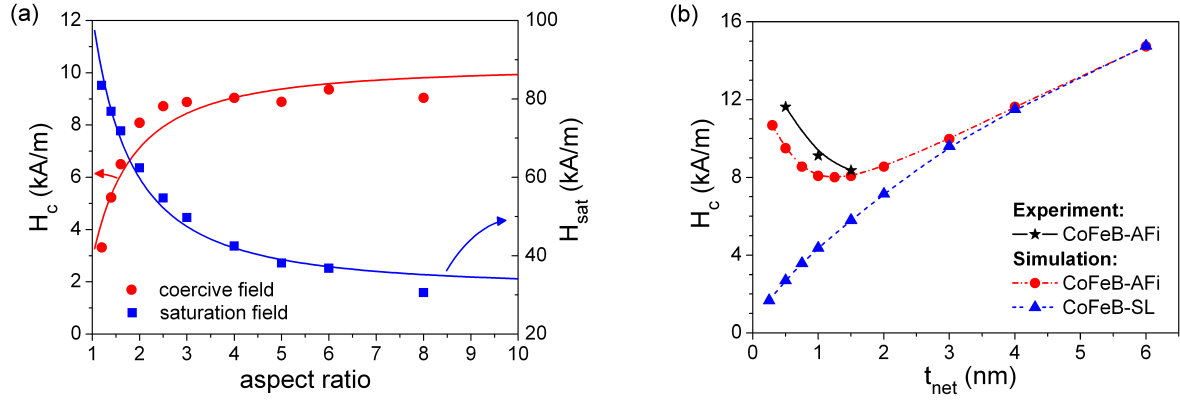
Fig. 3.23: *(a) Simulated dependence of H_c and H_{sat} on the aspect ratio for elements of CoFeB(4)/Ru(1)/CoFeB(3). The width of the elliptical shaped elements was held constant at $w = 250nm$ and the length was varied between $\ell = 300$ to $2000nm$. The lines are fittings in accordance with the assumed model, with a $n_y - n_x$ and n_x behavior, respectively. (b) Experimental and calculated dependence of coercivity, H_c, on the net thickness, t_{net}, of the AFi and a single layer, respectively. The experimental data points are for elliptical shaped elements with the dimension of $250nm \times 520nm$, the simulated data are evaluated for the same sample geometry.*

strongly on the length for small aspect ratios. This may originate from the deficient treatment of the micromagnetic variations at the edges of the elements, thus contributing strongly to the results in smaller structure sizes.

Unlike elliptic elements with a single ferromagnetic layer, the coercivity of the patterned AFi samples does not scale proportionally to the net magnetic moment. With higher net moment, the coercivity is *decreasing*, but always remains larger than for elements of a 4nm thick single layer. The reason is a superposition of the effective anisotropy due to the AF coupling ($\sim m_{tot}/m_{net}$), as expressed by equation 1.6 for the unpatterned films, and the dependence of coercivity on the net magnetic moment as described by equation 1.19 ($\sim m_{net}(n_y - n_x)/w$). Overall, the influence of the AF coupling is dominating for the investigated CoFeB-AFis and the coercivity is increased by approximately a factor of 1.4 when decreasing the net thickness of the AFi, and therefore the net moment, from 1.5 to 0.5nm.

The dependence of coercivity on the net thickness, $t_{net} = t_2 - t_1$, of the AFi and for single layer samples with layer thicknesses of $t = t_{net}$ have been simulated using the "LLG micromagnetic simulator" by Scheinfein (see figure 3.23(b)) [164]. For the simulation of the AFis, the thickness of the second FM layer, t_2, was varied between 3.5 and 6nm, whereas the thickness of the first FM layer was kept fixed at $t_1 = 3nm$, and the thickness of the non-magnetic spacer was chosen to be 1nm. The saturation moment of the FM layers was assumed to be $M_s = 860 emu/cm^3$, the uniaxial anisotropy to be $K_u = 2.4 \cdot 10^3 erg/cm^3$, the exchange stiffness constant to be $A = 1.05 \cdot 10^{-6} erg/cm$, and the AF coupling constant to be $J = -0.004 \cdot 10^{-6} erg/cm$ in accordance to experimental results on CoFeB. The coercivity of the simulated elliptic AFi elements of $250nm \times 520nm$ decreases with net thickness for $t_{net} \leq 1.5nm$, and increases for larger t_{net}, asymptotically reaching the values of the single layer coercivity. The experimental data of the AFi arrays with the same geometry show a similar behavior, therefore verifying
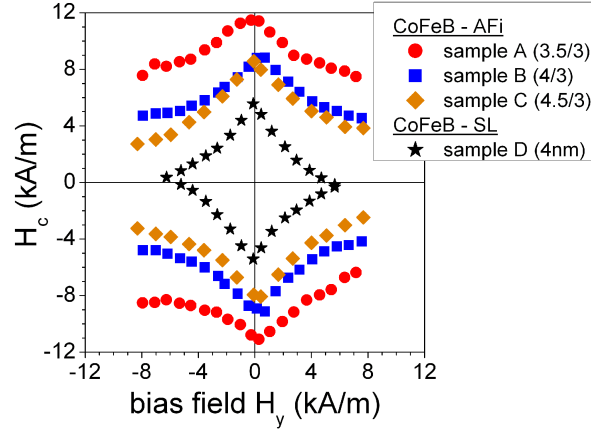
Fig. 3.24: *Bias field dependence of the coercivity for all investigated film systems with an aspect ratio $u = 2.2$, also illustrating the gain in effective anisotropy by introduction of the antiferromagnetic coupling and the strong influence of the increased Q-value on the anisotropy of the system.*

the described model for the samples under study.

Figure 3.24 shows the bias field dependence of the coercivity for samples patterned with an aspect ratio of $u = 2.2$. Due to the increase of effective anisotropy with the Q-value (and therefore basically with the inverse net magnetic moment), the asteroid gets stretched along the hard axis (bias) field. If used in a conventional writing scheme as a soft magnetic electrode for applications like MRAM or magnetic logic, the broad asteroid shape of the AFi storage layer cells limits the choice of Q-value due to field limitations, reducing the proposed advantages of an AFi structure reported by others [61, 62].

The AFi based on an amorphous CoFeB alloy shows a strong increase in the effective anisotropy due to the AF coupling, mediated by a thin Ru interlayer and by the stray field coupling. This is reflected by a higher coercivity and an increase of the asteroid width compared to a single CoFeB layer. The dependence of the switching field on the net magnetic moment cannot be explicitly explained within the model that considers the AFi as a rigid ferromagnetic layer with a reduced moment. One has to further take into account the increase in effective anisotropy, which basically scales with the inverse net moment for the investigated combinations of layer thicknesses. This last factor appears to be dominating in the system under study and leads to the decrease of coercivity with net moment. Finally, it has been found that the saturation field of the patterned AFis decreases decreasing with larger aspect ratio and is asymptotically reaching the saturation field of the unpatterned films. The origin for this behavior in small aspect ratios can be found in the additional contribution of the stray field coupling of the two ferromagnetic layers within the AFi, which basically depends on the demagnetization factor n_x versus aspect ratio.

Dependence of coercivity on coupling strength

The dependence of coercivity on the coupling strength for sub-micrometer sized AFi elements has been investigated by micromagnetic simulation. Therefore, the material parameters for CoFeB(4)/Ru(1)/CoFeB(3) and elliptical shaped elements with lateral dimensions of $250 \times$

1000nm have been chosen. The coupling was varied between $J_{lin} = 0$ to $-1 mJ/m^2$. Additionally, two single layers of CoFeB with identical geometry and thicknesses of 1 and 7nm have been simulated for comparison. The resulting coercivity of all simulations are presented in figure 3.25. For large coupling strength, the coercivity of the AFi system is approximately 16kA/m and decreases with decreasing AF coupling to less than 6kA/m, almost reaching the coercivity of a single layer element with the net thickness of 1nm. For very small AF coupling strength, $0 > J_{lin} > -0.007 mJ/m^2$, the AF configuration of the element cannot be achieved and the element behaves like a single layer of the total thickness $t = t_1 + t_2 = 7nm$ with $H_c \approx 21.5 kA/m$.

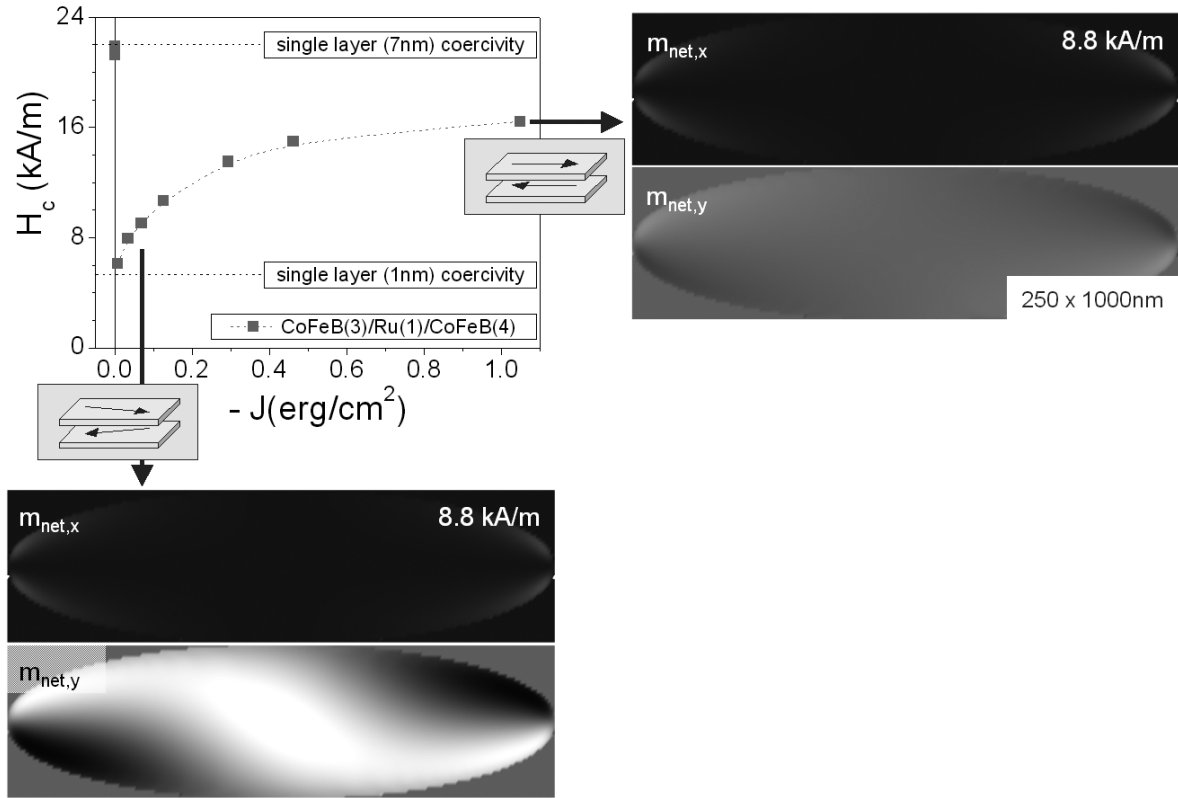
Fig. 3.25: *Coercivity versus coupling strength as extracted from micromagnetic simulation of $250 \times 1000nm$ ellipses of CoFeB(4)/Ru(1)/CoFeB(3). The domain patterns represent the x and y component of the magnetization for a strongly and weakly coupled AFi at an applied field of 8.8kA/m, respectively. The scaling is identical in both graphs.*

The origin of the strong dependence of coercivity on coupling strength is found in the domain patterns, also presented in figure 3.25. Here, the x and y components of the net moment of the AFi are shown for an applied field of 8.8kA/m for both a weakly coupled sample with $J_{lin} = -0.07 mJ/m^2$ and a strongly coupled sample with $J_{lin} = -1 mJ/m^2$, respectively. It is found, that the low AF coupled sample shows a much higher contrast in the y component of the magnetization. Therefore, the torque on the magnetization is higher for lower coupling strength, resulting in a smaller coercivity.

In comparison to these results, the unpatterned layer system shows a much stronger dependence of coercivity on the coupling strengths (see figure 3.7) and reaches the saturation
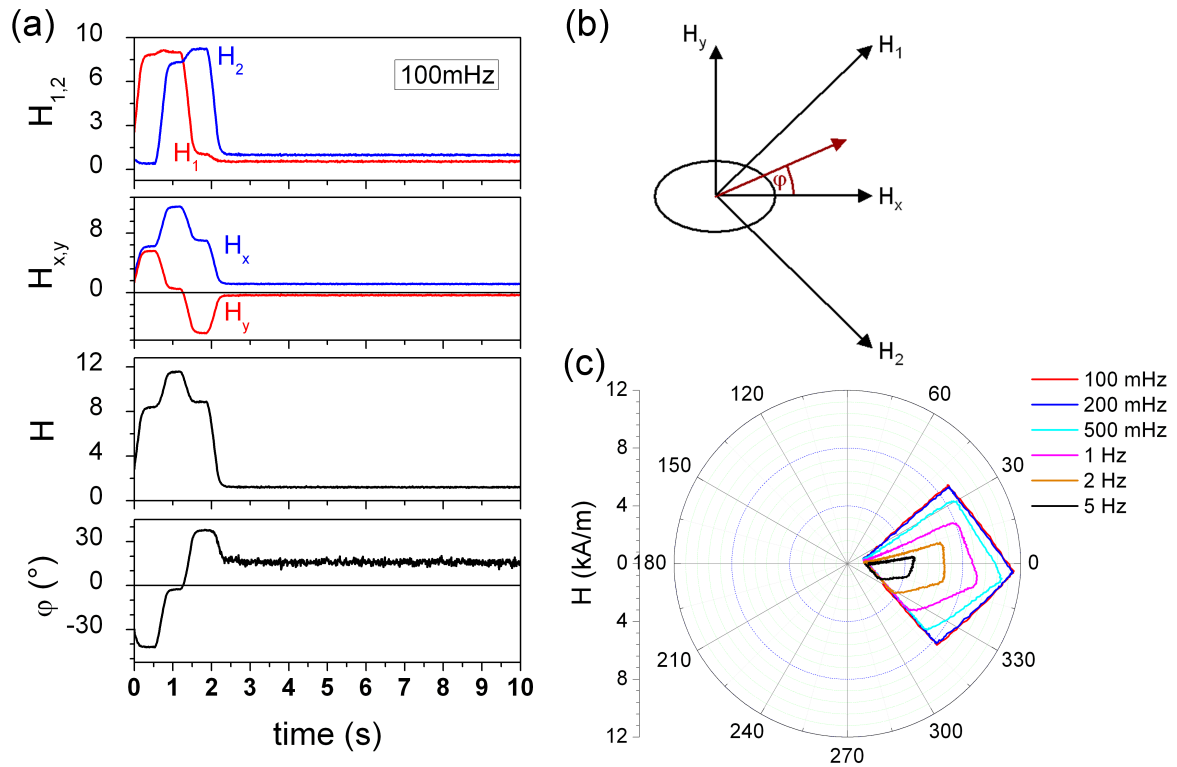
Fig. 3.26: *(a) Applied field sequence for the spin-flop switching scheme, (b) definition of fields and field angle with respect to the elements easy axis, and (c) polar plot of the boxed fields at different field sweeping frequencies.*

of coercivity much faster. The different behavior is most likely attributed to the additional contribution of shape anisotropy in patterned samples.

3.4.3 Spin-flop switching

In order to test the new spin-flop switching scheme on sub-micrometer sized samples by means of magneto-optical Kerr magnetometry, the NanoMOKE setup and the software had to be adapted. This approach promises a fast way to test the switching characteristics of patterned AFis, thus avoiding the complex patterning process of MRAM bits with field generating conductance lines and electrical contacts. As already discussed in section 1.4.1, two orthogonal fields have to be applied to the sample at $\pm45°$ with respect to the easy axis of the magnetic bits. Since the magnet system is installed in and perpendicular to the plane of incidence, two possibilities for the application of fields are possible:

- The sample has to be turned by $45°$ with respect to the x-axis. This results in a decrease in signal by approximately 30%. The signal difference between the two remanent states of the patterned AFi systems under study is of the order of $S_1 - S_2 = 0.1$mV, corresponding to approximately $2 \cdot 10^{-6}$rad of Kerr rotation. Since this value is at the resolution limit of the tool, it is not favorable to lose 30% of the signal by this field configuration.

- The applied fields ($H_{x,y}$) have to be turned by $45°$ to get the applied fields $H_{1,2}$ of the spin-flop switching scheme (see figure 3.26(b)). This can be achieved by a matrix rotation of the fields in the x-y-plane:

$$\begin{pmatrix} H_x \\ H_y \end{pmatrix} = \begin{pmatrix} \cos(\varphi) & \sin(\varphi) \\ \sin(\varphi) & -\cos(\varphi) \end{pmatrix} \cdot \begin{pmatrix} H_1 \\ H_2 \end{pmatrix}$$

$$\overset{\varphi=45°}{=} \begin{pmatrix} \sqrt{1/2} & \sqrt{1/2} \\ \sqrt{1/2)} & -\sqrt{1/2} \end{pmatrix} \cdot \begin{pmatrix} H_1 \\ H_2 \end{pmatrix}$$

The applied field sequence for the spin-flop switching scheme is shown for a sweep frequency of 100mHz in figure 3.26(a). The driving amplitude of the x and y electromagnets has been set to 1V, resulting in a spin-flop field amplitude of approximately 8.5kA/m. Higher amplitudes with up to 60kA/m are possible with the chosen magnet system. Due to the inductive load of the electromagnet, the field sweeping frequencies are limited to less than 200mHz. For higher frequencies, it is not possible to achieve the required boxed field with φ up to $\pm 45°$, as can be seen at the polar plot in figure 3.26(c).
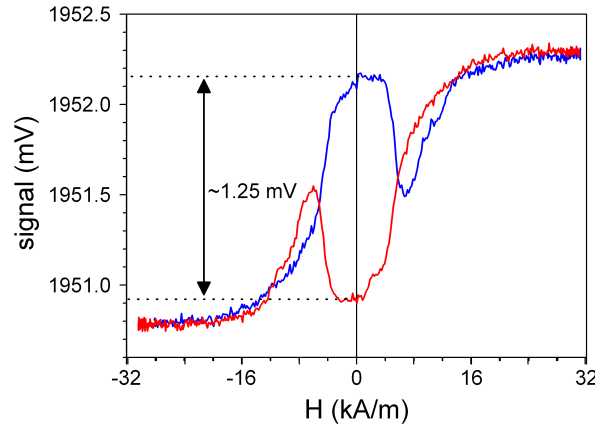

Fig. 3.27: *Longitudinal Kerr effect versus the applied magnetic field of the patterned sample used for the spin-flop experiments. The blue (red) line represents the sweep from negative (positive) to positive (negative) fields. The negative area under the loop for $-H_p < H < H_p$ results from different contributions of the two magnetic layers within the compensated AFi to the total detector signal, and does not reflect the "real" M(H) behavior.*

A first proof of the spin-flop switching in a magneto-optical experiment will be presented below. The patterns used for this measurement have been of circular shape with a diameter of 350nm. As a layer system, a compensated CoFeB-AAF has been used. The measured Kerr signal versus applied magnetic field of this sample is presented in figure 3.27. It shows two remanent levels with a high difference in the magneto-optical signal of $\Delta S = S_1 - S_2 \approx 1.25$mV. The negative area under the magnetization loop can be explained by the different magneto-optical signals coming from the two magnetic layers. Due to the high ΔS in comparison to the so far discussed patterned elements, this sample was a promising candidate for first spin-flop experiments with the NanoMOKE setup.

To test the effect of the applied spin-flop field cycle on the magnetic bits, the signal levels and, therefore, the orientation of the magnetization of the bits, have been recorded after each

field cycle. The sample was first saturated in a constant external field $H > H_{\text{sat}}$ to make sure, that all bits were aligned in one direction and the initial signal has been denoted S_0. After saturation, the toggle field cycle has been applied to the sample twice in a row and the signal states S_1 and S_2 have been recorded after each cycle. Ideally, if all bits are switching reliably, there is a signal change of $S_1 - S_0$ after the first cycle and $S_2 - S_0$ is zero, i.e. all bits are back at the initial state after toggling the sample twice in a row. Due to the low signal levels in the AFi structures with sub-micrometer sizes, this procedure was repeated several times to obtain a more reliable dataset.
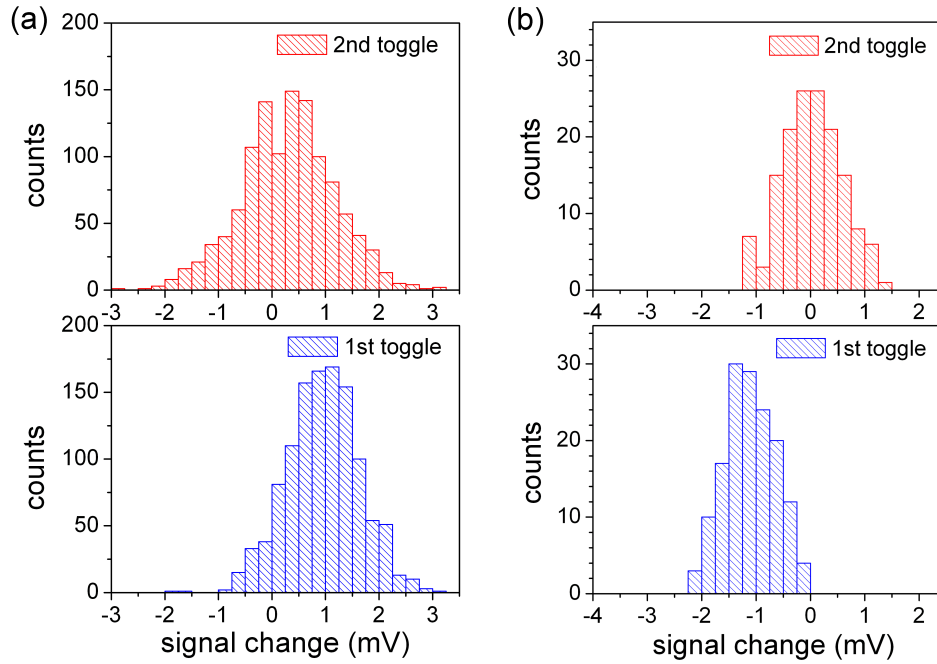

Fig. 3.28: *Signal changes, $S_1 - S_0$ (blue) and $S_2 - S_0$ (red), with respect to the initial state, S_0, after one and two spin-flop cycles, respectively. (a) Histograms obtained after saturation with $+28kA/m$ and (b) after saturation with $-28kA/m$.*

The results of these measurements are presented in figure 3.28. The two histograms per applied saturation field show the relative signal levels $S_1 - S_0$ (blue histogram) and $S_2 - S_0$ (red histogram) after the first and second spin-flop cycles, respectively. In the first row of experiments (figure 3.28(a)), a positive saturation field of $\sim 28\text{kA/m}$ has been applied, and the sample is magnetized at the lower signal level. After the first toggle sequence, the signal level is shifted to positive values and returns to the initial state after the second spin-flop cycle, as can be derived from the almost vanishing shift of the histogram. For figure 3.28(b) the saturation field was negative, therefore resulting in a signal shift to negative values after the first spin-flop cycle.

The shift of the maximum in the distribution is a clear indication for the spin-flop switching and is of the same order as the signal difference between the remanent states obtained from the majorloop presented in figure 3.27. Furthermore, it has been proven that this shift depends on the initial state. Nevertheless, the width $\sigma \approx 0.8$ of the distribution is broad in comparison to the signal change. This broad distribution has origins in the statistical noise level of

the experimental setup, which can be determined to be approximately 1mV for long time scales. Therefore, it is not possible to obtain important information about the switching field distribution from these MOKE measurements.

In conclusion, this is the first time the spin-flop switching scheme has been proven for an array of sub-micrometer magnetic bits by means of MOKE. For further experiments, the S/N level of the experimental setup has to be increased. If this goal can be achieved, this method could be valuable for rapid characterization of dense spin-flop MRAM arrays.

3.4.4 MFM on sub-micrometer scaled elements

Fig. 3.29: *MFM images and cross section of the patterned array on a patterned sample of a CoFeB single layer with 3nm thickness. The lateral size of the elements is approximately $320 \times 215nm^2$. The colored arrows indicate the direction of magnetization inside the elements.*

MFM images of sub-micrometer sized, magnetic elements of a single layer sample and of a CoFeB-AFi sample are presented within this section. The measurements have been performed at a HR-MFM at Swissprobe AG, Switzerland (see section 2.2.6 for detailed description of the measurement method and the setup of the MFM). All images have been taken at a remanent

state after demagnetizing the samples with alternating magnetic fields of decreasing amplitude.

The acquired images for a patterned single layer sample of CoFeB with 3nm thickness are shown in figures 3.29 and 3.30 for two different aspect ratios. Due to the known magnetization of the tip, the magnetic contrast can be correlated to a magnetic configuration in the interior of the elements as indicated by the arrows. The patterns imaged for figure 3.29 consist of elliptically shaped elements of 320×215nm. As can be deduced from the $4 \times 4\mu$m scan, the orientation of the magnetization inside the elements is always aligned along the easy axis of the system. The two different magnetic ground states are almost equally and randomly distributed over the array. This confirms the assumption in section 1.2.5 that the elements can be regarded as decoupled. Nevertheless, the magnetization vector seems to be distorted by a few degrees against the geometrical x and y-axes defined during the lithography process and this is reflected by the orientation of the whole array. This distortion is most likely related to some imperfections in definition of the shapes, caused by the beam blanking mechanism of the electron lithography system. This is confirmed by comparing the magnetization patterns with the SEM images of these arrays (not shown here).

Most interestingly, all elements show a pronounced dipolar contrast, even for these almost circular dots with a small aspect ratio of $u = 1.5$. This result can also be seen from the $0.75 \times 0.75\mu$m^2 scan and the cross section. This is most likely caused by the comparably high intrinsic anisotropy of the CoFeB alloy and has also been verified by micromagnetic simulations.

Similar results have been obtained for ellipses with the larger lateral size of approximately $0.31 \times 2.25\mu$m^2 ($u = 7.3$, see figure 3.30). For these elements, a magnetization reversal via a multidomain state is predicted by micromagnetic simulations. Due to the setup of the MFM, it is not possible to apply in-plane magnetic fields while imaging the magnetization configuration. From the results obtained in the remanent state, however, a stray field coupling as well as a multidomain state of the elements can be ruled out for zero applied fields.

The MFM imaging of the AF coupled patterns is much more difficult. Due to the partly compensated moment of the structures, the magnetic contrast is much lower. The images presented in figures 3.31 and 3.32 are taken from elements of CoFeB(4.5)/Ru(0.95)/CoFeB(3) with $u = 1.3$ and $u = 6.3$, respectively. As can be extracted from these images, a pronounced convolution of topological signal with a small additional magnetic contrast is observed. Nevertheless, all elements show a tiny dipolar contrast with the two poles at the ends of the ellipses. By also considering the increase of the effective anisotropy due to the AF coupling in comparison to single layer samples, one can draw the conclusion that these systems are in a single domain remanent state for all investigated aspect ratios. For more accurate images of the magnetization states, one would have to perform additional measurements with different magnetic orientation of the tip, as described in section 2.2.6.
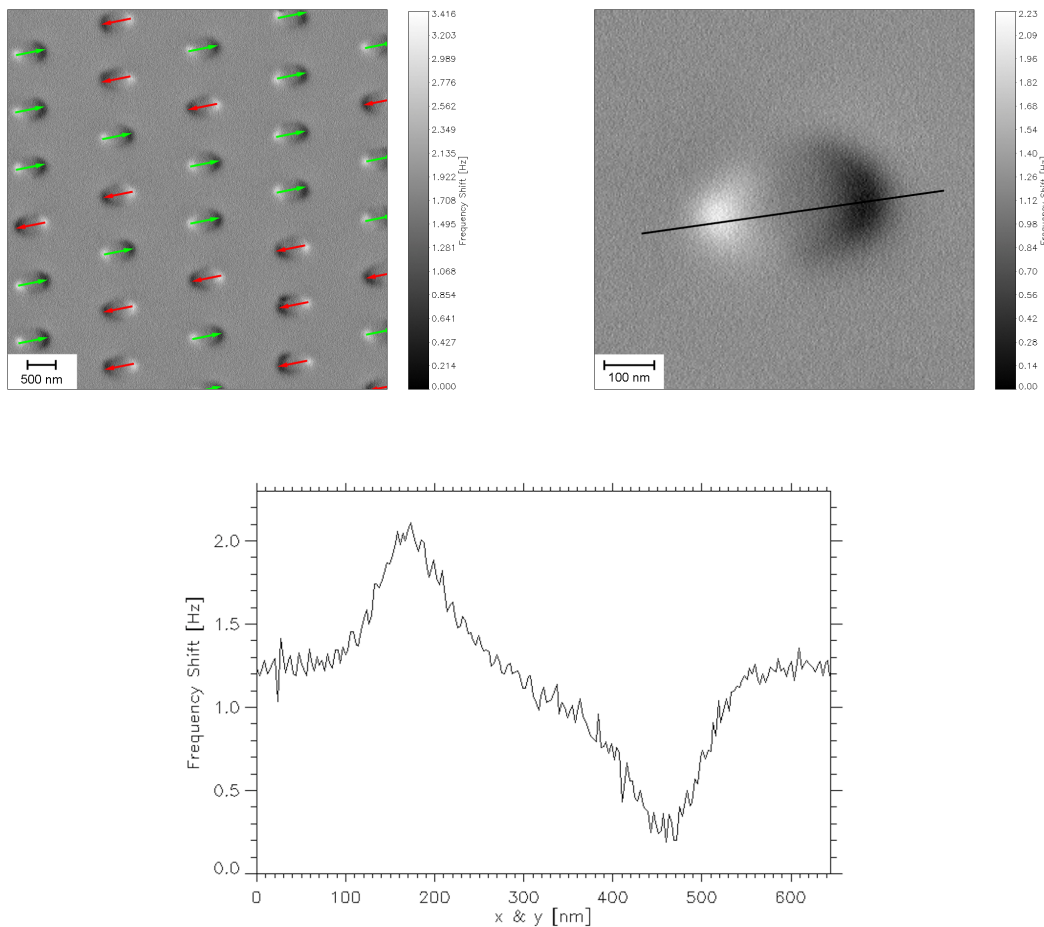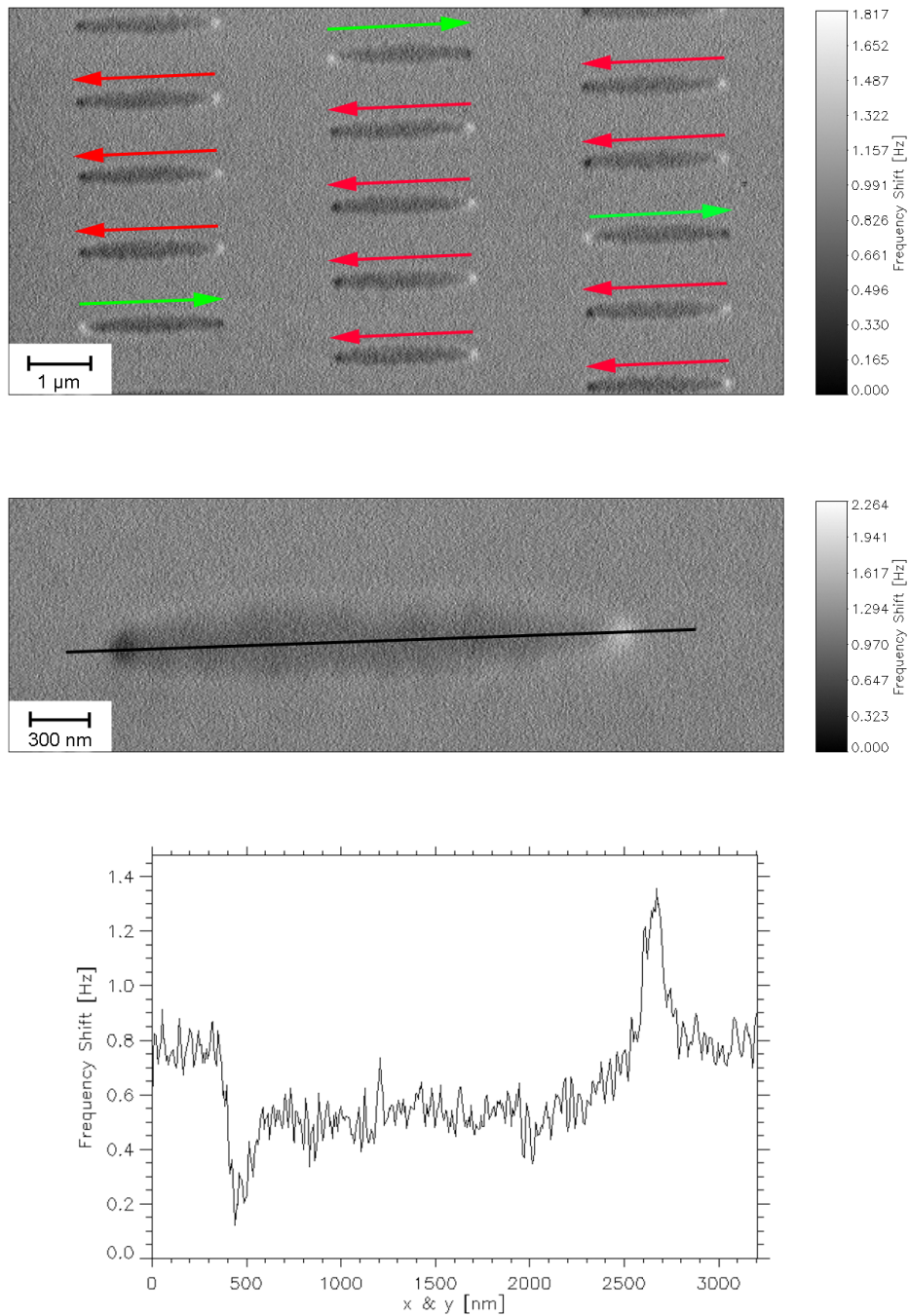
Fig. 3.30: *MFM images and cross section of the patterned array on a patterned sample of a CoFeB single layer with 3nm thickness. The lateral size of the elements is approximately $2.25 \times 0.31 \mu m^2$. The colored arrows indicate the direction of magnetization inside the elements.*

Fig. 3.31: *MFM images and cross section of the patterned array on sample C (CoFeB(4.5)/Ru(0.95)/CoFeB(3)) with the element size of $285 \times 215nm^2$. The colored arrows indicate the direction of magnetization inside the elements.*
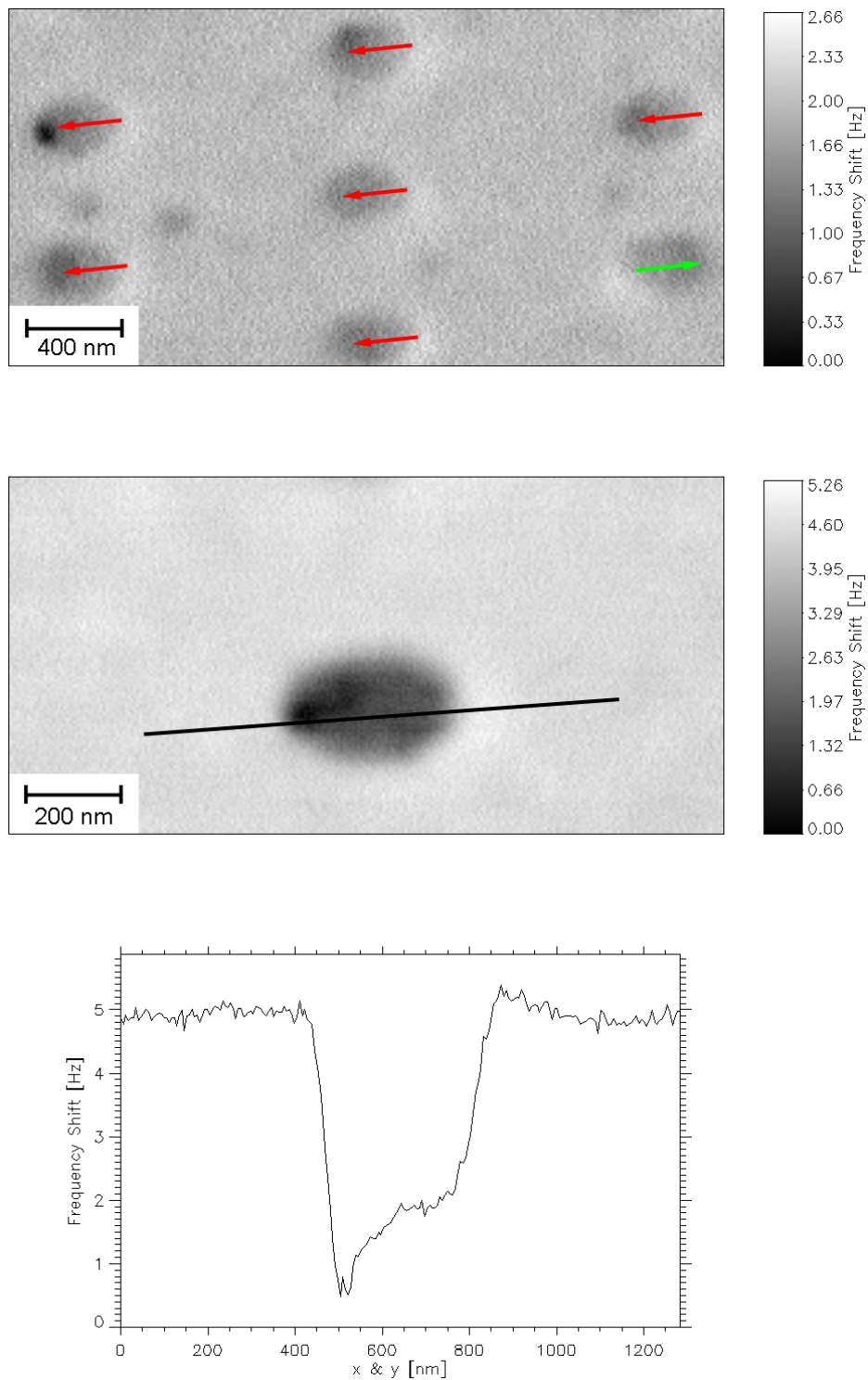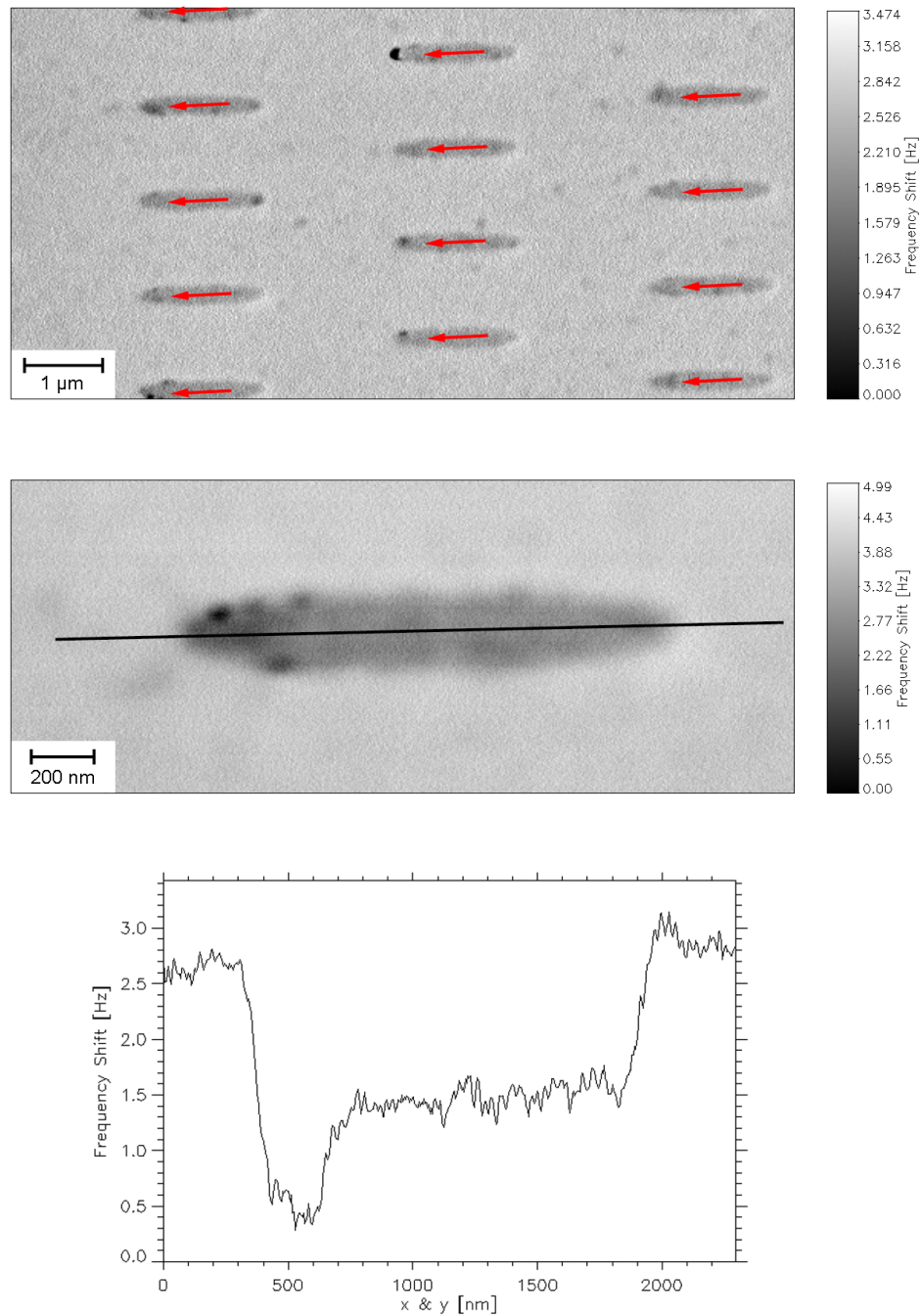
Fig. 3.32: *MFM images and cross section of the patterned array on sample C (CoFeB(4.5)/Ru(0.95)/CoFeB(3)) with the element size of $1.58 \times 0.25 \mu m^2$.*

3.5 Exchange bias

In section 3.3, the results obtained by integrating the amorphous CoFeB into magnetic tunnel junctions as a soft electrode have been discussed. By these promising results, and due to the reported benefits in interfacial matching, one may be inspired to use this material system as a hard electrode as well. Thus, the amorphous AlO_x tunneling barrier would be sandwiched between two amorphous CoFeB layers.

Therefore, the exchange bias properties of the CoFeB based hard electrodes in magnetic tunnel junctions is discussed in the following paragraphs. The first section covers the exchange bias properties of some systems containing amorphous CoFeB. Finally, the magnetic properties of sub-micrometer sized elements of exchange bias systems containing CoFeB are discussed.
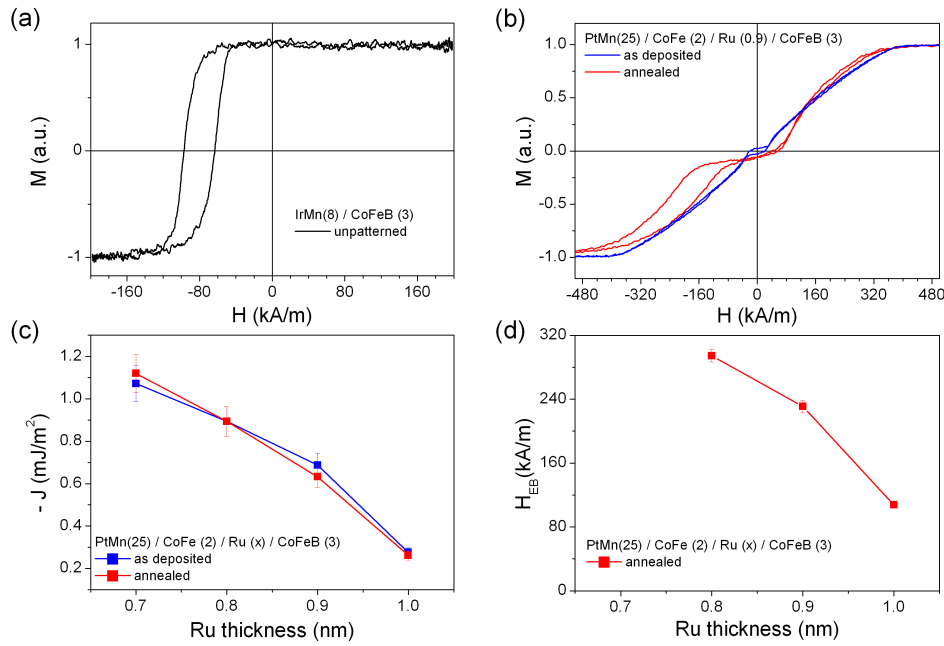
Fig. 3.33: *Magnetization loops of (a) IrMn(8)/CoFeB(3) and (b) PtMn(25)/CoFe(2)/Ru(0.9)/CoFeB(3), respectively. (c) AF coupling field, $-J$, and (d) exchange bias field, H_{EB} of PtMn(25)/CoFe(2)/Ru(x)/CoFeB(3). Numbers in parenthesis denote the layer thicknesses in nm.*

3.5.1 Suitability of CoFeB based AFis as a hard magnetic electrode

Figure 3.33(a) shows the magnetization loop of a CoFeB(3) single layer on IrMn(8nm), that serves as the antiferromagnet layer in this exchange bias system. After a heat treatment at 270°C for 15min. and a cooling down under application of a magnetic field of 400kA/m, a stable exchange bias of $H_{EB} = 80kA/m$ is established.

For integration as the hard magnetic layer in a MTJ stack, the magnetic moment of the reference layer has to be minimized in order to reduce the strayfield coupling between soft and hard electrode, as well as to decrease the Néel coupling. Therefore, a compensated AAF is usually chosen as the reference electrode. In order to study the feasibility of a compensated
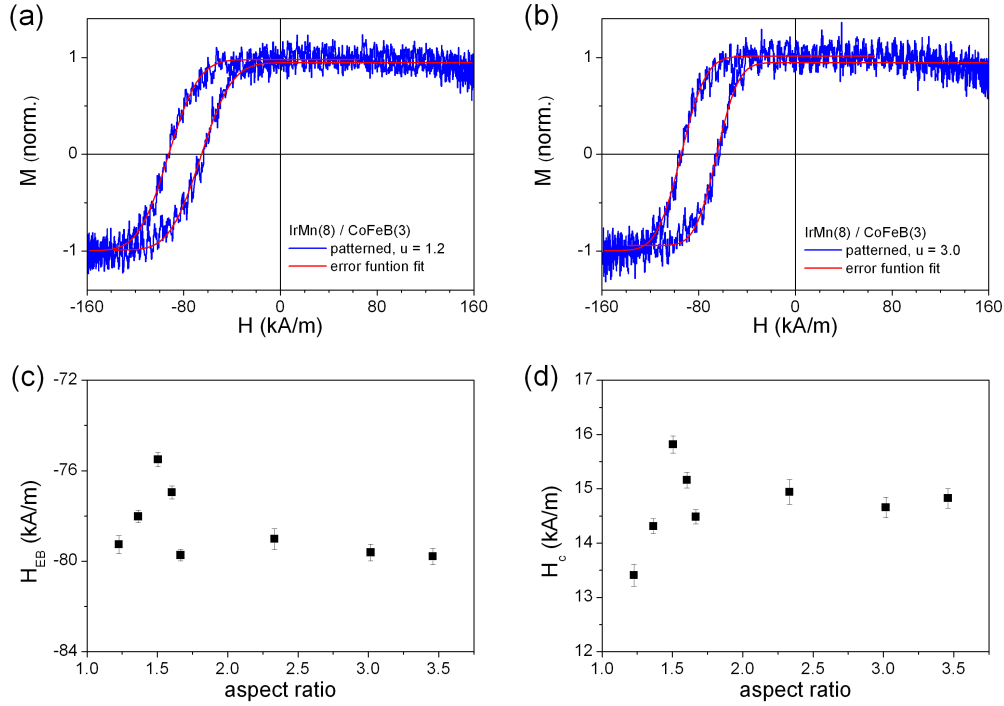
Fig. 3.34: *Magnetization loops of patterned IrMn(8)/CoFeB(3) of different aspect ratios (a)/(b). The red lines are fittings with a error function to determine exchange bias field and the coercivity presented in (c) and (d), respectively.*

CoFeB-AFi as a hard electrode, two series of AFM/CoFeB/Ru/CoFeB have been deposited. As the antiferromagnet, either IrMn or PtMn on appropriate buffer layers have been chosen. In both systems, either the interlayer exchange coupling could not be established, or the exchange bias (pinning) of the system was vanishing.

Therefore, a *mixed* AF coupled system with CoFe and CoFeB was used in order to achieve a high exchange biasing as well as a stable AF coupling. A series of PtMn(25)/CoFe(2)/Ru(x)/CoFeB(3) was deposited on an appropriate buffer layer. The thicknesses have been chosen so that the magnetic moments of the AFi are nominally compensated. After deposition, a heat treatment of 280°C for 100min. and a cooling down procedure with an applied magnetic field of 400kA/m has been performed. Figure 3.33(b) shows the magnetization loops of one of samples in the "as deposited" and annealed state. The resulting AF coupling strength $(-J)$ and exchange bias field (H_{EB}) extracted from these measurements are presented in figure 3.33(c) and (d), respectively. The coupling strength energy decreases with increasing spacer thickness from 1.1 to $0.27mJ/m^2$. The exchange bias shift, H_{EB}, decreases with increasing spacer thickness and decreases from 204 to 107kA/m.

In conclusion, a stable exchange bias system containing an amorphous CoFeB could be realized. To bring the CoFeB to the interface with AlO_x in a complete MTJ stack, either a single layer of CoFeB coupled on IrMn or a CoFe/Ru/CoFeB-AFi on PtMn can be used.

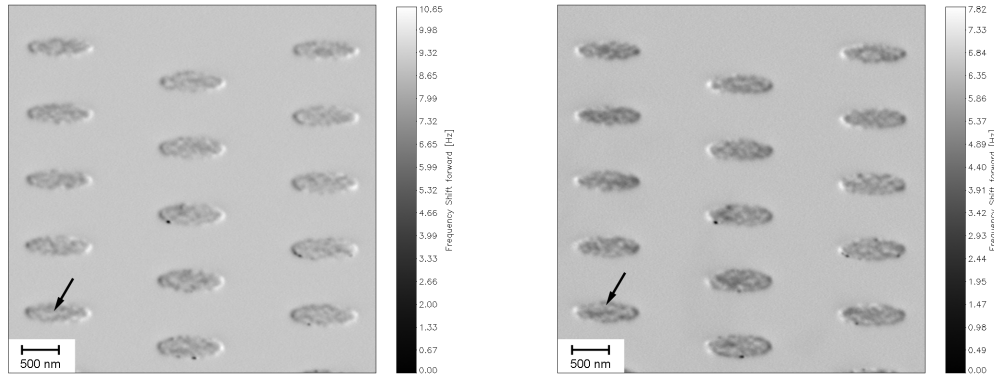Fig. 3.35: *MFM images of sub-micrometer sized IrMn(8)/CoFeB(3) with two different magnetic orientations of the MFM tip. The investigated element size was approximately $0.9 \times 0.3 \mu m$. As an example, the arrows mark a change in contrast in the interior of one element.*

3.5.2 Sub-micrometer scaled, CoFeB based hard electrodes

The investigation of exchange biased systems in sub-micrometer scales are of high interest, from a technological, as well as from a physical, point of view. It was the purpose of this study to increase enlighten several problems with exchange biased systems that arise when these systems are patterned to sub-micrometer scales. For example, D. Meyners reported unexpected fluctuations in the pinning direction of IrMn based tunnel junctions for sub-micrometer patterned ellipses in magnetologic wafers prepared by Siemens [165].

A film of IrMn(8)/CoFeB(3) deposited with appropriate seed and capping layers has been patterned to elliptically shaped elements with a width between 220 and 350nm and lengths between 265 to 1230nm, respectively. For comparison, a 3nm CoFeB single layer sample was patterned with similar structures.

The magnetization loops after heat treatment at 270°C for 15min. and a field cooling procedure with an applied field of 400kA/m are shown in figures 3.34(a)/(b). Comparing the results with the measurements of the unpatterned sample (see figure 3.33(a)), one cannot identify significant changes in either the exchange bias field or the coercivity with the sample size. H_{EB} is of the order of 76 to 80kA/m and H_{c} of the pinned layer is between 13.5 and 16kA/m. Angle dependent measurements of the coercivity have been performed in a range of $\pm 15°$ around the geometrical axis of the structures. All measurements show a maximum in coercivity at angles of $-3° \pm 1°$, indicating only a small deviation in the exchange bias direction. The offset from the geometric axis is most likely attributed to small misalignments of the patterned sample during annealing. From the magnetization behavior, there are no indications of instabilities caused by the exchange bias system in the range of sizes investigated here.

High resolution MFM images of the patterned elements have been recorded in collaboration with A. Drechsler and G. Tarrach of Swissprobe AG. In figure 3.35, the MFM images taken from an array of elements $0.9 \times 0.3 \mu m$ in size are presented. Between the two images, the magnetization direction of the tip was changed in order to separate the magnetic from the topological information in the scan. An explicit magnetic contrast is determined by comparing the images. Most interestingly, the magnetic dipolar contrast of the elements (comparable to
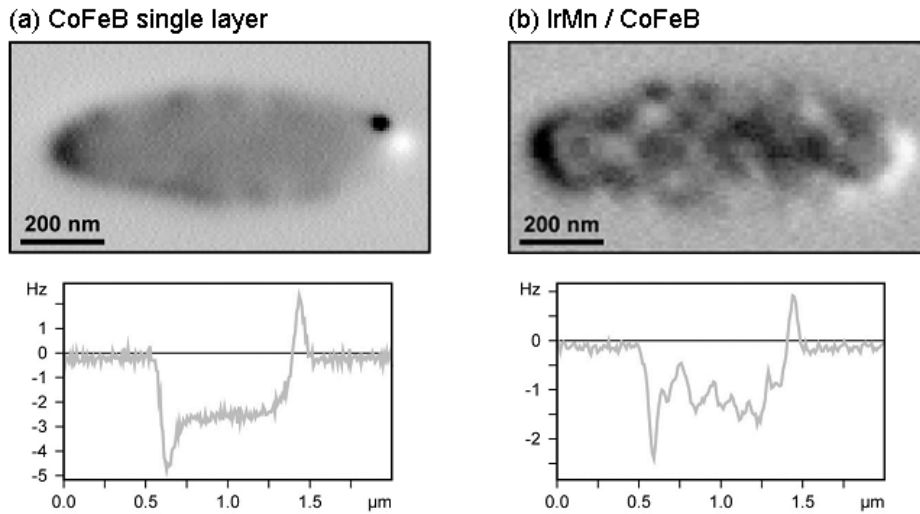
Fig. 3.36: *MFM images and cross sections of (a) a CoFeB(3) single layer and (b) a IrMn(8)/CoFeB(3). The investigated element size is approximately $0.3 \times 0.9 \mu m$ in both cases. Measurements and analysis by courtesy of A. Drechsler and G. Tarrach, Swissprobe AG.*

the contrast discussed for the single layer samples in section 3.4.4) is superimposed by a fine structure in the interior.

Figure 3.36 shows a close-up of a single element in comparison to an unpinned single layer of the same thickness. As already discussed, the cross section of the unpinned single layer clearly shows a magnetic dipolar contrast at both ends of the ellipse. In the interior of the element, the signal is dominated by the topology only. In the case of the exchange biased sample, however, a fine structure is clearly observed. This is caused either by topological features arising from a higher roughness of the elements or from magnetic effects caused by the exchange biasing. Comparing the two images with the changed tip magnetization in figure 3.35, one can further figure out several features inside the elements that turn their contrast from dark to light gray (or vice versa). One of these features is exemplarily marked by the arrows in figure 3.35. Both the non-existence of the fine structure in unpinned elements as well as the contrast reversal clearly suggests a magnetic origin for the fine structure.

Additionally, a non-contact AFM image of the same area as in figure 3.35 has been obtained with a non-magnetic cantilever. The scan is shown in figure 3.37. The topology of the elements is well defined with a flat surface on top of the elements. It is only observed at the edges that there are several spikes in the signal. These are most likely caused by resist residuals, underlined by a charging effect at the edges during SEM of these patterns. The height of the elements is of the same order as the thickness of the complete stack with seed and capping layers, thus indicating a good depth control during the etching process. Furthermore, these measurements confirm that the fine structure observed in the MFM images is not originated by roughness.

In order to distinguish between the magnetic and the topological interaction, the images of figure 3.35 have been digitally subtracted from each other. The resulting magnetic and topological contributions to the total signal are presented in figure 3.38 (a) and (b), respectively.
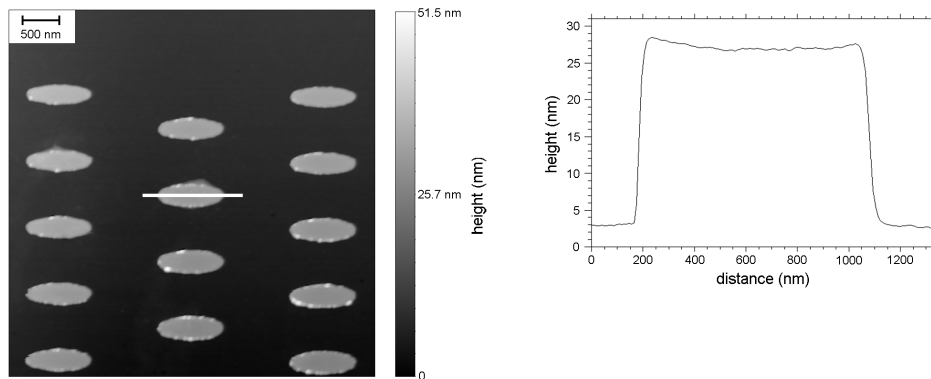
Fig. 3.37: *AFM image and cross section of the topology of the same area as in figure 3.35. The elements have a flat surface with a comparable roughness as the surrounding wafer.*

The magnetic interaction generates a frequency shift of approximately 3Hz originating at the end of the magnetic dipole. The fine structure in the interior of the elements present maximum frequency shifts of $\pm$1Hz. Although the measurements verify that the fine structure is caused by magnetic interactions between the tip and the sample, the origin of these observations remain unsolved. Two possibilities are suggested and will be discussed in the following:

- *Fluctuation in FM magnetization:*
  Domain walls inside the AFM are known as a source of domain patterns in the FM layer as well. Typically, they are formed to close the magnetic flux and to reduce the stray field energy of the total system.

- *Direct imaging of uncompensated spins at the AFM:*
  Uncompensated spins are commonly considered as the origin for the exchange bias effect (see section 1.2.2). In Co/IrMn bilayers, 5 to 10% of the spins at the interface between AFM and FM are considered to be uncompensated [166]. A direct imaging of uncompensated spins was also reported for micro-patterned $Co_{86}Fe_{10}B_4/Mn_{77}Ir_{23}$ by photoemission electron microscopy (PEEM) using x-ray magnetic circular dichroism (XMCD) [167]. First MFM imaging of uncompensated spins in CoO/CoPt perpendicular exchange biased systems was recently presented by KAPPENBERGER et al.[168]

From the existing MFM results, it is not possible to determine if the observed magnetic fine structure is either a result of domains in the FM layer or if it originates from a direct imaging of uncompensated spins. However, the occurrence of domains within the FM layer in sub-micrometer scaled IrMn/CoFeB bilayers is unlikely for two reasons: firstly, no domains are found for the single layer sample at the full range of sizes under investigation. Secondly, the strong intrinsic and shape anisotropy should force the FM layer into a single domain state, which is also indicated by the dipolar contrast in the elements that is a factor of three stronger than the contrast of the fine structure. Furthermore, the XMCD images in Ref. [166] of a comparable exchange bias system shows no multidomain state in the FM layer for elements smaller than approximately $1 \times 1\mu m^2$.[5] For further conclusions, the assumption of direct

---

[5]XMCD measurements allow element specific imaging of the magnetization configuration. At the Co L_3 edge with the element-selective XMCD only the Co moments of the FM layer are probed, with measurements at the Mn L

(a) magnetical contribution

(b) topological contribution
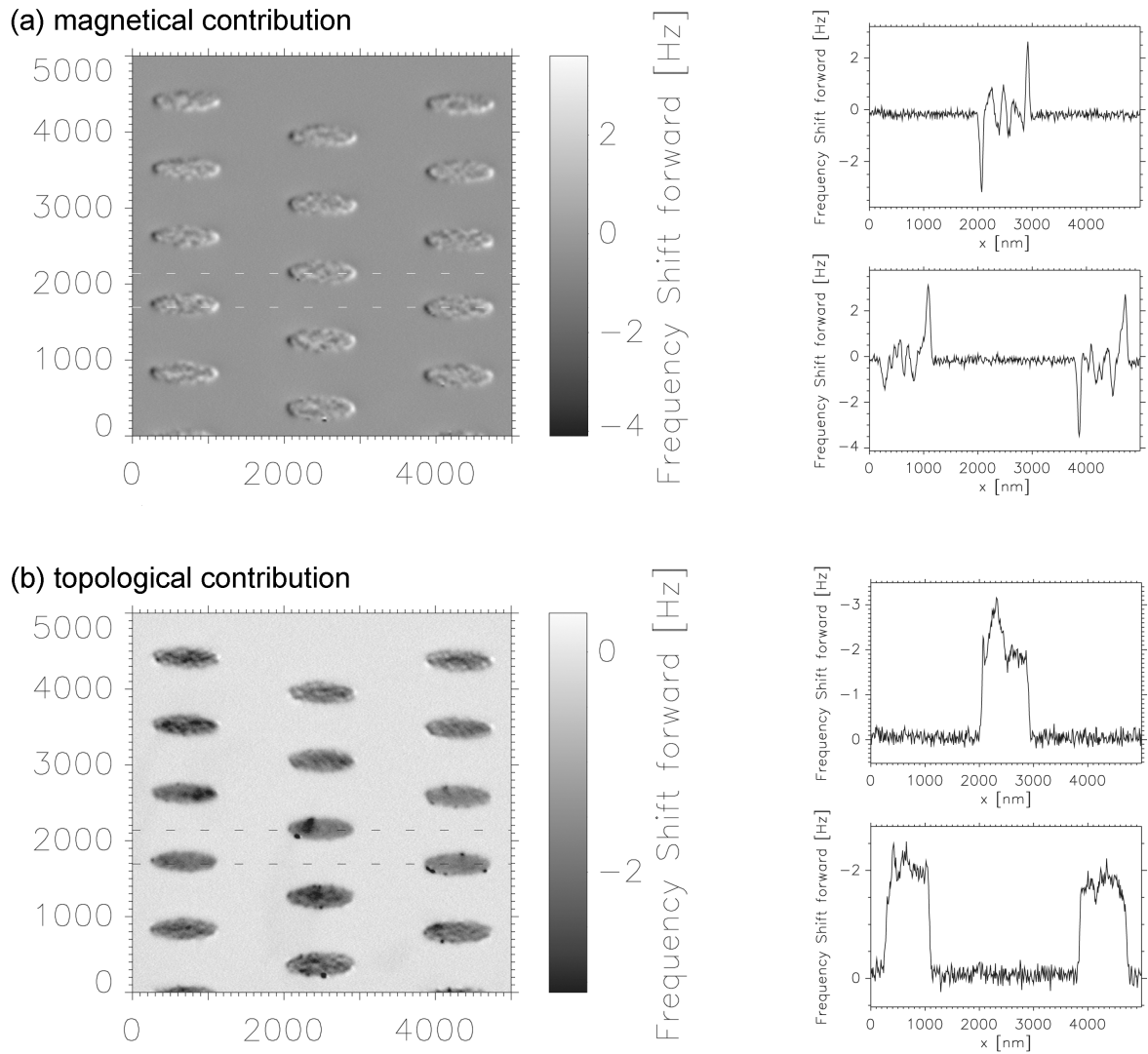
Fig. 3.38: *(a) Calculated magnetic and (b) topological contributions to the total signal as derived from the measurements with different tip magnetization as presented in figure 3.35. Measurements and analysis courtesy of A. Drechsler and G. Tarrach, Swissprobe AG.*

imaging of uncompensated spins by MFM has to be proven by another measurement method, e.g PEEM/XMCD.

Independent of their origin, these fluctuations are of great technological interest and can be a crucial point in scaling down magnetic elements for applications: if the size of the magnetic elements get closer to the typical size of the observed fine structure, a vanishing or, at least, uncontrollable exchange bias is very likely. These fluctuations may explain the observed instabilities in sub-micrometer sized tunnel junctions comprising similar exchange biased hard magnetic electrodes as initially mentioned.

Further investigations are necessary to solve this question and will be addressed in future research within a collaboration between Siemens, Swissprobe and the University of Basel. If the assumption of uncompensated spins as the origin for the observed magnetic fine structure is verified, a first observation of uncompensated spins at the interface of an in-plane magnetized AFM/FM bilayer by means of magnetic force microscopy has been presented in this section.

---

edges a contrast is given by the orientation of the Mn spins within the AFM.

4 Summary

It has been reported by other groups, that a thin film of CoFeB can be used as a soft magnetic electrode in magnetic tunnel junction instead of the commonly used polycrystalline films of NiFe or CoFe. Such amorphous systems show a significantly decreased coercivity, a higher temperature stability, and a smoother interface matching, leading to higher TMR effects.

It has been shown at the laboratories at Siemens, that the concept of amorphous CoFeB layers interfacing the AlO_x barrier can be successfully implemented to our MTJ stack system. To the same time, publications by other groups indicated some advantages by using artificial ferrimagnets in magnetic tunnel junctions. For this thesis, it was the idea to combine both approaches, namely a soft magnetic electrode comprising of two antiferromagnetically coupled layers of an amorphous CoFeB alloy.

It has been presented in the first part of the experimental work, that a stable antiferromagnetic coupling in CoFeB/Ru/CoFeB trilayers exists, if a suitable thickness of the Ru interlayer is chosen. Systematic studies of the interlayer exchange coupling have been performed. In agreement to studies of the RKKY-like coupling in similar (but polycrystalline) trilayer systems, the interlayer coupling in amorphous CoFeB-AFis shows an oscillating behavior and a decrease in amplitude with increasing spacer layer thickness. In comparison to polycrystalline CoFe-AFi systems the coupling strength decreases by approximately a factor of 10. Furthermore, CoFeB-AFis show comparable low coercivities, a narrow distribution of the local anisotropy, a high stability against heat treatments, and could be successful integrated as a soft magnetic electrode in magnetic tunnel junctions. For annealing temperatures higher than 325°C, the coercivity increases abruptly, most likely originated by an onset of crystallization. Only for temperatures above $350 - 370$°C the antiferromagnetic coupling vanishes. These reasonable high thermal stability of coupling, together with the low coercivity and the low distribution of anisotropy, are important properties for potential applications (e.g., as free magnetic layers in sensor elements or in magnetic random access memories).

Finally, it has been found, that the coupling in CoFeB/Ru/CoFeB trilayers show a strong temperature dependence. This is in accordance to the theory and is a result of the low Fermi velocity of electrons in the Ru spacer layer, as also seen for comparable AFis consisting of Ru as the non-magnetic spacer. However, the margin between plateau and saturation field has to be increased, in order to enable applications at elevated temperatures (e.g., in heat assisted MRAM writing schemes, or for spin-flop switching at typical operation temperatures). Possible solutions have been given by comparison with simulations.

The second aim of the thesis was the investigation of CoFeB-AFis at sub-micrometer size. The magnetic multilayers, therefore, have been patterned by e-beam lithography. The resulting patterns have been at sub-micrometer to micrometer range, comparable to sizes of state of the art MRAM devices. It has been proven by MFM analysis, that all elements investigated in this thesis, can be described by a single domain state, in accordance to micromagnetic simulations. This behavior is essential for the reproduced switching of MRAM cells, and is attributed to the strong intrinsic and shape anisotropy of the cells.

With a high sensitive magneto-optical Kerr effect magnetometer, it was possible to investigate

the switching and coupling behavior of these patterned AFis in comparison to CoFeB and NiFe single layers. It has been found, that the coercive field of all samples under study scale with the shape anisotropy. Furthermore, the saturation field of the patterned AFi samples increase with decreasing aspect ratio. This behavior can be explained with an additional contribution of the strayfield coupling between the two layers within the AFi. However, it turns out that the coercivity of the AFi sample increases with respect to single layer elements of the same size, which is in contradiction with results published by others. It has been shown by comparison to micromagnetic simulations that the origin for this result is an increase of effective anisotropy by the additional AF coupling. Therefore, the CoFeB-AFi samples investigated in this thesis cannot be regarded solely as a rigid magnetic body with a decreased (net) magnetic moment.

Finally, the recently reported spin-flop switching scheme was demonstrated for one of the CoFeB-AFi samples. The experimental setup of the Kerr magnetometer was modified for these measurements, since the sample consisted of the soft magnetic electrode only. These experiments show the feasibility of a rapid, non-contact measurement method of the spin-flop switching. However, in order to achieve more information about the switching reliability of the elements, the signal to noise ratio of this method has to be improved.

Thereafter, the exchange bias coupling phenomena between an antiferromagnetic and a ferromagnetic layer has been investigated. In order to implement the amorphous CoFeB layer to both sides of the Al_2O_3 barrier, either a CoFeB single layer or an artificial ferrimagnet can be used as the exchange biased reference layer. To gain more insight in the exchange bias coupling at sub-micrometer size, systems of IrMn/CoFeB have been deposited and patterned by e-beam lithography. MFM studies on these patterns show a magnetic fine structure in the exchange bias system that does not exist in single layer elements of the same geometry. As discussed, this fine structure is most likely attributed to a direct imaging of the interfacial uncompensated spins between IrMn and CoFeB. These results clearly illustrate future challenges for the scaling behavior of exchange bias samples with in-plane magnetization, that not have been addressed in literature with technological relevant material systems so far. Therefore, further experiments (also with PEEM, XMCD) are suggested.

Outlook

Some results in this thesis brought up new questions, or indicate the need for further studies. The most important topics for further investigations are

- *Spin-flop switching*
  One of the most interesting aspects will be a systematic study of the spin-flop switching scheme. The magneto-optical experiment presented in this thesis is more a proof of concept, rather than a systematically study. For further experiments on spin-flop switching, the signal to noise ratio of the setup has to be improved. On the other side, the integration of the CoFeB-AFi in a MTJ full-stack system will allow further experiments on spin-flop switching, not only quasi-static, but also dynamic measurements.

- *Heat-assisted switching*
  The temperature dependence of the unpatterned AFi samples brings up new questions, e.g., how do the sub-micrometer size samples behave at elevated temperatures? Since the heat-assisted writing of MRAM cells is of great technological interest, this question will be addressed in future experiments.

- *Exchange bias properties*
  As already discussed, the exchange bias properties in sub-micrometer size can be a crucial point for downscaling of magnetoresistive devices. The experiments presented in this thesis, therefore, will be continued by detailed MFM studies at the University of Basel.

- *Spin-transfer switching*
  OCHIAI ET AL. have presented spin-transfer experiments by using AFi like structures comparable to the ones investigated in this thesis. As discussed in section 1.4.2, their experiments with spin-transfer switching show a reduction in the critical current density required to turn the magnetization to 1×10^6 A/cm^2 [111, 108]. Therefore, it is obvious to suggest the integration of the investigated CoFe- or CoFeB-AFi systems to low RA magnetoresistive devices. Such TMR multilayer systems seem to be promising for future experiments on spin-transfer switching and the integration to magnetoresistive devices.

A NanoMOKE2^{TM}

A.1 Overview

One can find a huge variety of tools for investigation of the magnetic and transport properties of magnetic thin films and devices at the laboratory of Siemens CT MM 1. At the beginning of my PhD there was no possibility to easily characterize sub-micrometer sized magnetic elements without passing the wafer through a complete lithography process. For rapid magnetic characterization the decision was felled to purchase a high sensitive, spatial resolving magneto-optical Kerr (MOKE) setup (see section 2.2.2).

The NanoMOKE2^{TM}system is an ultra-high sensitivity magneto-optical magnetometer provided by Durham Magneto Optics Ltd. (DMO).[1] It is sensitive to the longitudinal, transverse and polar magneto-optical Kerr effects and is ideally suited to measuring the magnetic properties of thin magnetic films and magnetic nanostructures [169]. Furthermore the tool is using standard electrical, optical and mechanical components mounted on a vibration isolated optical table, thus giving us the possibilities to easily change the setup for different measurement tasks. In more than one year of operation, there have been various modification of the setup and additional software features have been implemented.

A.2 Specifications

Detailed specifications can be obtained from the NanoMOKE2^{TM}manual and specification booklet [169]. The key features of the NanoMOKE2^{TM}system installed at Siemens are:

- Temperature and power stabilized diode laser system.

- Magnetic moments as small as $10^{-12}emu$ can be detected.

- Various lens systems with focus sizes between 2.8 to 5μm for the quadrupole magnet, and 10μm for the dipolar magnet system are provided.

- Computer controlled x-y-θ stage with high accuracy (linear stages with ±12.5mm range and 1μm repeatability, rotation stage with $\pm175°$ range and $0.003°$ repeatability.

- One electromagnet in a quadrupole design and variable pole gaps, generating arbitrary field shapes in the xy-plane of the sample at a maximum magnetic field of 1000Oe (at 10Hz field sweep frequency and the smallest pole gap). A Second dipolar electromagnet can be inserted at the place of the standard quadrupole system, generating fields up to 5000 Oe (at 0.2Hz field sweeping frequency).

- Two analogues outputs (12bit) and two analogues inputs (16bit), simultaneously logged with the Kerr signals.

---

[1]see www.durhammagnetooptics.com for further information

A.3 Hardware modifications

To utilize the basic setup for a broader variety of measurement, various modifications have been carried out, that are described at the following paragraphs.

A.3.1 Temperature stage

To investigate the magnetic properties of exchange biased or AF coupled samples in dependence of the temperature, a simple heating stage has been adapted for the usage at the dipolar magnet system. This heating stage is inserted instead of the x-y-θ stage and enables MOKE measurements ranging from room temperature to approximately $350°$C. The data presented within section 3.1.5 have been obtained with this setup.

A.3.2 Simultaneous measurement of Kerr and magneto-transport signal

A special sample probe has been constructed to combine the spatially resolved magneto-optical measurements with an integral signal of an magneto-resistive sensor element. Therefore, a signal of an electrically contacted sensor element can be measured at the same time as the Kerr data. The laser spot can be focused on different positions of the sample and the data give insight of local magnetization reversal processes on the total (MR) signal behavior.
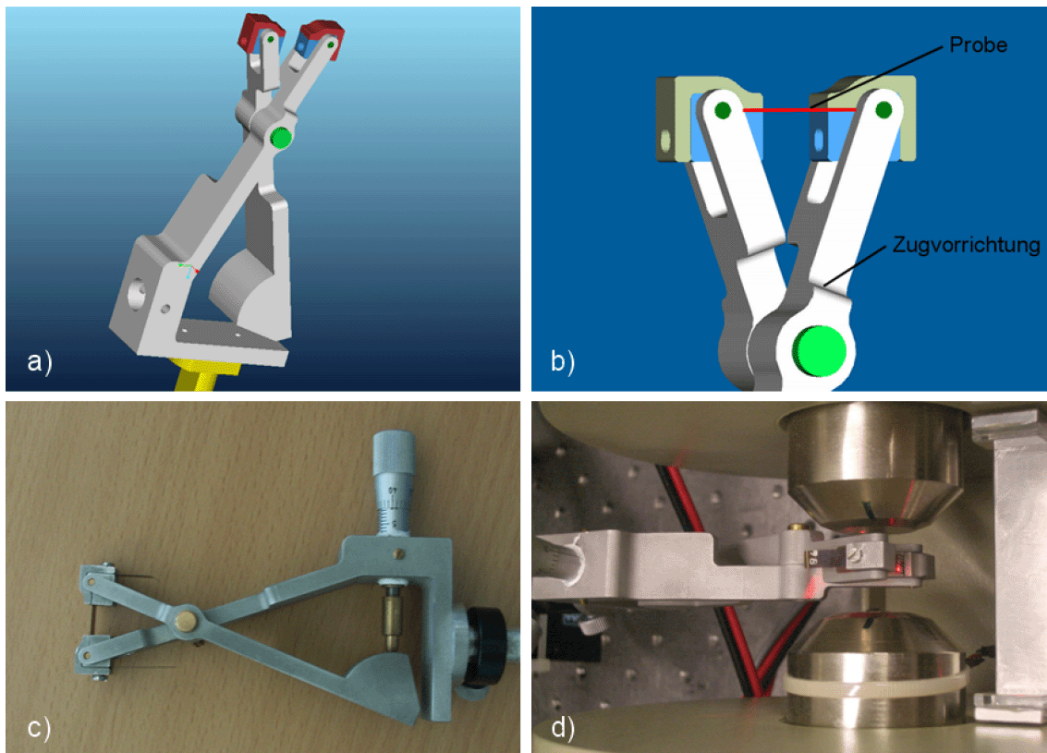

Fig. A.1: *(a)/(b) Three dimensional model and (c)/(d) photographes of the final strain apparatus. All images by courtesy of T. Uhrmann [170].*

A.3.3 Strain sensor

The demonstration of a strain sensor on a flexible polyimide substrate [2] has been investigated within the scope of a diploma thesis [170]. For this purpose, a probe to apply strain on the sample has been constructed for the use in the NanoMOKE2^{TM}setup, providing the possibilities for magnetization measurements in dependence of strain on the sensor elements. The apparatus is shown in figure A.1. Within this thesis, it has been shown for the first time, that a magnetostrictive GMR sensor fabricated on a flexible polyimide substrate can be used as a strain sensor, providing similar (or even higher) MR ratios as comparable GMR element deposited on the usually used SiO_2 substrates. The results are submitted for publication (see Ref. [171]).

A.4 Software add-ons

The software "LX Pro" by DMO controlling the NanoMOKE2 measurements provides basic routines for locating the sample, definition of the applied field sequences, acquiring and processing the data (see figure A.2). All features are integrated in a comfortable graphical user interface, but are also available as an ActiveX component. The latter can be used in external programmes to develop user defined measurement routines. The most convenient way to define own measurements was to implement the LX Pro routines in a Visual Basic programme, since this language is supported by DMO and is easy to learn. Although any other environment supporting ActiveX objects should be possible [169].

All additional software modules developed by myself are put together in a graphical user interface ("LXPro Menu", see figure A.3), and are described in the following paragraphs.[3]

A.4.1 Automated asteroid measurement and evaluation

The asteroid measurements implemented in the "automatic measurement window" allows one to measure angle or bias field dependent asteroids of the switching fields. Additionally to an linear distribution of bias fields, it is possible to choose a non-linear distribution to gain resolution for small bias fields.

For all bias field datapoints a single magnetization loop is taken, that can (semi-) automatically treated by the software module "Asteroid process", resulting in a switching field asteroid $H_c(H_y)$ as described in section 1.3.1. An example for an measured asteroid is shown in figure 3.24.

A.4.2 Position dependent measurement (Mapping)

A basic mapping routine has been implemented to automatically measure magnetization loops at predefined positions. The applied fields are set up in the "automatic measurement" menu and an ASCII file containing the x- and y-positions has to be imported.

It is possible to combine the asteroid measurements with the position list feature. Therefore, it is possible to measure a full switching field asteroid at each predefined position of the wafer.

---

[2]Magnetostrictive GMR sensor deposited and patterned on a flexible polyimide film (Upilex)
[3]The software is available on request, please feel free to contact me.
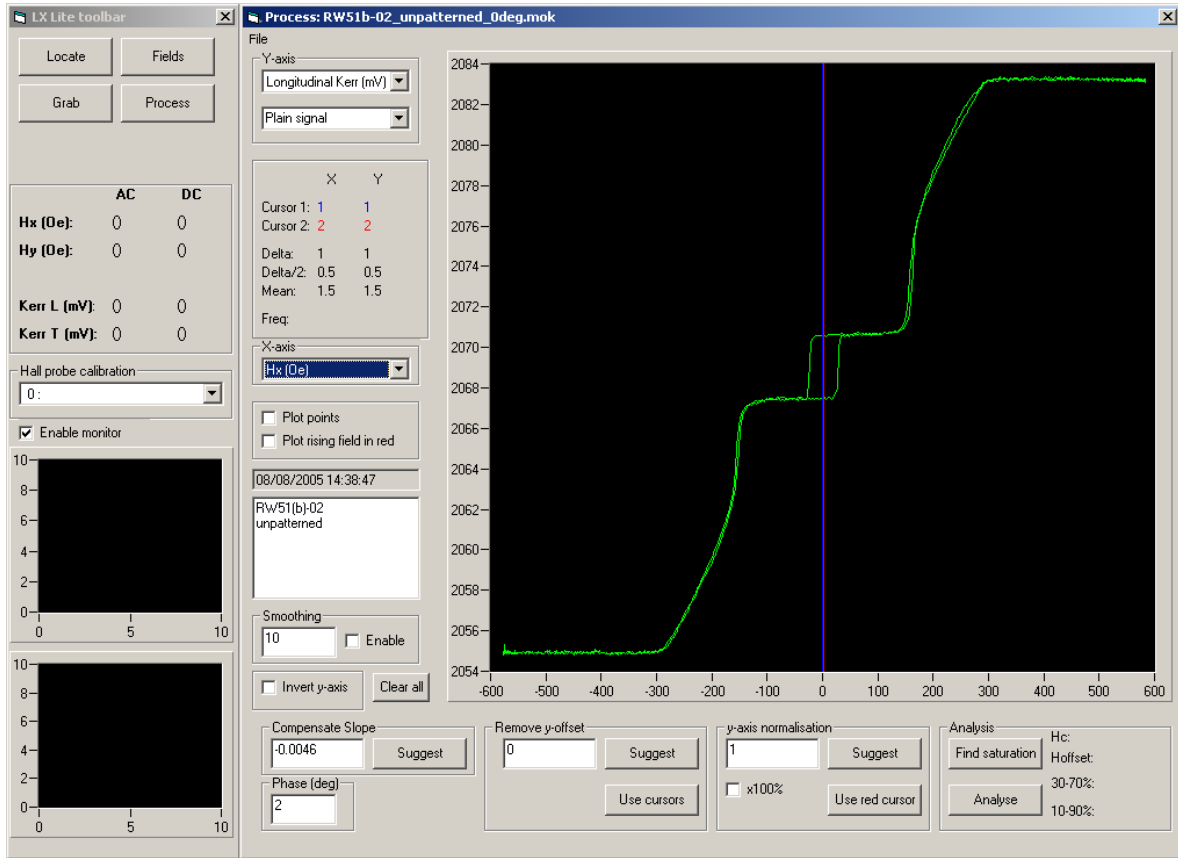
Fig. A.2: *Toolbar and process window of the "LXPro" software, provided by DMO. All basic measurement and process routines can be accessed via the graphical user interface.*

A.4.3 Alignment

Since the magnetic properties, such as coercivity and saturation moment, strongly depend on the angle of the field with respect to the sample (see section 1.3.1), the sample has to be aligned properly. To perform an automatic alignment, one need to give this routine two known points on a vertical or horizontal line. As larger they are separated, as better the accuracy of the alignment will be. The module "Align" is calculating and setting the angle correction, once the user has defined two points. The tool can be called from all panels of "LXPro Menu" via a menu item.

A.4.4 Field Calibration

The Hall sensor elements are located on the top of the pole pieces and have to be calibrated for each pole gap of the electromagnets. For the quadrupole electromagnet the Hall sensors are located at an angle of $45°$ with respect to the x- and y-field planes. A matrix rotation is therefore required to link the Hall voltages with H_x and H_y:

$$\begin{pmatrix} V_1 \\ V_2 \end{pmatrix} = \begin{pmatrix} V_{1x} & V_{1y} \\ V_{2x} & V_{2y} \end{pmatrix} \begin{pmatrix} H_x \\ H_y \end{pmatrix} \tag{A.1}$$

where V_1 and V_2 are the voltages read in by the computer from Hall sensors 1 and 2 respectively, and V_{ij} are the calibration matrix coefficients in units of $\frac{mV}{Oe}$ [169].

A small programme ("EM calibrate") has been written, that automatically evaluates these matrix coefficients. Therefore, a calibrated Hall probe has to be attached to one of the inputs. With this software it is easily possible to verify the calibration regularly and to define new pole gaps if necessary.
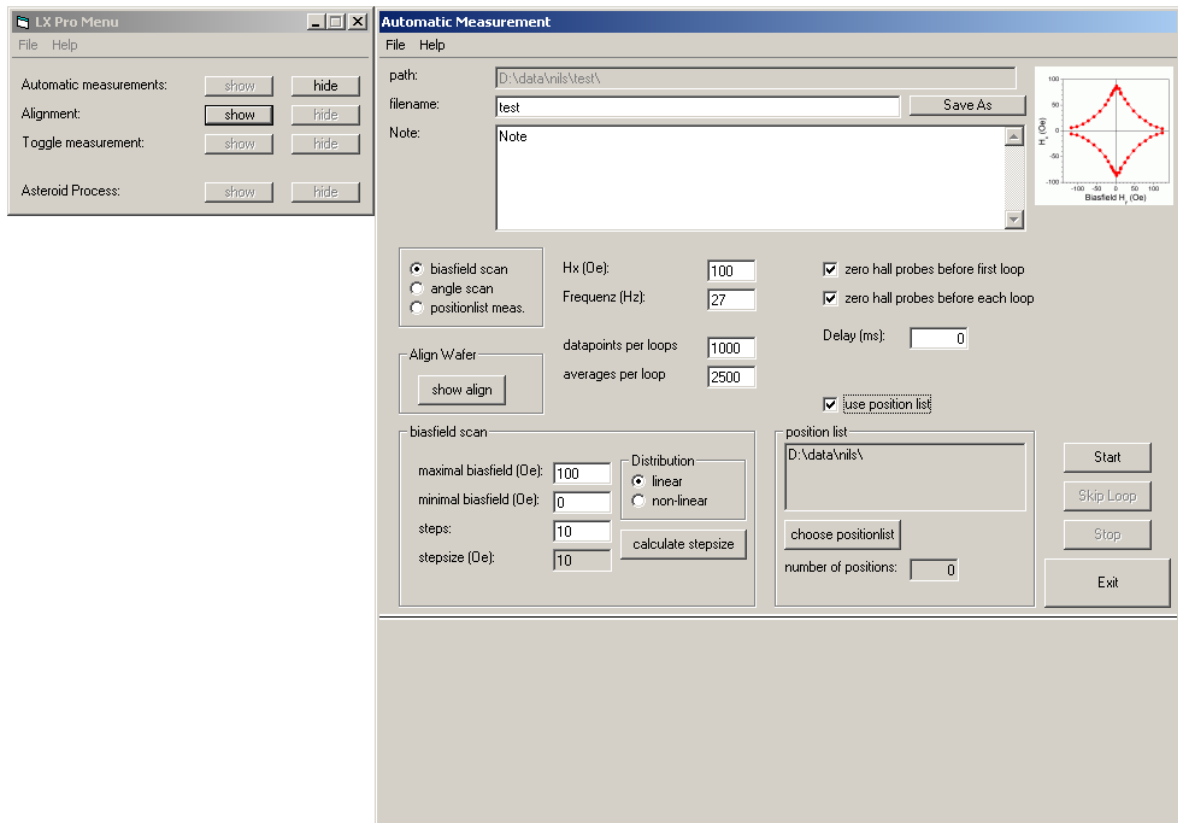

Fig. A.3: *Graphical user interface of the "LXPro Menu" software. The package integrates sub-routines for the automatic asteroid measurements (biasfield, angle, and position dependent), the toggle measurements, the alignment procedures, and a field calibration tool in one program.*

Danksagung

An dieser Stelle möchte ich mich ganz herzlich bei allen bedanken, die entscheidend zu den Ergebnissen beigetragen haben, die in dieser Arbeit zusammengefasst sind.

Als erstes hatte ich aufgrund der Kooperation zwischen der Uni Bielefeld und Siemens, und natürlich aufgrund einiger personeller Veränderungen auf beiden Seiten, das unverschämte Glück, nicht nur einen Betreuer zu haben. Ich hatte gleich eine ganze Reihe davon, namentlich Günter Reiss, Joachim Wecker, Manfred Rührig, Hubert Brückl, und Andreas Hütten. Alle standen mir über die ganze Zeit stets als Ansprech- und Diskussionspartner zur Verfügung.

Ein ganz besonderer Dank geht allerdings an Theo, der mich nicht nur als guter Kollege in der Zeit bei Siemens begleitet hat, sondern über die letzten Jahre auch zu einem guten Freund geworden ist. Er war stets mit kompetenter Hilfe zur Stelle und hat auf unendlich vielen Schmierblättern und mit großartigen Skizzen mein Verständnis für die physikalischen Zusammenhänge erweitert. Er war auch derjenige, der immer wieder meinen Blick auf die wesentlichen Dinge meiner Arbeit gelenkt hat - und einen ungebrochenen Optimismus verbreitete, wenn ich mal wieder das Gefühl hatte, daß ich mich in einer Sackgasse befand.

Auch möchte ich mich bei allen anderen Kollegen in Bielefeld und bei Siemens bedanken, die Proben für mich hergestellt und Messungen für mich gemacht haben. Insbesondere sind das Herr Gieres und Herr Mai (Sputter-Deposition), Karsten (Danke, daß ich immer freie Bahn bei der Lithographie hatte!), Marc und Jan (Auger-Messungen).

Auch sind einige Messungen extern gemacht worden, für die ich mich ganz herzlich bedanken möchte, und zwar bei M. Seibt und Y. Luo (Universität Göttingen) für die TEM-Messungen, bei A. Drechsler und G. Tarrach für die MFM-Messungen (Swissprobe AG), bei J. Kanak and T. Stobiecki (Universität Krakau) für die XRD-Untersuchungen und bei A. Gentils und S. McVitie (Universität Glasgow) für die Versuche mit Lorentz-Mikroskopie an den AFi-Proben.

Also, thanks to all the people that read my manuscript and did all the corrections, especially to Michelle, Tammy and Daniel - I promise to improve my English!!!

Finally, I acknowledge John Chapman for the opportunity to start with my "Postdoc", while still writing at my thesis. This offer made a seamless transition from Siemens to the University of Glasgow possible in the first place.

Mein größter Dank gilt aber all' der unermüdlichen Unterstützung, die ich von meinen Eltern, meiner Freundin Nadja, und meinen "Ersatz-Eltern" Nazlı und Uli bekommen habe - ihr habt alle einen Orden von mir verdient!!!

Bibliography

[1] M. Ho et al., *Study of magnetic tunnel junction read sensors*, IEEE Trans. Magn. **37**, 1691 (2001).

[2] H. A. M. van den Berg et al., IEEE Trans. Magn. **35**, 2892 (1999).

[3] M. Löhndorf et al., *Highly sensitive strain sensors based on magnetic tunneling junctions*, Appl. Phys. Lett. **81**, 313 (2002).

[4] W. J. Gallagher et al., *Microstructured magnetic tunnel junctions*, J. Appl. Phys. **81**, 3741 (1997).

[5] R. Richter, *Logic gates realized with spin dependent tunneling elements*, PhD thesis, University of Bielefeld, http://bieson.ub.uni-bielefeld.de/volltexte/2003/235/, 2002.

[6] D. A. Allwood et al., *Magnetic Domain-Wall Logic*, Science **309**, 1688 (2005).

[7] M. Johnson, and R. H. Silsbee, *Interfacial charge-spin coupling: Injection and detection of spin magnetization in metals*, Phys. Rev. Lett. **55**, 1790 (1985).

[8] S. Datta, and B. Das, *Electronic analog of the electro-optic modulator*, Appl. Phys. Lett. **56**, 665 (1990).

[9] J. C. Slonczewski, *Current-driven excitation of magnetic multilayers*, J. Magn Magn. Mater. **159**, L1 (1996).

[10] L. Berger, *Emission of spin waves by a magnetic multilayer traversed by a current*, Phys. Rev. B **54**, 9353 (1996).

[11] J. L. Simonds, *Magnetoelectronics Today and Tomorrow*, Physics Today (1995).

[12] J. S. Moodera, and G. Mathon, *Spin polarized tunneling in ferromagnetic junctions*, J. Magn. Magn. Mater. **200**, 248 (1999).

[13] J. Gregg, I. Petey, E. Jouguelet, and C. Dennis, *Spin electronics - a review*, J. Phys. D: Appl. Phys. **35**, R121 (2002).

[14] G. A. Prinz, *Magnetoelectronics applications*, J. Magn. Magn. Mater. **200**, 57 (1999).

[15] Y. Wu, *Nano Spintronics for Data Storage*, Encyclopedia of Nanoscience and Nanotechnology , 1 (2003).

[16] P. R. LeClair, *Fundamental Aspects of Spin Polarized Tunneling*, Dissertation, Universiteit Eindhoven, 2002.

[17] Messiah, *Quantenmechanik* (de Gruyter, 1976).

[18] J. G. Simmons, *Generalized Formula for the Electric Tunnel Effect between Similar Electrodes Separated by a Thin Insulating Film*, J. Appl. Phys. **34**, 1793 (1963).

[19] W. F. Brinkman, R. C. Dynes, and J. M. Rowell, *Tunneling Conductance of Asymmetrical Barriers*, J. Appl. Phys. **41**, 1915 (1970).

[20] R. Meservey, P. M. Tedrow, and P. Fulde, *Magnetic Field Splitting of the Quasiparticle States in Superconducting Aluminum Films*, Phys. Rev. Lett. **25**, 1270 (1970).

[21] P. M. Tedrow, and R. Meservey, *Spin-Dependent Tunneling into Ferromagnetic Nickel*, Phys. Rev. Lett. **26**, 192 (1971).

[22] M. Julliere, *Tunneling betwen ferromagnetic films*, Physics Letters A **54**, 225 (1975).

[23] T. Miyazaki, and N. Tezuka, *Giant magnetic tunneling effect in Fe/Al2O3/Fe junction*, J. Magn. Magn. Mater. **139**, L231 (1995).

[24] J. S. Moodera, L. R. Kinder, T. M. Wong, and R. Meservey, *Large magnetoresistance at room temperature in ferromagnetic thin film tunnel junctions*, Phys. Rev. Lett. **74**, 3273 (1995).

[25] A. Käufler et al., *Tunnel-magnetoresistance system with an amorphous detection layer*, J. Appl. Phys. **91**, 1701 (2002).

[26] D. Wang, C. Nordman, J. M. Daughton, Z. Qian, and J. Fink, *70% TMR at Room Temperature for SDT Sandwich Junctions With CoFeB as Free and Reference Layers*, IEEE Trans Magn. **40**, 2269 (2004).

[27] J. M. Schmalhorst, *Magnetische, thermische und dielektrische Stabilität von magnetischen Tunnelelementen*, Phd thesis, Universität Bielefeld, 2001.

[28] P. Rottländer, M. Hehn, O. Lenoble, and A. Schuhl, *Tantalum oxide as an alternative low height tunnel barrier in magnetic junctions*, Appl. Phys. Lett. **78**, 3274 (2001).

[29] M. Guth, A. Dinia, G. Schmerber, and H. A. M. van den Berg, *Tunnel magnetoresistance in magnetic tunnel junctions with ZnS barrier*, Appl. Phys. Lett. **78**, 3487 (2001).

[30] J. Wang, P. P. Freitas, E. Snoeck, X. Battle, and J. Cuadra, *Tunnel junction with FeTaN electrodes and AlN barriers*, IEEE Trans. Magn. **38**, 2703 (2002).

[31] T. Dimopoulos et al., *Magnetic tunnel junctions with yttrium oxide barrier*, Appl. Phys. Lett. **83**, 3338 (2003).

[32] W. H. Butler, X.-G. Zhang, T. C. Schulthess, and J. M. MacLaren, *Spin-dependent tunneling conductance of FezMgOzFe sandwiches*, Phys. Rev. B **63**, 054416 (2001).

[33] J. Mathon, and A. Umerski, *Theory of tunneling magnetoresistance of an epitaxial Fe/MgO/Fe(001) junction*, Phys. Rev. B **63**, 220403 (2001).

[34] X.-G. Zhang, and W. H. Butler, *Large magnetoresistance in bcc Co/MgO/Co and FeCo/MgO/FeCo tunnel junctions*, Phys. Rev. B **70**, 172407 (2004).

[35] J. Faure-Vincent et al., *High tunnel magnetoresistance in epitaxial Fe/MgO/Fe tunnel junctions*, Appl. Phys. Lett. **82**, 4507 (2003).

[36] S. Yuasa, T. Nagahama, A. Fukushima, Y. Suzuki, and K. Ando, *Giant room-temperature magnetoresistance in single-crystal Fe/MgO/Fe magnetic tunnel junctions*, Nature Materials **3**, 868 (2004).

[37] S. S. P. Parkin et al., *Giant tunnelling magnetoresistance at room temperature with MgO (100) tunnel barriers*, Nature Materials **3**, 862 (2004).

[38] M. Hehn et al., *Low-height sputter-deposited magnesium oxide tunnel barriers: experimental report and free electron modeling*, Eur. Phys. J. B **40**, 19 (2004).

[39] T. Dimopoulos et al., *Large tunnel magnetoresistance with plasma oxidized MgO barriers*, J. Appl. Phys. **98**, 073705 (2005).

[40] S. I. ansd J. Hayakawa et al., *Dependence of tunnel magnetoresistance in MgO based magnetic tunnel junctions Ar pressure during MgO sputtering*, arXiv:cond-mat , 0510531 (2005).

[41] H. A. M. van den Berg et al., *GMR sensor scheme with artificial antiferromagnetic subsystem*, IEEE Trans. Magn. **32**, 4624 (1996).

[42] H. A. M. van den Berg et al., *GMR angle detector with a artificial antiferromagnetic subsystem (AAF)*, J. Magn. Magn. Mater. **165**, 524 (1997).

[43] P. Grünberg, R. Schreiber, Y. Pang, M. B. Brodsky, and H. Sowers, *Layered Magnetic Structures: Evidence for Antiferromagnetic Coupling of Fe Layers across Cr Interlayers*, Phys. Rev. Lett. **57**, 2442 (1986).

[44] M. N. Baibich et al., *Giant Magnetoresistance of (001)Fe/(001)Cr Magnetic Superlattices*, Phys. Rev. Lett. **61**, 2472 (1988).

[45] G. Binasch, P. Grünberg, F. Saurenbach, and W. Zinn, *Enhanced magnetoresistance in layered magnetic structures with antiferromagnetic interlayer exchange*, Phys. Rev. B **39**, 4828 (1989).

[46] S. S. P. Parkin, N. More, and K. P. Roche, *Oscillations in Exchange Coupling and Magnetoresistance in Metallic Superlattice Structures: Co/Ru, Co/Cr, and Fe/Cr*, Phys. Rev. Lett. **64**, 2304 (1990).

[47] R. Coehoorn, *Period of oscillatory exchange interactions in Co/Cu and Fe/Cu multilayer systems*, Phys. Rev. B **44**, 9331 (1991).

[48] B. A. Jones, *Theory of exchange coupling in magnetic multilayers*, IBM Journal of Research and Development **42**, 25 (1998).

[49] Y. Yafet, *Ruderman-Kittel-Kasuya-Yosida range function of a one-dimensional free-electron gas*, Phys. Rev. B **36**, 3948 (1987).

[50] P. Bruno, and C. Chappert, *Oscillatory Coupling between Ferromagnetic Layers Separated by a Nonmagnetic Metal Spacer*, Phys. Rev. Lett. **67**, 1602 (1991).

[51] W. Battensperger, and J. S. Helman, *Ruderman-Kittel coupling between ferromagnets separated by a nonmagnetic layer*, J. Appl. Phys. **57**, 2954 (1990).

[52] M. D. Stiles, *Interlayer exchange coupling*, J. Magn. Magn. Mater. **200**, 322 (1999).

[53] D. E. Buergler, *Zwischenschichtaustauschkopplung: Abhängigkeit vom Schichtaufbau und der Qualität der Grenzflächen* (Forschungszentrum Jülich, 1999), Kap. B10, Seiten B10.1 – B10.20.

[54] N. Persat, and A. Dinia, *Strong temperature dependence of the interlayer exchange coupling strength in Co/Cu/Co sandwiches*, Phys. Rev. B **56**, 2676 (1997).

[55] M. D. Stiles, *Exchange Coupling in Magnetic Multilayers*, Concepts Condens. Mat. Phys. **in press**, 1 (2005).

[56] T. Dimopoulos, *Transport polarisé en spin dans les jontions tunnel magnétiques: Le role des interfaces métal/oxyde dans le processus tunnel*, PhD thesis, Université Louis Pasteur de Strasbourg, 2002.

[57] B. Dieny, J. P. Gavigan, and J. P. Rebouillat, *Magnetisation processes, hysteresis and finite-size effects in model multilayer systems of cubic or uniaxial anisotropy with antiferomagnetic coupling between adjacent ferromagnetic layers*, Journal of Physics: Condensed Matter **2**, 159 (1990).

[58] W. Folkerts, *Calculated magnetic phase diagrams and magnetoresistance curves for an antiferromagnetically coupled multilayer system*, J. Magn. Magn. Mater. **94**, 302 (1991).

[59] J. M. Slaughter et al., *Fundamentals of MRAM Technology*, Journal of Superconductivity: Incorporating Novel Magnetism **15**, 19 (2001).

[60] B. N. Engel et al., *A 4-Mb Toggle MRAM Based on a Novel Bit and Switching Method*, IEEE Trans. Magn. **41**, 132 (2005).

[61] S. Sousa, Z. Zhang, and P. Freitas, *Synthetic ferrimagnet free layer tunnel junction for magnetic random access memories*, J. Appl. Phys. **91**, 7700 (2002).

[62] N. Tezuka, N. Koike, K. Inomata, and S. Sugimoto, *Magnetization reversal and domain structure of antiferromagnetically coupled submicron elements*, J. Appl. Phys. **93**, 7441 (2003).

[63] N. Wiese et al., *Antiferromagnetically coupled CoFeB/Ru/CoFeB trilayers*, Appl. Phys. Lett. **85**, 2020 (2004).

[64] N. Wiese et al., *Magnetic properties of antiferromagnetically coupled CoFeB/Ru/CoFeB*, J. Magn. Magn. Mater. **290-291**, 1427 (2005).

[65] Z. Celinski et al., *Growth and magnetic studies of lattice expanded Pd in ultrathin Fe(001)/Pd(001)/Fe(001) structures*, Phys. Rev. Lett. **65**, 1156 (1990).

[66] D. M. Edwards, J. Mathon, R. B. Muniz, and M. S. Phan, *Oscillations of the exchange in magnetic multilayers as an analog of de Haas-van Alphen effect*, Phys. Rev. Lett. **67**, 493 (1991).

[67] J. R. Cullen, and K. B. Hathaway, *Temperature dependence of the exchange energy and critical field for antiferromagnetically coupled thin films and superlattices*, Phys. Rev. B **47**, 14998 (1993).

[68] Z. Zhang, L. Thou, P. Wigen, and K. Ounadjela, *Using ferromagnetic resonance as a sensitive method to study temperature dependence of interlayer exchange coupling*, Phys. Rev. Lett. **73**, 336 (1994).

[69] M. D. Stiles, *Interlayer Exchange Coupling* (in "Ultrathin Magnetic Structures III", Springer, 2004), .

[70] W. H. Meiklejohn, and C. P. Bean, *New magnetic anisotropy*, Phys. Rev. **102**, 1413 (1956).

[71] W. H. Meiklejohn, and C. P. Bean, *New magnetic anisotropy*, Phys. Rev. **105**, 904 (1957).

[72] A. E. Berkowitz, and K. Takano, *Exchange anisotropy - a review*, J. Magn. Magn. Mater. **200**, 552 (1999).

[73] D. Mauri, H. C. Siegmann, P. S. Bagus, and E. Kay, *Simple model for thin ferromagnetic films exchange coupled to an antiferromagnetic substrate*, J. Appl. Phys. **62**, 3047 (1987).

[74] A. P. Malozemoff, *Random-field model of exchange anisotropy at rough ferromagnetic-antiferromagnetic interfaces*, Phys. Rev. B **35**, 3679 (1987).

[75] A. P. Malozemoff, *Heisenberg-to-Ising crossover in a random-field model with uniaxial anisotropy*, Phys. Rev. B **37**, 7673 (1988).

[76] N. C. Koon, *Calculations of exchange bias in thin films with ferromagnetic/antiferromagnetic interfaces*, Phys. Rev. Lett. **78**, 4865 (1997).

[77] K. Takano, R. H. Kodama, A. E. Berkowitz, W. Cao, and G. Thomas, *Interfacial uncompensated antiferromagnetic spins: Role in unidirectional anisotropy in polycrystalline NiFe/CoO bilayers*, Phys. Rev. Lett. **79**, 1130 (1997).

[78] R. L. Stamps, *Mechanisms for exchange bias*, J. Phys. D: Appl. Phys. **33**, R247 (2000).

[79] J. Nogues, and I. K. Schuller, *Exchange bias*, J. Magn. Magn. Mater **192**, 203 (1999).

[80] L. Neel, and C. R. Hebd, Seances Acad. Sci. **255**, 1676 (1962).

[81] B. D. Schrag et al., *Néel 'orange-peel' coupling in magnetic tunneling junction devices*, Appl. Phys. Lett. **77**, 2373 (2000).

[82] J. Kools, T. G. S. M. Rijks, E. D. Veirmanaan, and R. Coehoorn, *On the Ferromagnetic Interlayer Coupling in Exchange-Biased Spin-Valve Multilayers*, IEEE Trans. Magn. **31**, 3918 (1995).

[83] J. Zhang, and R. M. White, *Topological coupling in spin valve type multilayers*, IEEE Trans. Magn. **32**, 4630 (1996).

[84] J. C. S. Kools, W. Kula, D. Mauri, and T. Linn, *Effect of finite magnetic film thickness on Néel coupling in spin valves*, J. Appl. Phys. **85**, 4466 (1999).

[85] K. Y. Kim, S. H. Jang, K. H. Shin, H. J. Kim, and T. Kang, *Interlayer coupling field in spin valves with CoFe/Ru/CoFe/FeMn synthetic antiferromagnets*, J. Appl. Phys. **89**, 7612 (2001).

[86] D. Wang et al., *Spin dpendent tunneling junctions with reduced Neel coupling*, J. Appl. Phys. **93**, 8558 (2003).

[87] F. J. Himpsel, J. E. Ortega, G. J. Mankey, and R. F. Willis, *Magnetic Nanostructures: Fabrication and Electronic States*, Advances in Physics **47**, 511 (1998).

[88] K.-S. Moon, R. Fontana, and S. S. P. Parkin, *Exchange-biased magnetic tunnel junctions: Dependence of offset field on junction width*, Appl. Phys. Lett. **74**, 3690 (1999).

[89] D. W. Abraham, and Y. Lu, *Precision measurement of dipole fields and moments in sub-micron magnetic particles*, 9th Joint MMM/Intermag, Anaheim Conference , BE (2004).

[90] D. W. Abraham, and Y. Lu, *Observation of switching of magnetic particle arrays with weak dipole interaction field effect*, J. Appl. Phys. **98**, 023903 (2005).

[91] W. Rave, K. Fabian, and A. Hubert, *Magnetic states of small cubic particles with uniaxial anisotropy*, J. Magn. Magn. Mater. **190**, 332 (1998).

[92] A. Hubert, and R. Schäfer, *Magnetic domains* (Springer, 1998).

[93] E. C. Stoner, and E. P. Wohlfarth, *A mechanism of magnetic hysteresis in heterogenous alloys*, Phil. Trans. Roy. Soc. A **240**, 599 (1948).

[94] J. Slaughter, Mram technology: Status and future challanges, Talk at the Cornell CNS Nanotechnology Symposium, 2004.

[95] J. Osborn, *Demagnetizing factors of the general ellipsoid*, Phys. Rev. **67**, 351 (1945).

[96] L. Sun, Y. Hao, C.-L. Chien, and P. Searon, *Tuning the properties of magnetic nanowires*, IBM J. Res. & Dev. **49**, 79 (2005).

[97] J. Z. Sun et al., *Thermal activation-induced sweep-rate dependence of magnetic switching astroid*, Appl. Phys. Lett. **78**, 4004 (2001).

[98] R. H. Koch et al., *Magnetization reversal in micron-sized magnetic thin films*, Phys. Rev. Lett. **81**, 4512 (1998).

[99] D. C. Worledge, *Magnetic phase diagram of two identical coupled nanomagnets*, Appl. Phys. Lett. **84**, 2847 (2004).

[100] D. C. Worledge, *Spin flop switching for magnetic random access memory*, Appl. Phys. Lett. **84**, 4559 (2004).

[101] D. C. Worledge, private communications.

[102] M. Durlam et al., *A 0.18 µm 4Mb Toggling MRAM*, Tech. Dig. - Int. Electron Devices Meet. (IEDM) **session 34, paper 6** (2005).

[103] L. Savtchenko, B. N. Engel, N. D. Rizzo, M. F. Deherrera, and J. A. Janesky, *Method of writing to scalable magnetoresitance random access memory element*, U.S. Patent No. 6,545,906, 2003.

[104] J.-V. Kim, T. Devolder, C. Chappert, C. Maufront, and R. Fournel, *Precession-dominated switching of synthetic antiferromagnets*, Appl. Phys. Lett. **85**, 4094 (2004).

[105] H. T. Nembach et al., *Ultrafast direct writing scheme with unipolar field pulses for synthetic antiferromagnetic magnetic random access memory cells*, Appl. Phys. Lett. **87**, 142503 (2005).

[106] J. A. Katine, F. J. Albert, R. A. Buhrman, E. B. Myers, and D. C. Ralph, *Current-Driven Magnetization Reversal and Spin-Wave Excitations in Co/Cu/Co Pillars*, Phys. Rev. Lett. **84**, 3149 (2000).

[107] F. J. Albert, J. Katine, R. A. Buhrman, and D. C. Ralph, *Spin-polarized current switching of Co thin film nanomagnets*, Appl Phys. Lett. **77**, 3809 (2000).

[108] Y. Huai, M. Pakala, Z. Diao, and Y. Ding, *Spin transfer switching current reduction in magnetic tunnel junction based dual spin filter structures*, Appl Phys. Lett. **87**, 222510 (2005).

[109] K. Yagami, A. A. Tulapurkar, A. Fukushima, and Y. Suzuki, *Low-current spin-transfer switching and its thermal durability in a low-saturation-magnetization nanomagnet*, Appl Phys. Lett. **85**, 5634 (2004).

[110] Y. Jiang et al., *Substantial reduction of critical current for magnetization switching in an exchange-biased spin valve*, Nature Materials **3**, 361 (2004).

[111] T. Ochiai et al., *Distinctive current-induced magnetization switching in a current-perpendicular-to-plane giant-magnetoresistance nanopillar with a synthetic antiferromagnetic free layer*, Appl Phys. Lett. **86**, 242506 (2005).

[112] A. Hubert, and G. Traeger, *Magneto-optical sensitivity functions of thin-film systems*, J. Magn. Magn. Mater. **124**, 185 (1993).

[113] L. D. Landau, and E. Lifshitz, *On the theory of the dispersion of magnetic permeabilty in ferromagnetic bodies*, Phys. Z. Sowjetunion **8**, 153 (1935).

[114] O. Stemme, *Dünne Permalloyschichten mit Mosaikstruktur für die Datenspeicherung*, Telefunken-Zeitung **3/4**, 403 (1966).

[115] D. Meyners, *Domänenuntersuchungen an nanostrukturierten magnetischen Tunnelelementen*, Diplomarbeit, University of Bielefeld, 2001.

[116] M. J. Donahue, D. G. Porter, R. D. McMichael, and J. Eicke, *OOMMF 2D solver - advanced details, OOMMF Workshop, Gaithersburg, MD*, 2000.

[117] L. Maissel, *Application of Sputtering to the Deposition of Films* (in "Handbook of Thin Film Technology", McGraw Hill, 1983), Kap. 4.

[118] G. K. Wehner, and G. S. Anderson, *The Nature of Physical Sputtering* (in "Handbook of Thin Film Technology", McGraw Hill, 1983), Kap. 3.

[119] D. Meyners, *Sub-micrometer scaled magnetic logic*, PhD thesis, University of Bielefeld, 2006.

[120] E. F. Wassermann et al., *Fabrication and Characterization of Large Scale Periodic Magnetic Nanostructures*, J. Appl. Phys. **83**, 1753 (1998).

[121] A. Carl, S. Kirsch, and E. F. Wassermann, *Large scale periodic magnetic nanostructures fabricated by optical interference lithography*, Mat. Res. Soc. Symp. Proceedings **705**, Y9.2 (2002).

[122] D. J. Resnick, S. V. Sreenivasan, and C. G. Willson, *Step & Flash imprint technology*, Materials Today , 34 (2005).

[123] S. V. Sreenivasan et al., *Enhanced nanoimprint process for advanced lithography applications*, Semiconductor Fabtech **25th edition** (2005).

[124] T. Zell, *Lithography*, 2001, Vortragsskript zur 2. Dresdner Sommerschule Mikroelektronik.

[125] T. Ito, and S. Okazaki, *Pushing the limits of lithography*, Nature **406**, 1027 (2000).

[126] H. Koop, *Untersuchung des Einflusses der geometrischen Form auf das Schaltverhalten magnetischer Tunnelelemente im sub-micrometer Grössenbereich*, PhD thesis, University of Bielefeld, 2004.

[127] H. Koop, H. Brückl, D. Meyners, and G. Reiss, *Shape dependence of the magnetization reversal in sub-micrometer magnetic tunnel junctions*, J. Magn. Magn. Mater. **272-276**, e1475 (2004).

[128] R. Glang, and L. V. Gregor, *Generation of Patterns in Thin Films* (in "Handbook of Thin Film Technology", McGraw Hill, 1983), Kap. 7.

[129] Zeiss LEO, *Manual of LEO 1530 scanning electron microscope.*

[130] M. A. McCord, and M. J. Rooks, *Electron Beam Lithography* (SPIE Press, 1997), Kap. 2, Seiten 139–249.

[131] H. G. Craighead, *Lateral Patterning of Nanostructures.*

[132] Allresist GmbH, *Copolymer PMMA/MA 33% als E-Beam Resistserien, AR-P 610 in 2-Methoxyethanol und AR-P 617 in 1-Methoxy-2-propanol*, product data sheet, 2004.

[133] Allresist GmbH, *Entwickler AR 600-50, 600-51, 600-55 und 600-56 für die E-Beam Resistserien AR-P 610/617, 631/639 - 671/679 und 6510*, product data sheet, 2005.

[134] Allresist GmbH, *Stopper AR 600-60, 600-61 für die E-Beam Resistsserien AR-P 610/617, 631/639 - 671/679 und 6510*, product data sheet, 2005.

[135] Allresist GmbH, *Remover AR 600-80 und AR 300-70, 300-72, 300-73 zur Entfernung von Resistschichten*, product data sheet, 2005.

[136] S. Büttgenbach, *Mikromechanik* (Teubner Studienbücher).

[137] L. F. Fuller, *Pattern Generation Techniques* (McGraw-Hill, 1998), Kap. 2, Seiten 1–39.

[138] P. J. Flanders, *Alternating-gradient magnetometer*, J. Appl. Phys. **63**, 3940 (1988).

[139] Princeton Measurement Corp., *AGM/VSM manual*, 2002.

[140] M. Faraday, Trans. R. Soc. **5**, 592 (1846).

[141] J. Kerr, Philos. Mag. **3**, 339 (1877).

[142] J. Kerr, Philos. Mag. **5**, 161 (1878).

[143] J. C. Maxwell*Electricity and Magnetism* Vol. 2 (, 1873).

[144] Z. Q. Qiu, and S. D. Bader, *Surface magneto-optic Kerr effect*, Rev. Sci. Instr. **71**, 1243 (2000).

[145] S. Heitmann, *Co/Cu multilayers: Interplay of microstructure and GMR and recrystallization as the key towards temperature stability*, Phd thesis, Universität Bielefeld, 2004.

[146] Bergmann, and Schaefer, *Lehrbuch der Experimentalphysik - Festkörper* (De Gruyter, 1992).

[147] ETH Zürich, *Transmission Electron Microscopy*, Website: http://www.microscopy.ethz.ch/elmi-index.htm, last visited: 2005/12/18.

[148] D. B. Williams, and C. B. Carter, *Transmission Electron Microscopy* (Plenum Press, 1996).

[149] G. Binnig, H. Rohrer, C. Gerber, and E. Weibel, *Surface studies by scnning tunneling microscopy*, Phys. Rev. Lett. **49**, 57 (1981).

[150] R. Howland, and L. Benatar, *A practical guide to scanning probe microscopy* (Park Scientific Instruments, 1993-2000).

[151] *High resolutions magnetic force microscope (hr-MFM)*, Swissprobe Ltd., Brochure and specification booklet, 2005.

[152] T. Dimopoulos, G. Gieres, J. Wecker, N. Wiese, and M. D. Sacher, *Thermal annealing of junctions with amorphous and polycrystalline ferromagnetic electrodes*, J. Appl. Phys. **96**, 6382 (2004).

[153] M. Jimbo et al., *Thermal stability of spin valves using amorphous CoFeB*, J. Magn. Magn. Mater. **165**, 308 (1997).

[154] M. Rührig, *Mikromagnetische Untersuchungen an gekoppelten weichmagnetischen Mehrfachschichten*, Phd thesis, Universität Erlangen, 1993.

[155] W. A. Challener et al., *Light delivery techniques for heat-assisted magnetic recording*, Jpn. J. Appl. Phys. **42**, 981 (2003).

[156] I. L. Prejbeanu et al., *Thermally assisted switching in exchange-biased storage layer magnetic tunnel junctions*, IEEE Trans. Magn. **40**, 2625 (2004).

[157] S. Schwieger, and W. Nolting, *Origin of the temperature dependence of interlayer exchange coupling in metallic trilayers*, Phys. Rev. B **69**, 224413 (2004).

[158] T. Stobiecki, *personal communications.*

[159] Y. Luo et al., *Co-rich magnteic amorphous films and their application in magnetoelectronics*, Phys. Rev. B **72**, 014426 (2005).

[160] A. T. G. Pym et al., *Interface sharpening in CoFeB magnetic tunnel junctions*, submitted to Appl. Phys. Let. (2006).

[161] D. Meyners, H. Brückl, and G. Reiss, *Influence of boundary roughness on the magnetization reversal in submicron sized magnetic tunnel junctions*, J. Appl. Phys. **93**, 2676 (2003).

[162] Y.-H. Wang et al., *The switching behaviors of submicron magnetic tunnel junctions with synthetic antiferromagnetic free layers*, J. Appl. Phys. **97**, 10C923 (2005).

[163] N. Wiese, T. Dimopoulos, M. Rührig, J. Wecker, and G. Reiss, *Switching of submicrometer sized, antiferromagnetically coupled CoFeB/Ru/CoFeB trilayers*, J. Appl. Phys. **98**, 103904 (2005).

[164] The commercial available micromagnetic program llg micromagnetics simulator [TM], developed by m.r. scheinfein, was used; see http://llgmicro.home.mindspring.com.

[165] D. Meyners, *personal communications at the magneto-logic meeting*, 2005.

[166] H. Ohldag et al., *Correlation between exchange bias and pinned interfacial spins*, Phys. Rev. Lett. **91**, 017203 (2003).

[167] T. Eimüller et al., *Uncompensated spins in a micro-patterned CoFeB/MnIr exchange bias system*, Appl. Phys. Lett. **85**, 2310 (2004).

[168] P. Kappenberger et al., *Direct imaging and determination of the uncompensated spin density in exchange-biased CoO/(CoPt) multilayers*, Phys. Rev. Lett. **91**, 267202 (2003).

[169] Durham Magneto Optics Ltd., *NanoMOKE2 manual*, 2003.

[170] T. Uhrmann, *Giant-Magneto-Resistance (GMR) Sensoren auf polymerem Trägermaterial*, Fachhochschule Regensburg, 2005.

[171] T. Uhrmann et al., *Magnetostrictive GMR sensor on flexible polyimide substrates*, J. Magn. Magn. Mater. **submitted** (2005).